Article

ZFTA–RELA ependymomas make itaconate to epigenetically drive fusion expression

https://doi.org/10.1038/s41586-025-10005-1

Received: 8 July 2023

Accepted: 4 December 2025

Siva Kumar Natarajan[1,2,3], Joanna Lum[1,2,3], James Haggerty Skeans[1,2,4], Minal Nenwani[5,6,7], Sanjana Eyunni[3,8], Mateus Mota[1,2], Jill M. Bayliss[1,2], Akash Deogharkar[1,2], Erin Taya Hamanishi[1,9], Matthew Pun[1,2,4], Stefan R. Sweha[1,2], Simon Hoffman[1,2], Eleanor Young[8], Qiuyang Zhang[10,11], Rijul Mehta[1,2], Olamide Animasahun[5,6,12], Pranav Narayanan[1,2], Sushanth Sunil[1,2], Abhijit Parolia[8,10,11], Peter Sajjakulnukit[13], Pooja Panwalkar[1,2], Robert Doherty[9], Madison Clausen[9], Derek Dang[1,2,3], Debra Hawes[14], Fusheng Yang[14], Mariarita Santi[15], Alexander R. Judkins[14], Yelena Wilson[16], Thomas Vigil[13], Andrea Franson[9], Richard M. Mortensen[17], Tatsuya Ozawa[18,19], Andrea Griesinger[20,21], Eric C. Holland[18,19], Nicholas K. Foreman[20,21], Kulandaimanuvel Antony Michealraj[22], Sameer Agnihotri[23,24,25], Michael Taylor[26], Richard J. Gilbertson[27,28], Carl Koschmann[9,10], Arul M. Chinnaiyan[8,10,11,29], Costas A. Lyssiotis[10,13,30], Deepak Nagrath[5,6,7,10,12] & Sriram Venneti[1,2,8,10] ✉

ZFTA–RELA^{+} ependymomas are malignant brain tumours defined by fusions formed between the putative chromatin remodeller ZFTA and the NF-κB mediator RELA[1]. Here we show that ZFTA–RELA^{+} cells produce itaconate, a key macrophage-associated immunomodulatory metabolite[2]. Itaconate is generated by *cis*-aconitate decarboxylase 1 (ACOD1; also known as IRG1). However, the production of itaconate by tumour cells and its tumour-intrinsic role are not well established. ACOD1 is upregulated in a ZFTA–RELA-dependent manner. Functionally, itaconate enables a feed-forward system that is crucial for the maintenance of pathogenic ZFTA–RELA levels. Itaconate epigenetically activates ZFTA–RELA transcription by enriching for activating H3K4me3 via inhibition of the H3K4 demethylase KDM5. ZFTA–RELA^{+} tumours enhance glutamine metabolism to supply carbons for itaconate synthesis. Antagonism of ACOD1 or glutamine metabolism reduces pathogenic ZFTA–RELA levels and is potently therapeutic in multiple in vivo models. Mechanistically, ZFTA–RELA epigenetically suppresses PTEN expression to upregulate PI3K–mTOR signalling, a known driver of glutaminolysis. Finally, suppression of ACOD1 or a combination of glutamine antagonism with PI3K–mTOR inhibition abrogates spinal metastasis. Our data demonstrate that ZFTA–RELA^{+} ependymomas subvert a macrophage-like itaconate metabolic pathway to maintain expression of the ZFTA–RELA driver, which implicates itaconate as a candidate oncometabolite. Taken together, our results position itaconate upregulation as a previously unappreciated driver of ZFTA–RELA^{+} ependymomas. Our work has implications for future drug development to reduce pathogenic ZFTA–RELA expression for this brain tumour, and will advance our understanding of oncometabolites as a new class of therapeutic dependencies in cancers.

Ependymomas are aggressive brain tumours that arise throughout the neuraxis[3,4]. Despite decades of research, surgical resection and adjuvant therapies remain the mainstays of treatment. Although these treatments are effective in prolonging patient survival, they are not curative[4,5]. More than 80% of ependymomas that arise from cerebral hemispheres or the supratentorial (ST) brain region have recurrent fusions between zinc finger translocation associated (ZFTA) and RELA (also known as p65), a key component of the NF-κB pathway[1]. Rare ependymomas have ZFTA fusions with non-RELA partners, including MAML1, MAML2, NCOA1 and NCOA2 (ref. 6). Collectively, these are referred to as ZFTA fusion ependymomas and occur in both children (frequency of 66–84%) and adults (frequency of 20–58%)[3,7–9].

Although neither *ZFTA* nor *RELA* are oncogenic, *ZFTA–RELA* acts as a potent oncogene and is sufficient to transform cells both in vitro and in vivo[1,6,10,11]. ZFTA–RELA spontaneously translocates to the nucleus, and RELA drives pathological NF-κB signalling[1,12]. Moreover, ZFTA–RELA can act as a master chromatin remodeller[6,10,11,13,14]. Despite these biological insights, there are no effective treatments, targeted therapies or clinical trials available for ZFTA-driven ependymomas.

Our premise for this study is based on metabolic reprogramming as a cancer hallmark[15,16]. Many cancers generate metabolites that

---

A list of affiliations appears at the end of the paper.

contribute to cancer pathogenesis, and these are termed oncometabolites. Such oncometabolites include D-2-hydroxyglutarate (D-2HG) in cancers with mutant isocitrate dehydrogenase 1 and 2 (IDH1/2m), α-ketoglutarate (αKG), succinate and fumarate[17,18]. Many of these metabolites directly affect chromatin by altering histone and DNA modifications[19–21]. It is unknown whether the ZFTA–RELA fusion can reprogram integrated metabolic–epigenetic pathways and whether this information can be leveraged for therapeutic development. To address this knowledge gap, we analysed ependymoma tumour samples, patient-derived cells and animal models. As ZFTA–RELA can both activate NF-κB signalling and remodel chromatin[1,6,10,11,14], we focused our efforts on the interplay among signalling pathways, metabolism and epigenetics. Here we show that ZFTA–RELA induces the production of itaconate, an immunomodulatory metabolite secreted by macrophages[2,22,23]. We demonstrate that ZFTA–RELA$^+$ cells use glutamine carbons for itaconate production and that this glutamine dependency is a metabolic vulnerability. Moreover, interruption of this pathway leads to therapeutic effects in animal models and reduces protein levels of the pathogenic driver ZFTA–RELA. Our results provide a tractable and unexplored therapeutic avenue for these tumours.

ZFTA–RELA induces itaconate production

To define metabolic dependencies in ZFTA–RELA$^+$ ependymomas, we performed metabolomics in isogenic mouse neuronal stem cell (mNSC) models expressing either empty vector (EV) (EV mNSCs) or ZFTA–RELA fusion 1 (the most common form, referred to hereafter as ZFTA–RELA mNSCs)[1,10]. Itaconate was the highest upregulated metabolite in ZFTA–RELA mNSCs (Fig. 1a and Supplementary Table 1). Itaconate is an immunomodulatory metabolite that is generated by macrophages in response to pathogen or lipopolysaccharide (LPS) exposure[2,22], but its production by tumour cells is less explored. We confirmed our results by measuring itaconate levels in various models, using LPS-stimulated brain macrophages as positive controls. Itaconate levels were higher in ZFTA–RELA mNSCs than in control mNSCs and comparable with, but lower (around 50%) than, LPS-stimulated brain macrophages (Extended Data Fig. 1a). Itaconate is derived from the TCA cycle metabolite *cis*-aconitate. Glutamine, which can feed the TCA cycle, was also upregulated in ZFTA–RELA mNSCs compared with EV mNSCs (Fig. 1a,b and Supplementary Table 1). We validated this finding in ZFTA–RELA mNSCs and in patient-derived ependymoma cell lines (Fig. 1c and Extended Data Fig. 1b). Itaconate levels were higher in ZFTA–RELA mNSCs than in cells without a ZFTA fusion (non-ZFTA fusion cells) (Extended Data Fig. 1c). We therefore speculated that itaconate has a crucial role in the pathogenesis of ZFTA–RELA$^+$ ependymomas.

We confirmed our results using multiple orthogonal approaches. Itaconate is synthesized from *cis*-aconitate by the enzyme ACOD1 (Fig. 1d). ACOD1 levels were higher in ZFTA–RELA$^+$ cells than in controls (Fig. 1e and Extended Data Fig. 1d,e). To determine the relevance of this finding to human disease, we assessed ACOD1 expression by immunohistochemistry (IHC) in ZFTA–RELA$^+$ ependymomas and in ependymomas caused by a non-ZFTA fusion. We also examined posterior fossa group A, posterior fossa group B, spinal and myxopapillary ependymomas (Supplementary Table 2). ACOD1 expression was higher in ZFTA–RELA$^+$ (showing a range of expression) than in non-ZFTA fusion ependymomas (Fig. 1f and Extended Data Fig. 1f).

To test whether ACOD1 expression was driven by ZFTA–RELA, we used short hairpin RNAs (shRNAs) that target different regions of the fusion protein and confirmed knockdown by blotting for RELA, which detects both endogenous RELA and the higher-molecular-weight ZFTA–RELA (Fig. 1g). Functionally, *ZFTA–RELA* knockdown decreased the proliferation of patient-derived EP1NS (ZFTA–RELA$^+$) cells (Extended Data Fig. 1g). Moreover, ACOD1 levels were reduced proportionally to the extent of *ZFTA–RELA* knockdown (Fig. 1h). To assess the relationship between the levels of ZFTA–RELA and ACOD1 expression, we generated mNSCs that express high or low levels of the fusion protein (Extended Data Fig. 1h). We also used a panel of ependymoma cells derived from a patient with a ZFTA–RELA$^+$ tumour and from mice with varying amounts of ZFTA–RELA protein expression (Extended Data Fig. 1h). ACOD1 and ZFTA–RELA protein levels showed a positive correlation in these models (Fig. 1i and Extended Data Fig. 1i).

ZFTA–RELA spontaneously translocates to the nucleus in a ZFTA-dependent manner to activate NF-κB signalling[1]. Because NF-κB upregulates ACOD1 in macrophages[24], we tested whether ZFTA–RELA$^+$ cells use a similar mechanism. Deletion of the RELA trans-activating domain (TAD) or the REL homology domain (RHD) in ZFTA–RELA$^+$ cells reduces NF-κB activation to slow tumour growth[10]. Furthermore, deletion of the zinc finger (ZF) domain in the ZFTA partner prevents nuclear translocation to suppress tumour formation[10] (Extended Data Fig. 1j). A previous study[10] showed that *Acod1* mRNA is reduced in cells that express all three of these mutants, which suggests that both ZFTA and NF-κB have a role in ACOD1 upregulation (Extended Data Fig. 1k). We therefore treated ZFTA–RELA mNSCs with the NF-κB inhibitor JSH-23. Treatment led to reduced ACOD1 levels in a dose-dependent manner (Extended Data Fig. 1l). These data suggest that ZFTA–RELA upregulates ACOD1 expression and itaconate production in ependymomas.

Inhibition of ACOD1 suppresses tumour growth

To determine the functional role of itaconate and ACOD1 in ZFTA–RELA$^+$ cells, we targeted ACOD1 in ZFTA–RELA models. Partial *ACOD1* knockdown using independent shRNAs was toxic to ZFTA–RELA$^+$ cells (Extended Data Fig. 2a,b). Toxicity was fully prevented through itaconate supplementation (Extended Data Fig. 2c). We next examined in vivo effects of targeting ACOD1 using mouse models in which ZFTA–RELA expression was induced via in utero electroporation (IUE ZFTA–RELA mouse models)[10,11]. IUE ZFTA–RELA animals were generated in *Acod1* wild-type (*Acod1*$^{\mathrm{WT}}$) or whole-body *Acod1*$^{-/-}$ mice[25]. To restrict *Acod1* knockout to ependymomas, we developed *Nes*^{cre} *Acod1*$^{fl/+}$ IUE ZFTA–RELA animals, in which *Acod1* knockout is confined to tumour cells. Both *Acod1*$^{-/-}$ and *Nes*^{cre}*Acod1*$^{fl/+}$ knockout mice exhibited a significant ($P < 0.0001$) increase (around fourfold) in overall survival compared with *Acod1*$^{\mathrm{WT}}$ animals (Fig. 1j). Moreover, there was no significant difference in survival ($P = 0.8311$) between *Acod1*$^{-/-}$ and *Nes*^{cre} *Acod1*$^{fl/+}$ IUE ZFTA–RELA animals, which suggests that targeting *Acod1* in ependymoma cells is sufficient to suppress tumour growth (Fig. 1j).

To validate our findings, we leveraged a recently characterized itaconate isomer metabolite called citraconate that competitively inhibits ACOD1 (ref. 26). The cell-permeable form dimethyl citraconate potently inhibits ACOD1 in supraphysiological concentrations[26]. Dimethyl citraconate was toxic to ZFTA–RELA cells in vitro (Extended Data Fig. 2d). Mesaconate is similar in structure to itaconate but does not inhibit ACOD1 (ref. 26) and did not show toxicity (Extended Data Fig. 2e). To test whether dimethyl citraconate treatment can recapitulate the effect observed in animals with genetic deletion of *Acod1*, we intravenously injected mice with dimethyl citraconate in IUE (Fig. 1j) and flank (Extended Data Fig. 2f) ZFTA–RELA in vivo models. Treatment with dimethyl citraconate increased overall survival and suppressed tumour growth in both models (Fig. 1j,k and Extended Data Fig. 2f). Next, we tested an ACOD1-specific inhibitor (IRG1-IN-1; also known as ERG344) in ZFTA–RELA mNSCs and in mice with MAF-1329 (ZFTA–RELA$^+$) patient-derived xenografts (PDXs) in both flanks. We observed a significant decrease ($P < 0.0001$) in tumour growth in both models after treatment with IRG1-IN-1 (Fig. 1l and Extended Data Fig. 2g). Notably, in vivo supplementation of itaconate (unmodified itaconate, used throughout) restored tumour growth (Fig. 1l). Our results demonstrate that ACOD1 inhibition is toxic in models of ZFTA–RELA$^+$ ependymoma.

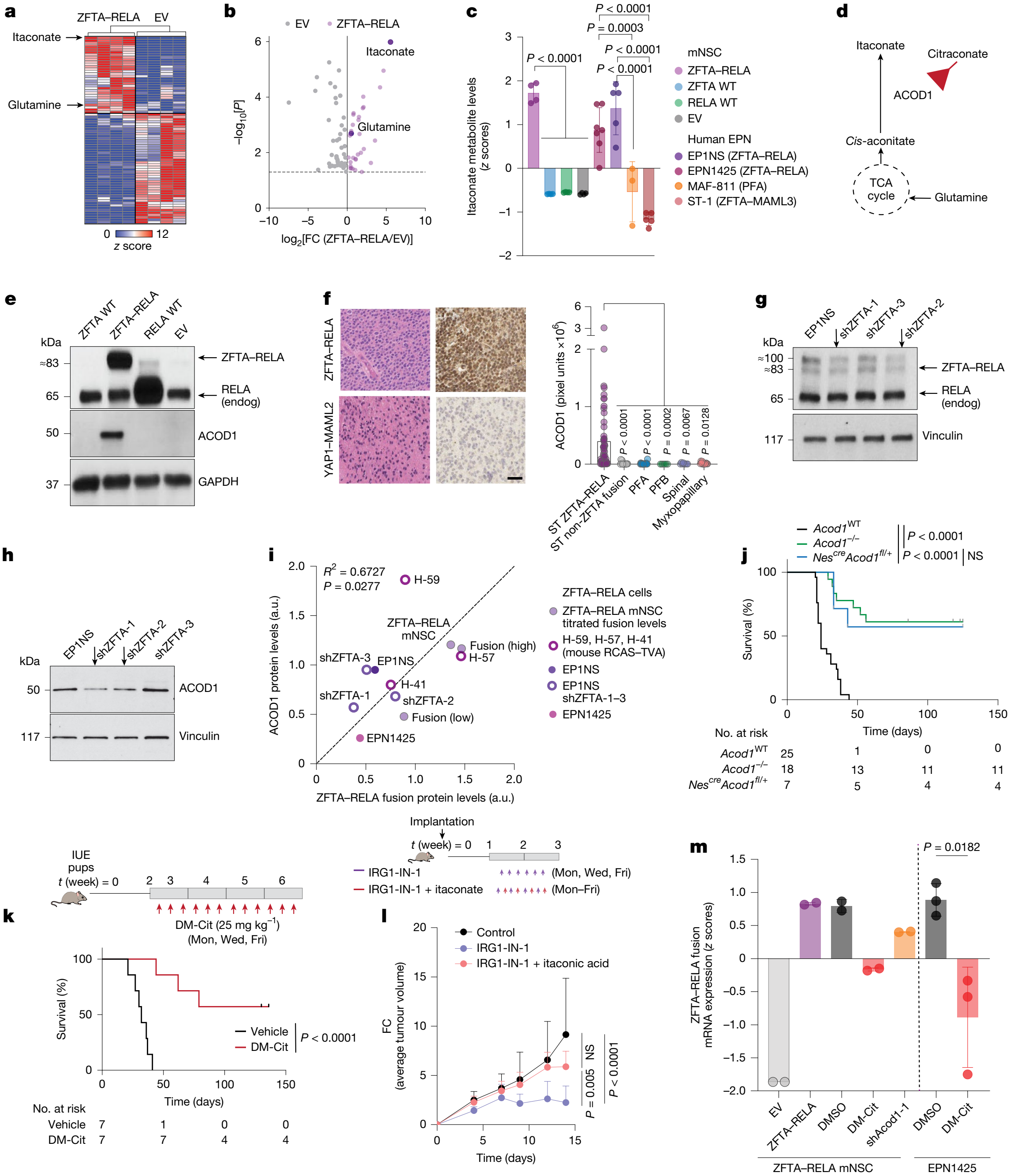

Fig. 1 | ZFTA–RELA induces itaconate production and ACOD1 inhibition suppress tumour growth. a,**b**, Heatmap (**a**) and volcano plot (**b**) of differential metabolites in mNSCs transfected with ZFTA–RELA or EV ($n = 4$, each). FC, fold change. **c**, Itaconate levels (z-scores) in ZFTA–RELA isogenic mNSCs ($n = 4$ for all) and in the following patient-derived ependymoma (EPN) cell lines: EP1NS (ZFTA–RELA$^+$; $n = 5$), EPN1425 (ZFTA–RELA$^+$; $n = 7$); ST-1 (ZFTA–MAML3$^+$; $n = 5$); and MAF-811 (non-fusion posterior fossa type A (PFA); $n = 3$). **d**, Itaconate is synthesized from *cis*-aconitate by ACOD1. Citraconate competitively inhibits ACOD1 (ref. 26). **e**, ZFTA–RELA, endogenous (endog) RELA and ACOD1 protein levels relative to GAPDH in ZFTA–RELA and control mNSCs. **f**, Left, representative haematoxylin and eosin (left) and ACOD1 IHC (right) images from ZFTA–RELA$^+$ and YAP1–MAML2$^+$ cells. Right, blinded quantification of the following ependymomas: ST ZFTA–RELA$^+$ ($n = 18$), ST non-ZFTA fusion ($n = 5$), PFA ($n = 7$), posterior fossa type B (PFB) ($n = 2$), spinal ($n = 3$) and myxopapillary ($n = 4$). Scale bar, 100 µm. **g**,**h**, ZFTA–RELA (**g**) and ACOD1 (**h**) protein levels relative to vinculin in EP1NS cells with or without *ZFTA–RELA* knockdown (using the shRNAs shZFTA-1–shZFTA-3, black arrows show best knockdown). **i**, Correlation between ZFTA–RELA and ACOD1 protein levels (relative to vinculin or GAPDH). H-59, H-57 and H-41 are also mouse ZFTA–RELA$^+$ cells. **j**, Kaplan–Meier analysis of the following mouse models: *Acod1*^{WT} ($n = 25$, median survival of 24 days); *Acod1*$^{-/-}$ ($n = 18$, median survival undefined) and *Nes*^{cre}*Acod*$^{fl/+}$ ($n = 7$, median survival undefined). NS, not significant. **k**, Kaplan–Meier analysis of IUE ZFTA–RELA *Acod1*^{WT} animals treated with vehicle ($n = 7$, median survival of 32 days) or dimethyl citraconate (DM-Cit; 25 mg kg^{-1}, intravenously (i.v.); $n = 7$, median survival undefined). Schematic of the treatment schedule is indicated. **l**, Fold change in tumour volume of mice with ZFTA–RELA mNSC xenografts and treated with vehicle (control; $n = 5$), an ACOD1-specific inhibitor (IRG1-IN-1, 1 mg kg^{-1}, intraperitoneally (i.p.); $n = 6$) or a combination of IRG1-IN-1 (1 mg kg^{-1}, i.p.) and itaconate (25 mg kg^{-1}, i.v.; $n = 8$). Schematic of the treatment schedule is indicated. **m**, *ZFTA–RELA* mRNA levels in the following cells: EV mNSCs; ZFTA–RELA mNSCs treated with vehicle, DM-Cit (10 mM for 24 h) or shAcod1-1 ($n = 2$ each); and EPN1425 cells treated with vehicle or DM-Cit ($n = 3$ each). DMSO, dimethyl sulfoxide. Data are the mean ± s.d. and analysed by unpaired, two-tailed, two-sided, t-tests (**b**,**m**), one-way analysis of variance (ANOVA) with Tukey's multiple comparisons test (**c**,**l**) or Dunn's multiple comparisons test (**f**), Spearman's correlation (**i**) or log-rank tests (**j**,**k**), all with 95% confidence intervals (CI). n indicates independent samples or animals.

Inhibition of ACOD1 reduces ZFTA–RELA levels

To understand the molecular mechanisms that mediate tumour suppression after targeting ACOD1, we performed RNA sequencing (RNA-seq) of ZFTA–RELA mNSCs with or without treatment with dimethyl citraconate or a shRNA targeted against *Acod1* (shAcod1) (Extended Data Fig. 2h and Supplementary Tables 3 and 4). We determined commonly upregulated (143) and downregulated (261) genes. Upregulated pathways included neuron projection and cholesterol and lipid metabolism (Extended Data Fig. 2i,j and Supplementary Tables 5 and 6). Suppressed pathways included downregulation of NF-κB signatures as the top hit (Extended Data Fig. 2i,k and Supplementary Tables 5 and 7). Notably, *ZFTA–RELA* mRNA was downregulated after *Acod1* knockdown and dimethyl citraconate treatment (Fig. 1m). We confirmed that *ZFTA–RELA* mRNA levels decreased after dimethyl citraconate treatment in patient-derived EPN1425 (ZFTA–RELA$^+$) cells (Fig. 1m). Similarly, ZFTA–RELA protein levels were reduced after ACOD1 suppression in multiple cell lines, including in an inducible system (Fig. 2a,b and Extended Data Fig. 3a,b). We expressed either *ACOD1* cDNA or vector controls in HEK293 cells (Extended Data Fig. 3c) and then transfected them with inducible ZFTA–RELA. In these cells, dimethyl citraconate reduced ZFTA–RELA levels, and this effect was attenuated by *ACOD1* overexpression (Extended Data Fig. 3d). We validated our findings using the ACOD1 inhibitor IRG1-IN-1, which also reduced ZFTA–RELA levels (Extended Data Fig. 3e,f). Moreover, IRG1-IN-1 reduced ZFTA–RELA protein levels in vivo, and this effect was rescued by itaconate supplementation (Fig. 2c).

Our RNA-seq and quantitative PCR (qPCR) data demonstrated that *ZFTA–RELA* mRNA levels were decreased after targeting *ACOD1* (Fig. 1m), which suggests that transcriptional regulation is involved in this process. Itaconate is structurally similar to the oncometabolite D-2HG produced by IDH1/2m[27–29]. D-2HG competitively inhibits αKG-dependent DNA and histone demethylases, which results in epigenetic hypermethylation[30,31]. Similar to D-2HG, itaconate competitively inhibits the αKG-dependent DNA demethylase TET2 in macrophages[27–29]. On the basis of this premise, we proposed that itaconate modifies chromatin in ZFTA–RELA$^+$ ependymomas and focused on the transcription-activating mark H3K4me3. The H3K4 histone demethylase KDM5 depends on αKG and is inhibited by D-2HG to increase H3K4me3 levels in tumours with mutant IDH1/2m[30,32]. Given its structural similarity to 2HG, we proposed that itaconate could also inhibit KDM5. There are two isoforms of 2HG: D-2HG and L-2HG (the more potent physiological isoform)[33]. We tested the ability of itaconate to inhibit KDM5 compared with both L-2HG and D-2HG in cell-free assays with unmodified metabolites. Itaconate had a stronger KDM5 inhibitory activity than D-2HG but showed similar half-maximal inhibitory (IC_{50}) values to the more potent L-2HG (Fig. 2d and Extended Data Fig. 3g).

These data led us to propose that itaconate inhibits KDM5 to increase H3K4me3. Conversely, suppression of itaconate reduces H3K4me3 levels (Fig. 2e). *Acod1* knockdown in ZFTA–RELA mNSCs and dimethyl citraconate treatment in ZFTA–RELA$^+$ cells reduced H3K4me3 levels (Fig. 2f and Extended Data Fig. 3h). Both unmodified citraconate and cell-permeable dimethyl citraconate reduced ZFTA–RELA and H3K4me3 levels, with a greater effect observed with cell-permeable dimethyl citraconate (Fig. 2f and Extended Data Fig. 3i). Treatment with dimethyl citraconate reduced H3K4me3 levels in cell lines without the ZFTA–RELA fusion, which suggested that there are additional regulatory mechanisms involved in this process (Extended Data Fig. 3j). Conversely, supplementation of itaconate to mNSCs that do not express a fusion protein (non-fusion mNSCs) was sufficient to increase H3K4me3 levels (Fig. 2g). Similarly, ACOD1 overexpression upregulated H3K4me3 in HEK293 cells (Extended Data Fig. 3k). The addition of exogenous itaconate to ZFTA–RELA$^+$ cells with *Acod1* knocked down increased H3K4me3 levels, but not H3K27ac or H3K9me3, and simultaneously rescued ZFTA–RELA expression (Fig. 2h and Extended Data Fig. 3l). Consistent with our hypothesis, exogenous addition of cell-permeable dimethyl αKG to ZFTA–RELA cells reduced both H3K4me3 and ZFTA–RELA levels (Extended Data Fig. 3m,n). Conversely, cell-permeable octyl-L-2HG increased ZFTA–RELA expression in EPN1425 cells (Extended Data Fig. 3n).

To assess genome-wide H3K4me3 alterations, we performed H3K4me3 chromatin immunoprecipitation with sequencing (ChIP–seq) and assessed chromatin accessibility in parallel using assay for transposase-accessible chromatin with sequencing (ATAC-seq). The addition of dimethyl citraconate reduced chromatin accessibility globally in ZFTA–RELA mNSCs ($n = 12,117$ reduced accessibility sites compared with $n = 369$ gained accessibility sites) (Fig. 2i, Extended Data Fig. 4a and Supplementary Table 8). Moreover, dimethyl citraconate enhanced chromatin accessibility of genes involved in neurodevelopment and lipid metabolism and suppressed genes involved in growth factor signalling and cell migration (Extended Data Fig. 4b,c and Supplementary Tables 9 and 10). Similarly, H3K4me3 ChIP–seq of ZFTA–RELA$^+$ cells revealed that dimethyl citraconate treatment reduced H3K4me3 enrichment globally ($n = 9,897$ reduced sites compared with $n = 230$ enriched sites) (Fig. 2i, Extended Data Fig. 4d and Supplementary Table 11). Genes that gained H3K4me3 marks belonged mainly to neurogenesis and neurodevelopmental pathways (Extended Data Fig. 4e and Supplementary Table 12). Genes with reduced H3K4me3 marks corresponded to chromatin organization and remodelling (Extended Data Fig. 4f and Supplementary Table 13). Patient-derived EPN1425 cells treated with dimethyl citraconate showed similar changes in H3K4me3 enrichment (Extended Data Fig. 4g–i and Supplementary Tables 14–16). Overlapping of ATAC-seq and H3K4me3 ChIP–seq data revealed genes that were commonly epigenetically upregulated ($n = 17$) or downregulated ($n = 6,820$) after dimethyl citraconate treatment, and included chromatin remodelling and DNA repair pathways (Extended Data Fig. 4j,k and Supplementary Tables 17 and 18).

These data indicate that an increase in H3K4me3 levels, independent of itaconate treatment, would be sufficient to reverse the effects of dimethyl citraconate. To test this idea, we used CPI-455, a small-molecule KDM5 inhibitor. Treatment of ZFTA–RELA mNSCs with CPI-455 increased H3K4me3 levels (Extended Data Fig. 3o) and reversed the effects of dimethyl citraconate (Fig. 2j). These results demonstrate that ACOD1 inhibition decreases both global H3K4me3 and pathogenic ZFTA–RELA expression.

Citraconate epigenetically reduces ZFTA–RELA

The most common ZFTA–RELA fusion in patients with ependymomas is formed between exons 1 and 2 of *ZFTA* and the entire open reading frame of *RELA*[1] (Extended Data Fig. 5a). Regulatory elements essential for the expression of ZFTA–RELA are restricted to the ZFTA partner (shared with wild-type ZFTA and ZFTA–MAML3)[1,34,35] (Extended Data Fig. 5a,b). Moreover, overlap of ATAC-seq and H3K4me3 ChIP–seq data showed that *Zfta*, but not *Rela*, was epigenetically repressed by dimethyl citraconate in ZFTA–RELA$^+$ cells (Fig. 3a). On the basis of this premise, we proposed that dimethyl citraconate reduces genomic H3K4me3 at ZFTA regulatory elements to reduce ZFTA–RELA transcription.

Dimethyl citraconate reduced endogenous ZFTA (and ZFTA–RELA) levels in ZFTA–RELA$^+$ cells and in mNSCs expressing ZFTA or RELA (Extended Data Fig. 5c–e). Conversely, itaconate supplementation increased both H3K4me3 levels (Fig. 2g) and endogenous ZFTA (Fig. 3b). We did not observe a similar consistent pattern with endogenous RELA (Fig. 3b). Moreover, treatment of ZFTA–RELA mNSCs with CPI-455 increased both endogenous ZFTA and ZFTA–RELA levels (Fig. 3c). Other ZFTA fusion ependymomas also contained the same ZFTA regulatory region (Extended Data Fig. 5a,b). ZFTA–MAML3 ST-1 ependymoma cells produced itaconate and expressed ACOD1, but at lower levels than in ZFTA–RELA$^+$ cells (Extended Data Fig. 1c,e). Similar to ZFTA–RELA$^+$ cells, dimethyl citraconate treatment reduced endogenous ZFTA and

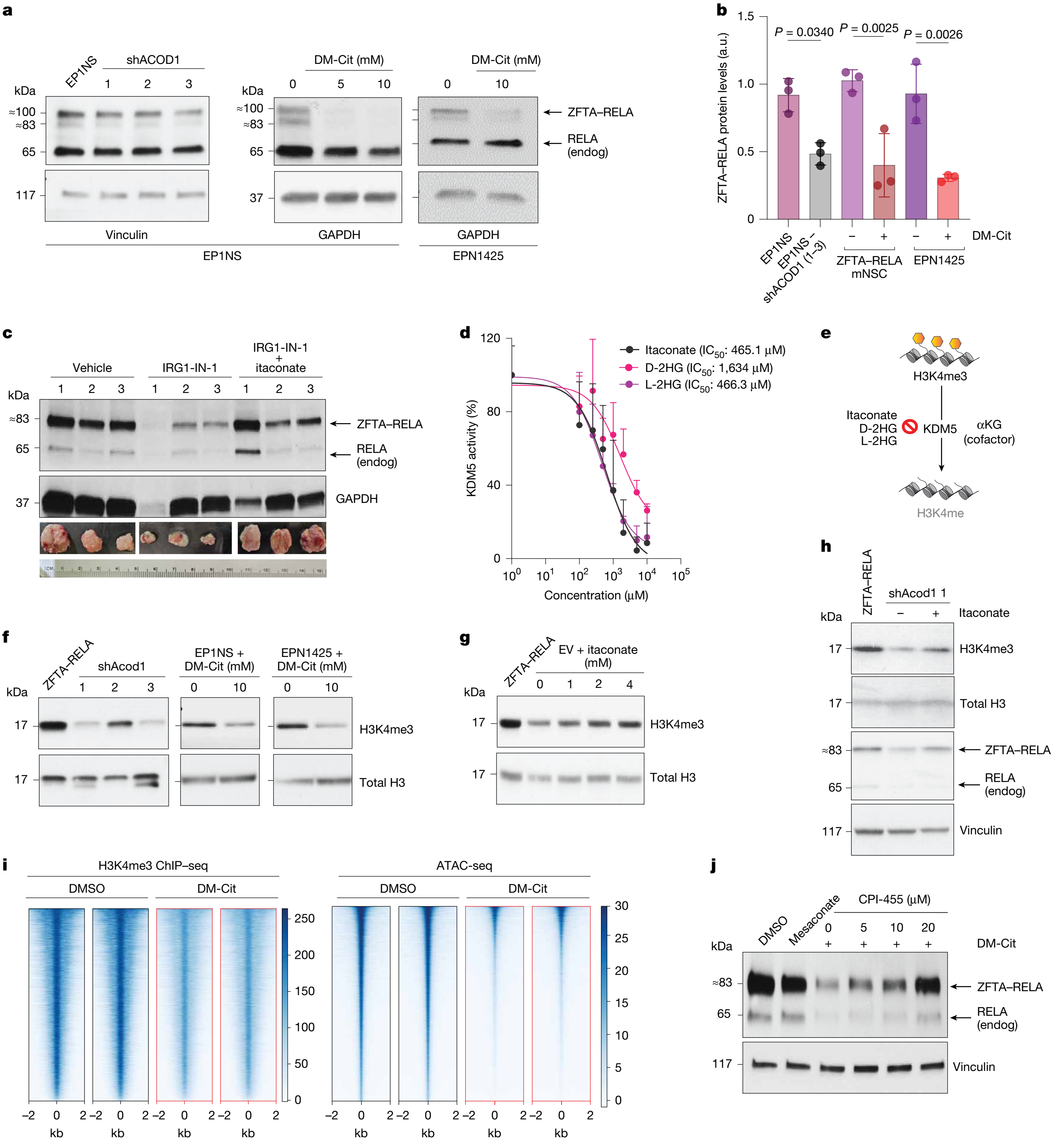

Fig. 2 | Inhibition of ACOD1 reduces global H3K4me3 and decreases pathogenic ZFTA–RELA levels. a, ZFTA–RELA and endogenous RELA levels relative to vinculin or GAPDH in EP1NS cells with or without shACOD1 or DM-Cit (5–10 mM for 24 h) treatment, and in EPN1425 cells with or without DM-Cit (10 mM for 24 h) treatment. **b**, ZFTA–RELA protein levels (normalized to vinculin or GAPDH) in EP1NS cells with or without shACOD1-1–shACOD1-3 treatment, and ZFTA–RELA mNSCs and EPN1425 cells with or without DM-Cit (10 mM for 24 h) treatment (*n* = 3 each). **c**, ZFTA–RELA, endogenous RELA and GAPDH levels in tumours (*n* = 3 each) from animals in Fig. 1l treated with vehicle, IRG1-IN-1 (1 mg kg^{-1}, i.p.) or a combination of IRG1-IN-1 and itaconate (25 mg kg^{-1}, i.v.). Tumour images are shown below. **d**,**e**, KDM5 enzyme inhibition activity (shown as mean ± s.d.) (**d**) and schematic (**e**) of itaconate (*n* = 9), D-2HG (*n* = 5) and L-2HG (*n* = 5) activity. IC_{50} values are indicated. **f**, Blots of H3K4me3 and total H3 in ZFTA–RELA mNSCs with or without shAcod1 treatment (left), and EPN1425 and EP1NS cells with or without DM-Cit (10 mM for 48 h) treatment (right). **g**, Blot of H3K4me3 and total H3 in EV mNSCs with or without itaconate (5–10 mM for 96 h) treatment. **h**, H3K4me3, total H3, ZFTA–RELA, endogenous RELA and vinculin in ZFTA–RELA mNSCs with control (lane 1), shAcod1 (lane 2) or shAcod1 treatment plus 1 mM itaconate for 48 h (lane 3). **i**, Heatmaps of H3K4me3 ChIP–seq (left) and ATAC-seq (right) from ZFTA–RELA mNSCs treated with vehicle or DM-Cit (10 mM for 48 h) showing downregulated genes. **j**, ZFTA–RELA, endogenous RELA and vinculin in ZFTA–RELA mNSCs treated with DMSO, mesaconate (an itaconate analogue that does not inhibit ACOD1 (refs. 26,61) used as a control, 10 mM) or DM-Cit (10 mM) along with indicated concentrations of the KDM5 inhibitor CPI-455 for 48 h. Data are the mean ± s.d. and analysed by one-way ANOVA with Tukey's multiple comparisons test (**b**) or nonlinear regression-fit analysis (**d**), all with 95% CI. *n* indicates independent samples.

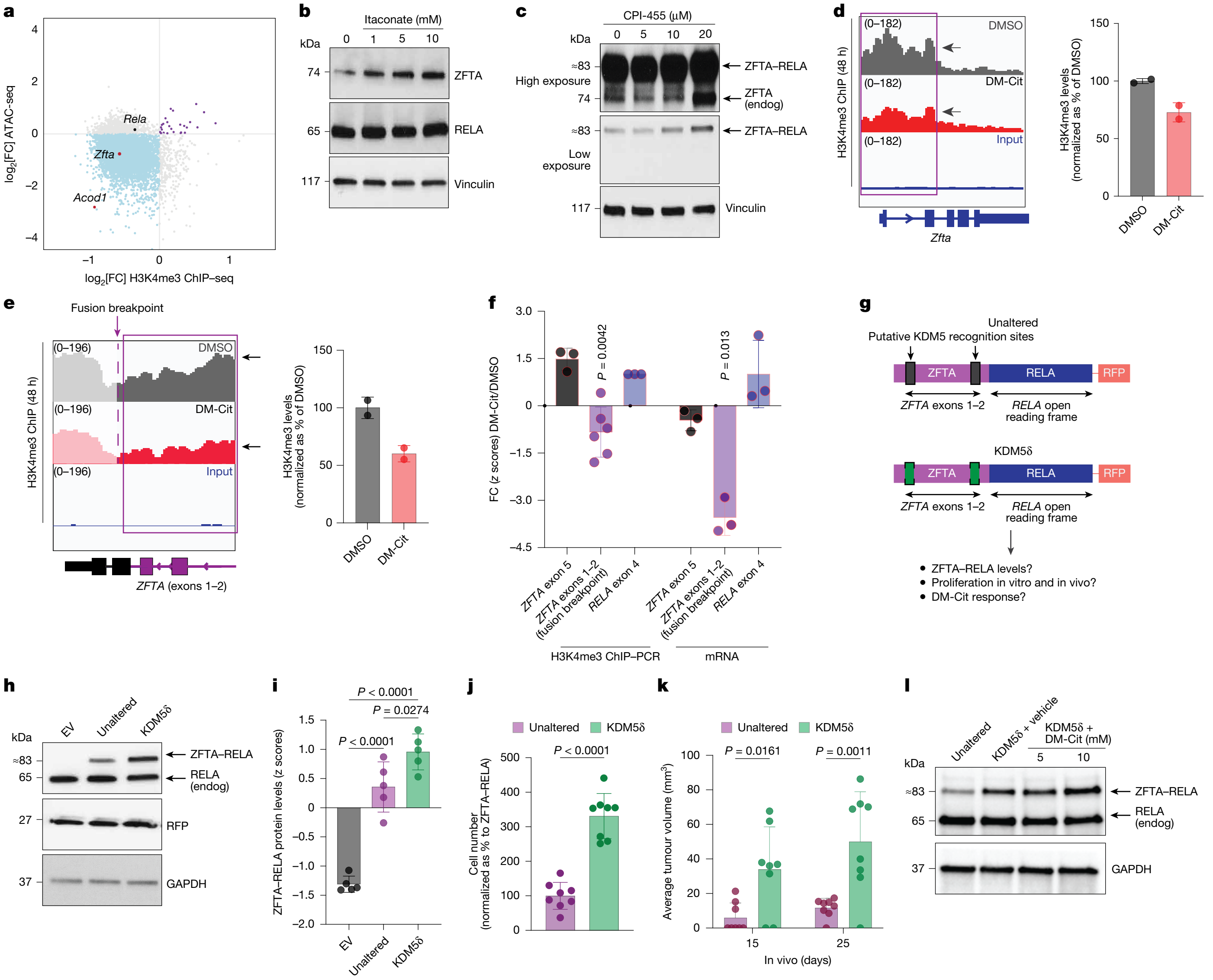

Fig. 3 | DM-Cit reduces genomic H3K4me3 at the ZFTA regulatory region of ZFTA–RELA. a, H3K4me3 enrichment and chromatin accessibility (ATAC-seq) in ZFTA–RELA mNSCs treated with DMSO or DM-Cit (10 mM for 24 or 48 h). **b**, Endogenous ZFTA, RELA and vinculin in EV mNSCs treated with itaconate (at the indicated concentrations for 96 h). **c**, ZFTA–RELA, endogenous ZFTA and vinculin in ZFTA–RELA mNSCs with or without the KDM5 inhibitor CPI-455 (at the indicated concentrations for 48 h). Both high and low exposure of the blots are shown. **d**,**e**, Representative H3K4me3 ChIP tracks (left) and quantification (right) of the *ZFTA* locus (also known as 2700081O15Rik; purple box) in ZFTA–RELA mNSCs (**d**) and EPN1425 cells (**e**) treated with DMSO or DM-Cit (10 mM for 48 h) ($n = 2$ each). **f**, Fold change (citraconate (10 mM) or DMSO for 48 h) for H3K4me3 ChIP–PCR (left) and mRNA qPCR (right) at *ZFTA* exon 5 ($n = 3$), *ZFTA* exons 1–2 (fusion breakpoint that is part of the ZFTA–RELA fusion, $n = 6$) and *RELA* exon 4 ($n = 3$) in EPN1425 cells. **g**, Schematic of KDM5A and KDMAB (KDM5) recognition sites (fusion unaltered, purple boxes)[36,37,39] and the mutant (KDM5δ, green boxes) in the regulatory ZFTA portion of the ZFTA–RELA fusion protein. **h**,**i**, ZFTA–RELA, endogenous RELA, RFP and GAPDH in EV mNSCs, ZFTA–RELA (unaltered) and ZFTA–RELA mutant (KDM5δ) (**h**). ZFTA–RELA relative to GAPDH was quantified ($n = 5$ each) (**i**). **j**,**k**, Cell numbers ($n = 8$ each) at 72 h, normalized to cells expressing the unaltered fusion protein (**j**), and average tumour volume ($n = 8$ samples each) in mice with xenografts of the unaltered fusion or the mutant KDM5δ protein (**k**). **l**, ZFTA–RELA, endogenous RELA and GAPDH in cells with the unaltered fusion protein (lane 1) or the mutant KDM5δ protein treated with vehicle (lane 2) or DM-Cit (lanes 3 and 4, at the indicated concentrations for 48 h). Data are the mean ± s.d. and analysed using two-way ANOVA with Šídák's multiple comparisons test (**f**), one-way ANOVA with Tukey's multiple comparisons test (**i**), unpaired, two-tailed, two-sided *t*-test (**j**) or two-way ANOVA with Šídák's multiple comparisons test (**k**), all with 95% CI. *n* indicates independent samples.

ZFTA–MAML3, and caused dose-dependent toxicity in ST-1 ependymoma cells (Extended Data Fig. 5f,g).

These data prompted us to focus on genomic changes at the ZFTA regulatory region. H3K4me3 ChIP–seq revealed decreased H3K4me3 enrichment at this region after dimethyl citraconate treatment in both ZFTA–RELA mNSCs and EPN1425 cells (Fig. 3d,e and Extended Data Fig. 5h). This was accompanied by decreased chromatin accessibility at the *Zfta* regulatory locus (Extended Data Fig. 5i). To investigate this *ZFTA* regulatory locus in the fusion gene, we conducted H3K4me3 ChIP–PCR in EPN1425 cells, using primers specific to the fusion breakpoint *ZFTA* regulatory region (exons 1 and 2). We observed a similar decrease in H3K4me3 enrichment after dimethyl citraconate treatment at the fusion ZFTA regulatory elements (Fig. 3f). As controls, primers that spanned exon 5 of *ZFTA* (excluded from the fusion protein) and exon 4 of *RELA* did not show a similar significant decrease in H3K4me3 enrichment after dimethyl citraconate treatment (Fig. 3f and Extended Data Fig. 5j). In parallel, dimethyl citraconate treatment decreased mRNA levels of fusion-specific *ZFTA* exons 1 and 2, whereas minimal or no change was observed in *ZFTA* exon 5 or *RELA* exon 4 (Fig. 3f and Extended Data Fig. 5k).

Because our data showed that itaconate can affect KDM5 activity (Fig. 2d), we investigated whether changes in H3K4me3 levels at the *ZFTA* regulatory region depend on KDM5. We identified two putative KDM5 recognition sites[36–39] in the *ZFTA* regulatory region (Fig. 3g). We proposed that mutating these KDM5 recognition sites would reduce H3K4 demethylation and lead to three potential outcomes: (1) increased H3K4me3 enrichment at the ZFTA regulatory region; (2) increased ZFTA–RELA expression; and (3) reduced sensitivity to dimethyl citraconate. mNSCs were transfected with red fluorescent protein (RFP)-tagged unaltered ZFTA–RELA or plasmids with a KDM5 mutant (KDM5δ). In this mutant, the KDM5A recognition site in *ZFTA* exon 1 was changed from CCGCCC to CCACCA, and the KDM5B recognition site in *ZFTA* exon 2 was changed from GCACAC to GCAAAC (Fig. 3g). We performed H3K4me3 ChIP–PCR using specific primers for the ZFTA regulatory region. Compared with mNSCs transfected with unaltered ZFTA–RELA, mNSCs transfected with KDM5δ showed increased H3K4me3 enrichment at the *ZFTA* regulatory region but did not have altered global H3K4me3 levels (Extended Data Fig. 5l,m). This was accompanied by an increase in ZFTA–RELA and downstream ACOD1 protein levels (Fig. 3h,i and Extended Data Fig. 5n). Functionally, there was increased proliferation in vitro and enhanced tumour growth in vivo with mNSCs expressing KDM5δ compared with mNSCs expressing unaltered ZFTA–RELA (Fig. 3j,k and Extended Data Fig. 5o). Moreover, KDM5δ-expressing mNSCs treated with dimethyl citraconate did not show decreased ZFTA–RELA expression (Fig. 3l) and had attenuated toxicity (Extended Data Fig. 5p). Overall, our data suggest that dimethyl citraconate reduces enrichment of H3K4me3 at *ZFTA* regulatory regions, which in turn leads to a decrease in ZFTA fusion expression.

Glutamine is used to produce itaconate

We mapped metabolic pathways used by ZFTA–RELA$^+$ cells to generate itaconate using ^{13}C-isotope labelling. Both glucose and glutamine can be used for itaconate production in macrophages[40,41]. ZFTA–RELA$^+$ cells produced higher glutamine levels than non-fusion cells (Fig. 1a,b and Extended Data Fig. 6a). Furthermore, ZFTA–RELA mNSCs and EPN1425 cells showed enhanced glutamine uptake and metabolism compared with non-fusion controls (Extended Data Fig. 6b,c). Glutamine can give rise to itaconate through oxidative decarboxylation (M+4) (Fig. 4a and Extended Data Fig. 6d) or through reductive carboxylation (M+5) (Fig. 4a and Extended Data Fig. 6e). Isotope tracing showed that glutamine gave rise to itaconate mainly through oxidative decarboxylation (M+4), with the fifth carbon derived from glucose (Fig. 4b and Extended Data Fig. 6f–h). Glutamine can be taken up by cancer cells via the importer SLC1A5 and is metabolized to glutamate by glutaminase (GLS)[42] (Fig. 4a). GLS levels were higher in ZFTA–RELA mNSCs than in non-fusion mNSCs (Fig. 4c and Extended Data Fig. 7a). We confirmed higher SLC1A5 and GLS protein levels in ZFTA–RELA$^+$ cells than in non-fusion cells (Extended Data Fig. 7b–e). *ZFTA–RELA* knockdown decreased both GLS and SLC1A5 levels (Fig. 4c and Extended Data Fig. 7e). Furthermore, compared with patients with non-fusion ependymomas, ZFTA–RELA$^+$ cells showed higher mRNA levels of *SLC1A5* and *GLS* from published bulk[3] and single-cell RNA-seq[43] datasets (Extended Data Fig. 7f,g), and increased *SLC1A5* expression by IHC (Extended Data Fig. 7h,i). Together, our data demonstrate that ZFTA–RELA$^+$ ependymomas upregulate glutamine metabolism to generate itaconate.

ZFTA–RELA epigenetically reduces PTEN

We analysed in detail mechanisms by which ZFTA–RELA enhances glutamine metabolism. Glutaminolysis is regulated by master metabolic factors, including PI3K–AKT signalling and MYC that upregulate GLS[44] (Fig. 4d). Compared with control mNSCs, ZFTA–RELA mNSCs exhibited PI3K–AKT–mTOR activation, as evidenced by increased phosphorylated AKT (pAKT) and phosphorylated S6RP (pS6RP) levels and downstream phosphorylated GSK3α and GSK3β (pGSK3α/β) levels (Fig. 4e and Extended Data Fig. 8a,b). Moreover, pAKT and MYC were increased in patient-derived cells and in a dose-dependent manner when ZFTA–RELA expression was increased in mNSCs (Extended Data Fig. 8c,d). PTEN is a key tumour suppressor that antagonizes PI3K–AKT signalling. *PTEN* is often deleted in tumours, which leads to activation of PI3K–AKT, MYC and glutamine metabolism, which prompted us to analyse PTEN expression patterns in more detail[44–46]. Compared with control mNSCs, ZFTA–RELA mNSCs had lower *Pten* mRNA and protein levels (Fig. 4e and Extended Data Fig. 8e,f). PTEN reduction was not due to genetic deletions or mutations[1,3] (Extended Data Fig. 8g). We verified that PTEN protein levels were lower in ZFTA–RELA$^+$ cells than in non-fusion cells (Extended Data Fig. 8h). PTEN immunostaining was lower in ZFTA–RELA$^+$ mouse tumours than in normal brain (Fig. 4f and Extended Data Fig. 8i). Notably, IHC showed that ZFTA–RELA$^+$ ependymomas had reduced PTEN levels compared with non-ZFTA fusion ependymomas (Fig. 4f and Extended Data Fig. 8i). Higher levels of *PI3KA*, *GSK3B* and *MYC* mRNA levels in ZFTA–RELA$^+$ tumour samples than in non-ZFTA fusion tumour samples were also observed in published datasets[3] (Extended Data Fig. 8j).

We proposed that low PTEN increases GLS levels via PI3K–AKT signalling. In support of this hypothesis, low *PTEN* expression was associated with increased *GLS* and *SLC1A5* expression from published ependymoma single-cell RNA-seq data[43] (Extended Data Fig. 8k,l). Moreover, patients with ZFTA–RELA$^+$ ependymomas with low *PTEN* but high *GLS* and *SLC1A5* expression showed worse progression-free and overall survival compared with patients with tumours with high *PTEN* but low *GLS* and *SLC1A5* expression (grouped by *k*-means clustering) (Fig. 4g and Extended Data Fig. 8l). Treatment of cells with two well-characterized, small-molecule inhibitors, MK-2206 (an AKT inhibitor) and PI-103 (a dual PI3K–mTOR inhibitor), both decreased pAKT levels, which was accompanied by reduced MYC and GLS expression (Fig. 4h and Extended Data Fig. 8m).

As ZFTA–RELA$^+$ ependymomas do not exhibit genetic *PTEN* deletions or mutations[1,3] (Extended Data Fig. 8g), we wanted to analyse the mechanism of PTEN downregulation by ZFTA–RELA. Previous studies have suggested that ZFTA–RELA is a chromatin remodeller[6,10,11,14]. We examined *PTEN* mRNA levels in ZFTA–RELA-expressing cells with either nonfunctional ZFTA or RELA (TAD or RHD mutants) from published studies[10]. Only the ZFTA nonfunctional mutant showed high *PTEN* mRNA expression, which suggested that ZFTA, but not RELA, is required to downregulate *PTEN* (Extended Data Fig. 9a). In support of this idea, cells expressing ZFTA fusion proteins exhibited reduced *PTEN* mRNA levels (Extended Data Fig. 9b). These data, along with the known chromatin remodelling function of ZFTA–RELA, led us to speculate that ZFTA–RELA epigenetically represses PTEN expression.

We analysed ZFTA–RELA mNSCs and isogenic mNSCs for repressive H3K27me3 and H3K9me3 marks. ZFTA–RELA mNSCs showed increased H3K27me3 (ref. 11), but not H3K9me3, levels compared with non-fusion mNSCs (Fig. 4i). Similarly, global H3K27me3 levels were higher in ZFTA–RELA$^+$ ependymomas than in non-ZFTA fusion ependymomas (Fig. 4j and Extended Data Fig. 9c). *ZFTA–RELA* knockdown reduced H3K27me3 levels, which was accompanied by an increase in PTEN protein and mRNA expression (Extended Data Fig. 9d,e). Similarly, reducing ZFTA–RELA through ACOD1 inhibition (Fig. 1m) increased *Pten* expression (Extended Data Fig. 9f). These data suggest that ZFTA–RELA represses *PTEN* expression in a H3K27me3-dependent manner. The addition of GSK-343, an EZH2 (H3K27 methyltransferase) inhibitor, led to reduced global H3K27me3 levels in both ZFTA–RELA and EV mNSCs (Fig. 4k). ATAC-seq and H3K27me3 ChIP–seq of ZFTA–RELA$^+$ cells (Extended Data Fig. 9g) showed that there was reduced chromatin accessibility at the *Pten* locus, which was reversed by GSK-343 treatment (Extended Data Fig. 9h). Moreover, H3K27me3 enrichment was reduced at the

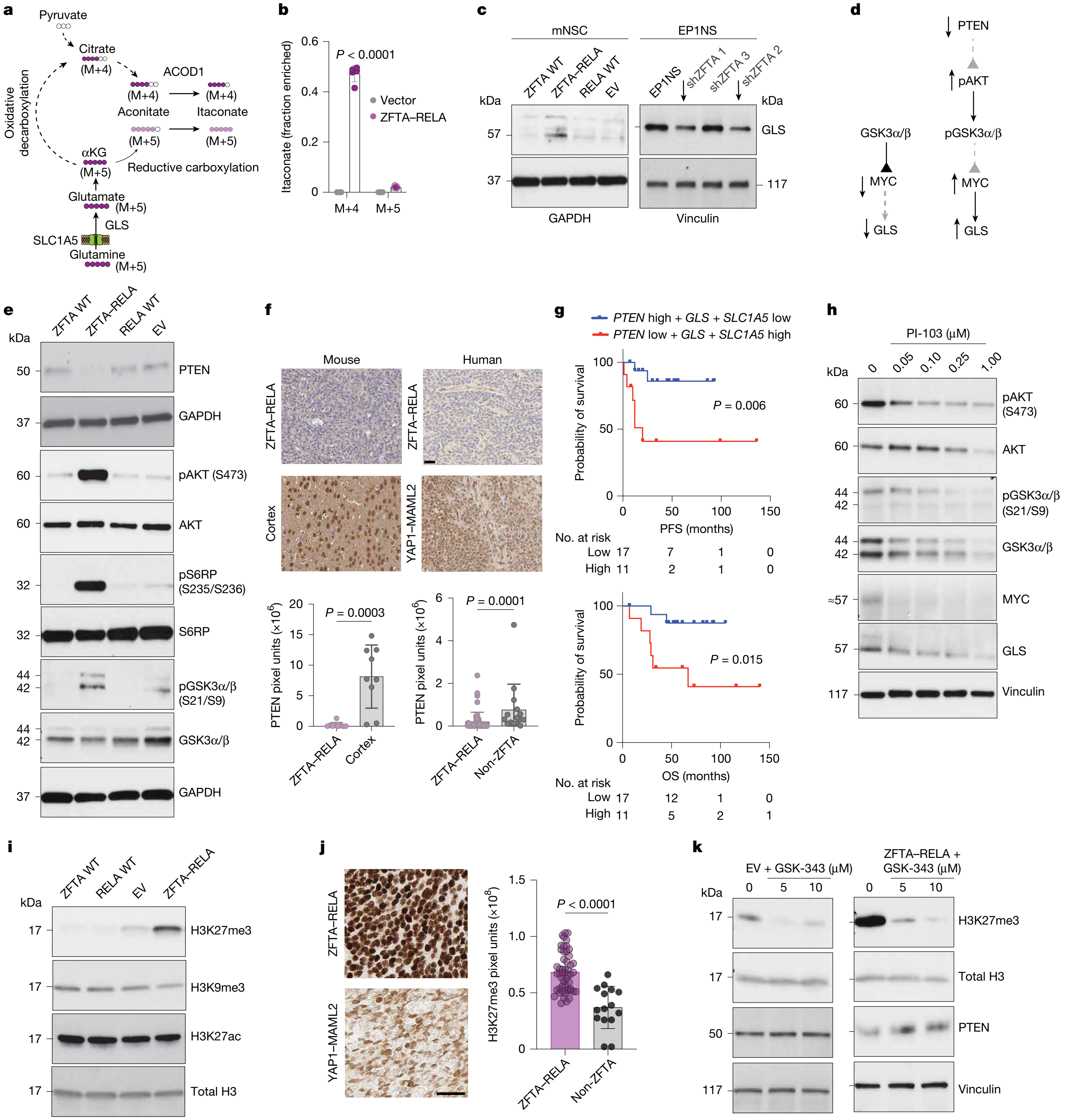

Fig. 4 | ZFTA–RELA epigenetically suppresses PTEN and drives glutamine metabolism to generate itaconate. a,**b**, Schematic (**a**) and quantification (**b**) of itaconate biosynthesis from glutamine (U-^{13}C-GLN) through oxidative phosphorylation (M+4) or reductive carboxylation (M+5) in ZFTA–RELA and EV mNSCs. **c**, GLS and GAPDH or vinculin in isogenic mNSCs (left) and EP1NS cells with or without shZFTA treatment (arrows show best knockdown, right, relative to vinculin). **d**,**e**, Schematic (**d**) and PTEN, pAKT (S473), total AKT, pS6RP (S235/S236), total S6RP, pGSK3α/β (S21/S9), total GSK3α/β and GAPDH in isogenic mNSCs (**e**). **f**, Representative PTEN IHC images (top) and blinded quantification (bottom) from mouse ZFTA–RELA$^+$ ependymomas versus normal brain ($n = 3$ each), and from human ZFTA–RELA$^+$ ($n = 18$) and YAP1–MAML2$^+$ ($n = 5$) ependymomas. Scale bar, 50 µm. **g**, Kaplan–Meier analysis of progression-free (PFS, top) and overall (OS, bottom) survival in patients with *PTEN* high and *GLS* and *SLC1A5* low expression ($n = 17$) and patients with *PTEN* low and *GLS* and *SLC1A5* high expression ($n = 11$) ZFTA–RELA$^+$ ependymomas, as determined by gene expression and *k*-means clustering. **h**, pAKT (S473), total AKT, pGSK3α/β (S21/S9), total GSK3α/β, MYC, GLS and vinculin in ZFTA–RELA mNSCs after treatment with the dual PI3K–mTOR inhibitor PI-103 (at the indicated concentrations for 24 h). **i**, H3K27me3, H3K9me3, H3K27ac and total H3 in isogenic mNSCs. **j**, Representative H3K27me3 IHC images (left) and blinded quantification of ZFTA–RELA$^+$ ($n = 18$) and YAP1–MAML2$^+$ ($n = 5$) ependymomas (right). Scale bar, 12.5 µm. **k**, H3K27me3, total H3, PTEN and vinculin in ZFTA–RELA (right) and EV mNSCs (left) with or without EZH2 inhibitor (GSK-343) treatment (at the indicated concentrations for 48 h). Data are the mean ± s.d. and analysed by unpaired, two-tailed, two-sided *t*-test (**b**,**j**), Mann–Whitney test (**f**) or log-rank test (**g**), all with 95% CI. *n* indicates independent samples.

Pten locus after EZH2 inhibition (Extended Data Fig. 9h), which corresponded to increased PTEN expression in ZFTA–RELA mNSCs (Fig. 4k). Likewise, PTEN levels in EP1NS cells also increased with GSK-343 treatment (Extended Data Fig. 9i,j), which was accompanied by a decrease in downstream AKT activation and reduced GLS levels (Extended Data Fig. 9j,k). EV mNSCs treated with GSK-343 also showed a reduction in global H3K27me3, whereas no changes in PTEN protein were observed (Fig. 4k). Our data suggest that ZFTA–RELA epigenetically represses PTEN expression to activate AKT signalling and drive glutamine metabolism.

Targeting ACOD1 and glutamine metabolism

We assessed the effect of glutamine withdrawal from culture media. Glutamine withdrawal led to increased toxicity in all ZFTA–RELA$^+$ cells compared with control cells (Fig. 5a). This toxicity was partially reversed by itaconate supplementation (Extended Data Fig. 10a). Glutamine withdrawal also decreased H3K4me3, but not H3K9me3, levels (Extended Data Fig. 10b). We next tested various small-molecule inhibitors of glutamine metabolism (Extended Data Fig. 10c). Treatment with the SLC1A5 inhibitor V9302 (ref. 47) or the GLS inhibitor CB-839 (ref. 48) resulted in a greater toxicity in ZFTA–RELA mNSCs than in non-fusion mNSCs (Extended Data Fig. 10d,e). The glutamine antagonist 6-diazo-5-oxo-L-norleucine (DON) reduced tumour growth in mice that had ZFTA–RELA mNSCs transplanted into their flank (Extended Data Fig. 10f,g). Overcoming the blood–brain barrier is a major therapeutic obstacle for brain tumours. We therefore focused our efforts on the glutamine antagonist JHU-083, which is highly CNS-penetrant[49,50]. ZFTA–RELA$^+$ cells showed greater toxicity after JHU-083 treatment than non-fusion cells (Fig. 5b). Consistent with glutamine feeding itaconate biosynthesis, JHU-083 treatment reduced itaconate levels in ZFTA–RELA mNSCs (Extended Data Fig. 11a). Notably, JHU-083 decreased ZFTA–RELA protein levels in vitro (Fig. 5c) and in vivo (Extended Data Fig. 11b). Moreover, itaconate supplementation reversed JHU-083 toxicity and restored ZFTA–RELA protein levels (Extended Data Fig. 11c,d).

We tested the efficacy of targeting glutamine metabolism with JHU-083 in vivo using multiple animal models. JHU-083 suppressed tumour growth and increased overall survival in mouse models of orthotopic ZFTA–RELA mNSC transplant and in IUE models (Fig. 5d,e and Extended Data Fig. 11f,g). In vivo itaconate supplementation partially rescued JHU-083-mediated tumour suppression (Extended Data Fig. 11e). JHU-083 along with standard-of-care radiation treatment in IUE ZFTA–RELA animals extended survival compared with radiation monotherapy (Extended Data Fig. 11h). We also tested combination therapy with JHU-083 and dimethyl citraconate in mice with a PDX of MAF-1329 tumour cells (Fig. 5f). Intravenous treatment of PDXs with dimethyl citraconate or JHU-083 monotherapy or combination therapy suppressed tumour growth in vivo (Fig. 5f). We confirmed that ZFTA–RELA protein levels were reduced in vivo in animals treated with dimethyl citraconate alone or in combination with JHU-083 (Fig. 5g,h).

We also evaluated the dual PI3K–mTOR inhibitor PI-103 in vitro and in vivo. PI-103 showed greater toxicity in ZFTA–RELA mNSCs than EV mNSCs (Extended Data Fig. 12a). Moreover, PI-103 as monotherapy or in combination with DON suppressed tumour growth in mice in which ZFTA–RELA mNSCs were xenografted into their flanks (Extended Data Fig. 12b–e). Similarly, PI-103 as a single agent and in combination with JHU-083 increased overall survival in animals with orthotopic ZFTA–RELA mNSC xenografts (Extended Data Fig. 12f–h). ZFTA–RELA PDX tumours treated with PI-103 or JHU-083 monotherapy showed growth suppression, with the greatest effect observed with combined PI-103 and JHU-083 treatment (Extended Data Fig. 12j,k). We did not observe a tumour-suppressive effect with JHU-083, PI-103 or dimethyl citraconate treatment in non-ZFTA–RELA or in posterior-fossa group A (MAF-811) ependymoma PDXs (Extended Data Fig. 12i).

Ependymomas can metastasize to the spinal cord and pose a major therapeutic challenge[51,52]. Mice with orthotopic ZFTA–RELA mNSC xenografts developed spontaneous spinal cord metastases and eventually hindlimb paralysis (Fig. 5i,j, and Supplementary Video 1). Metastatic tumours also retained low PTEN expression (Fig. 4f and Extended Data Fig. 12m). Although JHU-083 or PI-103 monotherapy did not alter metastases (Extended Data Fig. 12l), dimethyl citraconate alone, or a combination of JHU-083 and PI-103, abrogated spinal metastasis (Fig. 5i,j and Supplementary video 1). Overall, these data demonstrate that targeting glutamine metabolism and the downstream itaconate metabolic pathway at multiple nodes singly or in combination (Fig. 5k) lead to therapeutic effects in ZFTA–RELA ependymomas, with reduction in levels of the pathogenic fusion protein both in vitro and in vivo.

Discussion

We investigated and exploited metabolic dependencies to identify itaconate as a metabolite produced by ZFTA–RELA$^+$ ependymoma cells. We demonstrated that ACOD1 upregulation by ZFTA–RELA leads to the production of itaconate. Moreover, ZFTA–RELA reduces PTEN to activate PI3K–AKT signalling and stimulate glutamine metabolism. Glutamine serves as a carbon source for generating itaconate. Overall, our results revealed a critical actionable pathway with multiple druggable metabolic vulnerabilities (Fig. 5k). Our findings also have translational relevance, as inhibition of PI3K signalling and glutamine metabolism led to therapeutic effects in multiple ZFTA fusion models.

Itaconate is a macrophage metabolite known for its immunomodulatory properties[2,22]. Studies have revealed that itaconate has various roles in macrophages, including anti-inflammatory and antiviral responses, modulating redox balance through NRF2 activation and modifying cysteine residues on proteins[23,27,53–55]. Itaconate can also affect central carbon metabolism by inhibiting succinate dehydrogenase and modifying glycolytic enzymes[27,28,56–58]. However, the expression of ACOD1 and the production of itaconate by tumour cells, and its potential role in cancers, have not been extensively explored. Our data demonstrated that ZFTA–RELA$^+$ ependymomas use this pathway to promote the production of itaconate. We also observed that antagonism of itaconate and/or inhibition of glutamine metabolism resulted in reduced levels of pathogenic ZFTA–RELA. Mechanistic investigations indicated that this effect was epigenetic, as itaconate increased H3K4me3 levels and led to an increase in endogenous ZFTA and ZFTA–RELA levels. Our results are in line with recent studies that have also identified itaconate as an epigenetic modifier that inhibits the DNA demethylase TET2 in macrophages[27,29]. Our results suggest that ZFTA–RELA$^+$ ependymomas rely on itaconate-mediated epigenetic feedback to sustain the expression of ZFTA–RELA. This pro-oncogenic effect of itaconate to drive integrated metabolic and epigenetic pathways suggests that it could function as an oncometabolite like 2HG, succinate and fumarate in other cancers[17–19,59,60]. Because of its immunoregulatory role, itaconate could also potentially modulate the immune microenvironment in ependymomas.

Collectively, our results suggest that ZFTA–RELA$^+$ ependymomas rely on itaconate for sustained expression of ZFTA–RELA. Our data uncovered new leads for the therapeutic potential of targeting glutamine metabolism and itaconate biosynthesis in ZFTA fusion ependymomas. These findings hold promise for the development of effective treatment strategies against this aggressive cancer.

Online content

Any methods, additional references, Nature Portfolio reporting summaries, source data, extended data, supplementary information, acknowledgements, peer review information; details of author contributions and competing interests; and statements of data and code availability are available at https://doi.org/10.1038/s41586-025-10005-1.

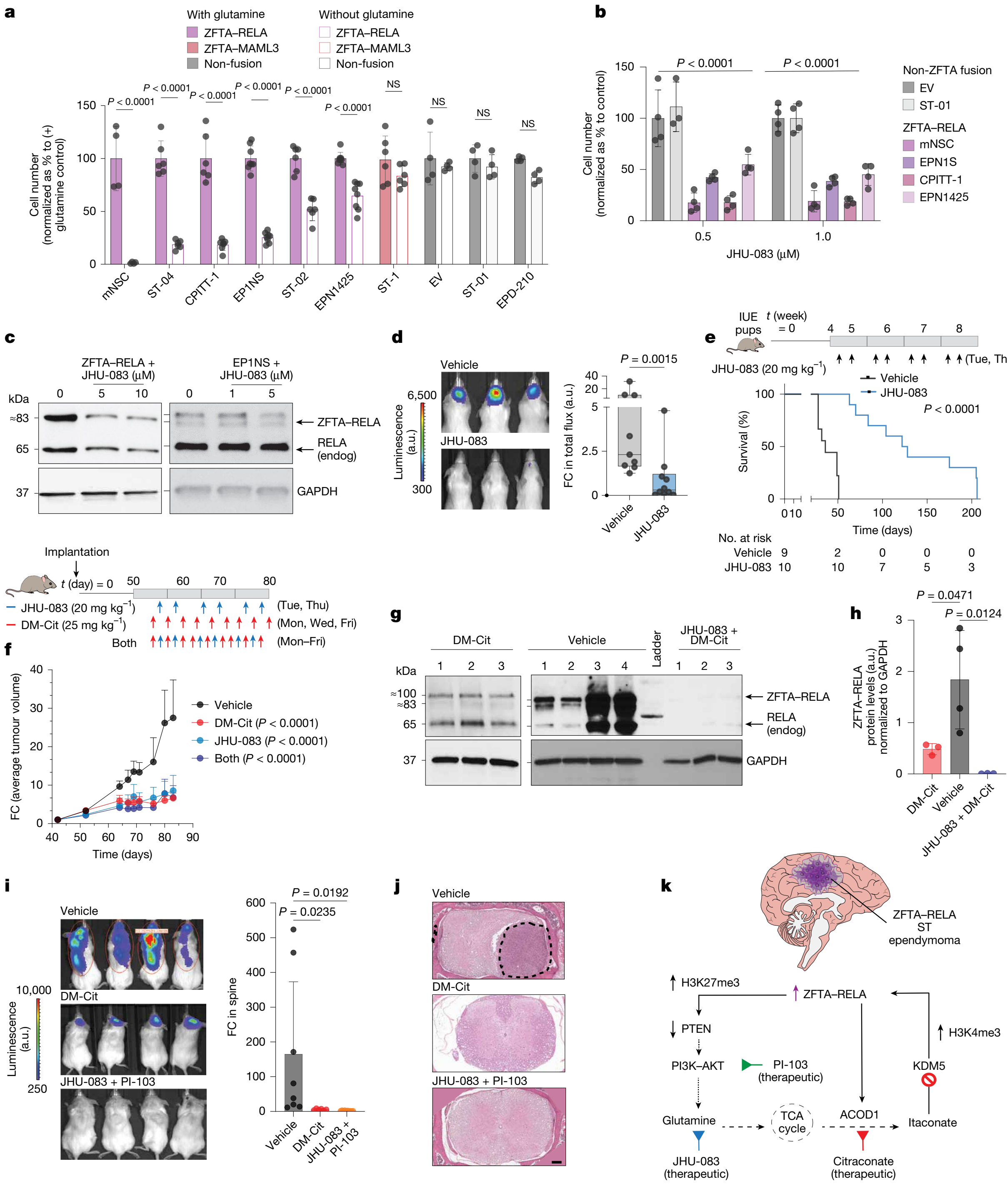

Fig. 5 | Targeting glutamine metabolism leads to therapeutic effects in ZFTA–RELA ependymomas. a,**b**, Cell numbers (normalized to control) in ZFTA–RELA^{+}, ZFTA–MAML3^{+} (ST-1) and non-ZFTA fusion cells with or without glutamine (**a**) or JHU-083 treatment (**b**, at the indicated concentrations) at 96 h. *n* = 4 (ZFTA–RELA mNSC, EV mNSC, ST-01 and EPD-210), *n* = 6 (ST-04, CPITT-1, ST-02 and ST-1) or *n* = 8 (EP1NS and EPN1425). **c**, ZFTA–RELA, endogenous RELA and GAPDH in ZFTA–RELA mNSCs (left) and in EP1NS patient-derived cells (right) treated with or without JHU-083 (at the indicated concentrations for 96 h). **d**,**e**, Representative bioluminescence images (left) and quantification (right, fold change, medians with interquartile ranges, box plot ends show highest and lowest observations) (**d**) and Kaplan–Meier analysis (**e**) of IUE ZFTA–RELA mice treated with vehicle (*n* = 9) or JHU-083 (*n* = 10, orally, 20 mg kg^{-1}, 2 doses per week for 5 weeks). **f**, Tumour volume (fold change) in mice with MAF-1329 (ZFTA–RELA^{+}) PDXs treated with vehicle (*n* = 5), JHU-083 (*n* = 5, 20 mg kg^{-1} orally, 2 doses per week), DM-Cit (*n* = 5, 25 mg kg^{-1}, i.v., 3 doses per week) or a combination of JHU-083 and DM-Cit (*n* = 5) for 4 weeks. **g**,**h**, ZFTA–RELA and endogenous RELA and GAPDH (**g**) and quantification (**h**) of MAF-1329 PDX tumour tissues treated with vehicle (*n* = 4), DM-Cit (*n* = 3) or their combination (*n* = 3). **i**,**j**, Representative bioluminescence images (left) and quantification (right) (**i**) and haematoxylin and eosin images (**j**, dotted region) from spontaneous spinal metastatic tumours in mice with ZFTA–RELA mNSC xenografts treated with vehicle (*n* = 8), DM-Cit (*n* = 6) or a combination of JHU-083 and PI-103. Scale bar, 124 μm. **k**, Schematic illustrating the proposed working model of ZFTA–RELA-driven metabolic reprogramming in ST ependymomas. Data are the mean ± s.d. (except **d**, mean ± minimum to maximum) and analysed by Šídák's multiple-comparison test (**a**), two-way ANOVA with Tukey's multiple comparisons test (**b**), Mann–Whitney (**d**), log-rank (**e**), two-way (**f**) or one-way ANOVA (**h**) with Dunnett's multiple-comparison test, or one-way ANOVA with Holm–Šídák's multiple-comparisons test (**i**), all with 95% CI. *n* indicates independent samples or animals.

1. Parker, M. et al. C11orf95–RELA fusions drive oncogenic NF-κB signalling in ependymoma. *Nature* **506**, 451–455 (2014).
2. O'Neill, L. A. J. & Artyomov, M. N. Itaconate: the poster child of metabolic reprogramming in macrophage function. *Nat. Rev. Immunol.* **19**, 273–281 (2019).
3. Pajtler, K. W. et al. Molecular classification of ependymal tumors across all CNS compartments, histopathological grades, and age groups. *Cancer Cell* **27**, 728–743 (2015).
4. Saleh, A. H. et al. The biology of ependymomas and emerging novel therapies. *Nat. Rev. Cancer* **22**, 208–222 (2022).
5. Merchant, T. E. Current management of childhood ependymoma. *Oncology* **16**, 629–642 (2002).
6. Zheng, T. et al. Cross-species genomics reveals oncogenic dependencies in ZFTA/C11orf95 fusion–positive supratentorial ependymomas. *Cancer Discov.* **11**, 2230–2247 (2021).
7. Louis, D. N. et al. The 2021 WHO classification of tumors of the central nervous system: a summary. *Neuro Oncol.* **23**, 1231–1251 (2021).
8. Witt, H. et al. DNA methylation-based classification of ependymomas in adulthood: implications for diagnosis and treatment. *Neuro Oncol.* **20**, 1616–1624 (2018).
9. Upadhyaya, S. A. et al. Molecular grouping and outcomes of young children with newly diagnosed ependymoma treated on the multi-institutional SJYC07 trial. *Neuro Oncol.* **21**, 1319–1330 (2019).
10. Kupp, R. et al. *ZFTA*-translocations constitute ependymoma chromatin remodeling and transcription factors. *Cancer Discov.* **11**, 2216–2229 (2021).
11. Arabzade, A. et al. ZFTA–RELA dictates oncogenic transcriptional programs to drive aggressive supratentorial ependymoma. *Cancer Discov*. **11**, 2200–2215 (2021).
12. Ozawa, T. et al. A de novo mouse model of C11orf95–RELA fusion-driven ependymoma identifies driver functions in addition to NF-κB. *Cell Rep.* **23**, 3787–3797 (2018).
13. Okonechnikov, K. et al. 3D genome mapping identifies subgroup-specific chromosome conformations and tumor-dependency genes in ependymoma. *Nat. Commun.* **14**, 2300 (2023).
14. Zhu, J. J. C11orf95–RELA reprograms 3D epigenome in supratentorial ependymoma. *Acta Neuropathol.* **140**, 951–960 (2020).
15. Faubert, B., Solmonson, A. & DeBerardinis, R. J. Metabolic reprogramming and cancer progression. *Science* **368**, eaaw5473 (2020).
16. Venneti, S. & Thompson, C. B. Metabolic reprogramming in brain tumors. *Annu. Rev. Pathol.* **12**, 515–545 (2017).
17. Turcan, S. et al. *IDH1* mutation is sufficient to establish the glioma hypermethylator phenotype. *Nature* **483**, 479–483 (2012).
18. Killian, J. K. et al. Succinate dehydrogenase mutation underlies global epigenomic divergence in gastrointestinal stromal tumor. *Cancer Discov.* **3**, 648–657 (2013).
19. Turcan, S. et al. Mutant-IDH1-dependent chromatin state reprogramming, reversibility, and persistence. *Nat. Genet.* **50**, 62–72 (2018).
20. Flavahan, W. A. et al. Insulator dysfunction and oncogene activation in IDH mutant gliomas. *Nature* **529**, 110–114 (2016).
21. Inoue, S. et al. Mutant IDH1 downregulates ATM and alters dna repair and sensitivity to DNA damage independent of TET2. *Cancer Cell* **30**, 337–348 (2016).
22. Hooftman, A. & O'Neill, L. A. J. The immunomodulatory potential of the metabolite itaconate. *Trends Immunol.* **40**, 687–698 (2019).
23. Zhao, H. et al. Myeloid-derived itaconate suppresses cytotoxic CD8$^+$ T cells and promotes tumour growth. *Nat. Metab.* **4**, 1660–1673 (2022).
24. van quickelberghe, e. et al. Identification of immune-responsive gene 1 (IRG1) as a target of A20. *J. Proteome Res.* **17**, 2182–2191 (2018).
25. Nair, S. et al. *Irg1* expression in myeloid cells prevents immunopathology during *M. tuberculosis* infection. *J. Exp. Med.* **215**, 1035–1045 (2018).
26. Chen, F. et al. Citraconate inhibits ACOD1 (IRG1) catalysis, reduces interferon responses and oxidative stress, and modulates inflammation and cell metabolism. *Nat. Metab.* **4**, 534–546 (2022).
27. Aso, K. et al. Itaconate ameliorates autoimmunity by modulating T cell imbalance via metabolic and epigenetic reprogramming. *Nat. Commun.* **14**, 984 (2023).
28. Lampropoulou, V. et al. Itaconate links inhibition of succinate dehydrogenase with macrophage metabolic remodeling and regulation of inflammation. *Cell Metab.* **24**, 158–166 (2016).
29. Chen, L. L. et al. Itaconate inhibits TET DNA dioxygenases to dampen inflammatory responses. *Nat. Cell Biol.* **24**, 353–363 (2022).
30. Gunn, K. et al. (*R*)-2-Hydroxyglutarate inhibits KDM5 histone lysine demethylases to drive transformation in *IDH*-mutant cancers. *Cancer Discov.* **13**, 1478–1497 (2023).
31. Xu, W. et al. Oncometabolite 2-hydroxyglutarate is a competitive inhibitor of α-ketoglutarate-dependent dioxygenases. *Cancer Cell* **19**, 17–30 (2011).
32. Sasaki, M. et al. *IDH1*^{R132H} mutation increases murine haematopoietic progenitors and alters epigenetics. *Nature* **488**, 656–659 (2012).
33. Intlekofer, A. M. et al. Hypoxia induces production of L-2-hydroxyglutarate. *Cell Metab.* **22**, 304–311 (2015).
34. Herranz-Pérez, V. et al. Ependymoma associated protein Zfta is expressed in immature ependymal cells but is not essential for ependymal development in mice. *Sci. Rep.* **12**, 1493 (2022).
35. Ozawa, T. et al. C11orf95–RELA fusion drives aberrant gene expression through the unique epigenetic regulation for ependymoma formation. *Acta Neuropathol. Commun.* **9**, 36 (2021).
36. Zhang, Y. et al. The PHD1 finger of KDM5B recognizes unmodified H3K4 during the demethylation of histone H3K4me2/3 by KDM5B. *Protein Cell* **5**, 837–850 (2014).
37. Johansson, C. et al. Structural analysis of human KDM5B guides histone demethylase inhibitor development. *Nat. Chem. Biol.* **12**, 539–545 (2016).
38. Dorosz, J. et al. Molecular architecture of the Jumonji C family histone demethylase KDM5B. *Sci. Rep.* **9**, 4019 (2019).
39. Tu, S. et al. The ARID domain of the H3K4 demethylase RBP2 binds to a DNA CCGCCC motif. *Nat. Struct. Mol. Biol.* **15**, 419–421 (2008).
40. Puchalska, P. et al. Isotope tracing untargeted metabolomics reveals macrophage polarization-state-specific metabolic coordination across intracellular compartments. *iScience* **9**, 298–313 (2018).
41. Ma, E. H. ^{13}C metabolite tracing reveals glutamine and acetate as critical in vivo fuels for CD8 T cells. *Sci. Adv.* **10**, eadj1431 (2024).
42. Yang, L., Venneti, S. & Nagrath, D. Glutaminolysis: a hallmark of cancer metabolism. *Annu. Rev. Biomed. Eng.* **19**, 163–194 (2017).
43. Gojo, J. et al. Single-cell RNA-seq reveals cellular hierarchies and impaired developmental trajectories in pediatric ependymoma. *Cancer Cell* **38**, 44–59 (2020).
44. Momcilovic, M. et al. The GSK3 signaling axis regulates adaptive glutamine metabolism in lung squamous cell carcinoma. *Cancer Cell* **33**, 905–921 (2018).
45. Wise, D. R. et al. Myc regulates a transcriptional program that stimulates mitochondrial glutaminolysis and leads to glutamine addiction. *Proc. Natl Acad. Sci. USA* **105**, 18782–18787 (2008).
46. Gao, P. et al. c-Myc suppression of miR-23a/b enhances mitochondrial glutaminase expression and glutamine metabolism. *Nature* **458**, 762–765 (2009).
47. Schulte, M. L. et al. Pharmacological blockade of ASCT2-dependent glutamine transport leads to antitumor efficacy in preclinical models. *Nat. Med.* **24**, 194–202 (2018).
48. Gross, M. I. et al. Antitumor activity of the glutaminase inhibitor CB-839 in triple-negative breast cancer. *Mol. Cancer Ther.* **13**, 890–901 (2014).
49. Hanaford, A. R. et al. Orally bioavailable glutamine antagonist prodrug JHU-083 penetrates mouse brain and suppresses the growth of MYC-driven medulloblastoma. *Transl. Oncol.* **12**, 1314–1322 (2019).
50. Chung, C. et al. Integrated metabolic and epigenomic reprograming by H3K27M mutations in diffuse intrinsic pontine gliomas. *Cancer Cell* **38**, 334–349 (2020).
51. Benesch, M. et al. Newly diagnosed metastatic intracranial ependymoma in children: frequency, molecular characteristics, treatment, and outcome in the prospective HIT series. *Oncologist* **24**, e921–e929 (2019).
52. Zacharoulis, S. et al. Metastatic ependymoma: a multi-institutional retrospective analysis of prognostic factors. *Pediatr. Blood Cancer* **50**, 231–235 (2008).
53. Qin, W. et al. Chemoproteomic profiling of itaconation by bioorthogonal probes in inflammatory macrophages. *J. Am. Chem. Soc.* **142**, 10894–10898 (2020).
54. Bambouskova, M. et al. Electrophilic properties of itaconate and derivatives regulate the IκBζ–ATF3 inflammatory axis. *Nature* **556**, 501–504 (2018).
55. Mills, E. L. et al. Itaconate is an anti-inflammatory metabolite that activates Nrf2 via alkylation of KEAP1. *Nature* **556**, 113–117 (2018).
56. Qin, W. et al. S-glycosylation-based cysteine profiling reveals regulation of glycolysis by itaconate. *Nat. Chem. Biol.* **15**, 983–991 (2019).
57. Cordes, T. et al. Immunoresponsive gene 1 and itaconate inhibit succinate dehydrogenase to modulate intracellular succinate levels. *J. Biol. Chem.* **291**, 14274–14284 (2016).
58. Liao, S. T. et al. 4-Octyl itaconate inhibits aerobic glycolysis by targeting GAPDH to exert anti-inflammatory effects. *Nat. Commun.* **10**, 5091 (2019).
59. Kulkarni, R. A. et al. A chemoproteomic portrait of the oncometabolite fumarate. *Nat. Chem. Biol.* **15**, 391–400 (2019).
60. Dang, L. et al. Cancer-associated *IDH1* mutations produce 2-hydroxyglutarate. *Nature* **462**, 739–744 (2009).
61. He, W. et al. Mesaconate is synthesized from itaconate and exerts immunomodulatory effects in macrophages. *Nat. Metab.* **4**, 524–533 (2022).

---

[1]Laboratory of Brain Tumor Metabolism and Epigenetics, Department of Pathology, University of Michigan Medical School, Ann Arbor, MI, USA. [2]Chad Carr Pediatric Brain Tumor Center, Department of Pediatrics, University of Michigan, Ann Arbor, MI, USA. [3]Molecular and Cellular Pathology Graduate Program, University of Michigan Medical School, Ann Arbor, MI, USA. [4]Medical Scientist Training Program, University of Michigan Medical School, Ann Arbor, MI, USA. [5]Laboratory for Systems Biology of Human Diseases, University of Michigan, Ann Arbor, MI, USA. [6]Department of Biomedical Engineering, University of Michigan, Ann Arbor, MI, USA. [7]Biointerfaces Institute, University of Michigan, Ann Arbor, MI, USA. [8]Michigan Center for Translational Pathology, Department of Pathology, University of Michigan Medical School, Ann Arbor, MI, USA. [9]Department of Pediatrics, Division of Pediatric Hematology–Oncology, University of Michigan School of Medicine, Ann Arbor, MI, USA. [10]Rogel Cancer Center, University of Michigan Medical School, Ann Arbor, MI, USA. [11]Department of Urology, University of Michigan Medical School, Ann Arbor, MI, USA. [12]Department of Chemical Engineering, University of Michigan, Ann Arbor, MI, USA. [13]Department of Molecular and Integrative Physiology, University of Michigan, Ann Arbor, MI, USA. [14]Department of Pathology and Laboratory Medicine, Children's Hospital Los Angeles, Keck School of Medicine

University of Southern California, Los Angeles, CA, USA. [15]Anatomic Pathology and Laboratory Medicine, Children's Hospital of Philadelphia, Philadelphia, PA, USA. [16]Department of Pathology, Akron Children's Hospital, Akron, OH, USA. [17]Departments of Molecular and Integrative Physiology, Internal Medicine, and Pharmacology, University of Michigan, Ann Arbor, MI, USA. [18]Human Biology Division, Fred Hutchinson Cancer Research Center, Seattle, WA, USA. [19]Seattle Tumor Translational Research Center, Fred Hutchinson Cancer Research Center, Seattle, WA, USA. [20]Department of Pediatrics, University of Colorado Anschutz Medical Campus, Aurora, CO, USA. [21]Morgan Adams Foundation Pediatric Brain Tumor Research Program, Children's Hospital Colorado, Aurora, CO, USA. [22]Department of Neurosurgery, University of Pittsburgh School of Medicine and Cancer 97 Biology Program, UPMC Hillman Cancer Center, Pittsburgh, PA, USA. [23]Department of Neurological Surgery, University of Pittsburgh School of Medicine, Pittsburgh, PA, USA. [24]John G. Rangos Sr Research Center, Children's Hospital of Pittsburgh, Pittsburgh, PA, USA. [25]Department of Neurobiology, University of Pittsburgh, Pittsburgh, PA, USA. [26]Department of Pediatrics, Section of Hematology–Oncology, Baylor College of Medicine, Houston, TX, USA. [27]Cancer Research UK Cambridge Institute, University of Cambridge, Cambridge, UK. [28]Department of Oncology, University of Cambridge, Cambridge, UK. [29]Howard Hughes Medical Institute, University of Michigan Medical School, Ann Arbor, MI, USA. [30]Department of Internal Medicine, Division of Gastroenterology, University of Michigan, Ann Arbor, MI, USA. ✉e-mail: svenneti@med.umich.edu

Methods

Cell lines and culture methods

All cell lines were cultured in a humidified incubator under normoxia at 37 °C with 5% CO_2. Cell lines were validated by STR analysis and were routinely screened and tested negative for mycoplasma.

Mouse cell lines. Immortalized mNSCs were provided by R.J.G.[62]. RCAS-TVA control (NS-1, NS-2 and NS-3) cell lines or mouse tumour cell lines with the ZFTA–RELA fusion (H-57, H-41 and H-59)[12] were provided by E.C.H. Mouse cells were cultured in neurobasal medium (Gibco, 21103049) with 0.2% heparin solution (StemCell Technologies, 07980), 20 ng μl^{-1} EGF (Shenandoah, 100-26) and 20 ng μl^{-1} FGF-basic 154aa (Shenandoah, 100-146).

Patient-derived cell lines. EP1NS (ZFTA–RELA$^+$) cells were obtained from T. Milde[63]. EPD-210 (PFA) cells were obtained from the Brain Tumour Resource Laboratory, Fred Hutchinson Cancer Research Center. Both cell lines were grown in neurobasal medium without vitamin A (Thermo Fisher, 12587-010) with 0.2% heparin solution, 20 ng μl^{-1} EGF and 20 ng μl^{-1} FGF-basic 154aa (Shenandoah, 100-146). ST-1 (ZFTA–MAML3$^+$), ST-2 (ZFTA–RELA$^+$) and ST-4 (ZFTA–RELA$^+$, *CDKN2A*$^{-/-}$) cells were provided by K.A.M. The cell lines were cultured in neurobasal medium without vitamin A supplemented with Glutamax (Thermo Fisher Scientific, 35050-061), 200 µg ml^{-1} human EGF and 4 µg ml^{-1} human FGF and 0.2% heparin in T-75 flasks coated with poly-L-ornithine solution (Sigma-Aldrich, P4957) and laminin from Engelbreth–Holm–Swarm murine sarcoma basement membrane (Sigma-Aldrich, L2020). The CPITT-1 (ZFTA–RELA$^+$) cell line was provided by S.A. and was cultured in neurobasal medium supplemented with 0.2% heparin solution, 20 ng μl^{-1} EGF and 20 ng μl^{-1} FGF-basic 154aa. EPN1425 cells were provided by S. Mack and were cultured in DMEM medium (Gibco, 11965092) supplemented with 10% fetal bovine serum (VWR, 89510-186) and 200 mM L-glutamine (Thermo Fisher Scientific, A2916801). MAF-1329 (ZFTA–RELA$^+$) and MAF-811 (PFA) cell lines were provided by A.G. and N.K.F. and were cultured in Opti-MEM media (Gibco, 31985070) supplemented with 10% fetal bovine serum and 200 mM L-glutamine. All cell lines were cultured in media supplemented with penicillin–streptomycin (10,000 U ml^{-1}) (Thermo Fisher Scientific, 115140122) and plasmocin prophylactic (InvivoGen, antmpp).

Lentiviral-transduction-mediated gene silencing using shRNA

Isogenic mNSCs were generated by transfecting cells with ZFTA WT, RELA WT, ZFTA–RELA or EV backbone[4] using lentiviral particles (SBI LentiStarter 3.0 kit, V060A). The following lentiviral transfection protocol was used to express ZFTA WT, RELA WT, EV or ZFTA–RELA (which contains 200 bp upstream of the initiating start codon) plasmids into immortalized mNSCs. Similarly, the same protocol was used to knockdown genes with shRNAs. First, 2×10^6 HEK293T cells were plated on 100 mm dishes 36–48 h before transfection. A change of medium was performed the next day to a volume of 5 ml antibiotic-free medium. All lentiviruses were prepared using a Lentistarter 3.0 kit (System Biosciences, LV060A-1). In brief, 2 µg transfer DNA (shACOD1), 20 µg pPackH1 mix and 24 µl PureFection reagent were mixed in 500 µl serum-free DMEM medium and incubated at room temperature for 30 min. The mixture was added dropwise to HEK293T cells and gently swirled to distribute. The transfected cells were then incubated at 37 °C and 5% CO_2 to produce virus for 48 h. During this period (around 48 h before intended infection), 1×10^6 ZFTA–RELA mNSCs or EP1NS cells were plated in T-75 flasks. Lentiviral particles were then collected and filtered using a 0.45 µm PVDF filter. Next, lentiviral particles were evenly distributed onto target cells. Lentiviral medium was removed after 24 h and replaced with suitable ZFTA–RELA mNSC or EP1NS cell culture medium. After 48 h, the transfected cells were treated with the appropriate antibiotic for selection. EP1NS cells were treated with 2 µg ml^{-1} puromycin, whereas ZFTA–RELA mNSCs were selected using 15 µg ml^{-1} blasticidin. Lentiviral plasmids used for shRNA-mediated knockdown are as follows: shAcod1 (mouse, access ID: NM_008392.1) (Gentarget) and shACOD1 (human) (Horizon Discovery). The following sequences were targeted to knockdown *Acod1* in ZFTA–RELA mNSCs: shAcod1-1 (GAGAGCTTTGCTGGTATGATT) and shAcod1-2 (GAGGCATTGGCTATTGCTGTT).

The following sequences were targeted for knocking down *ZFTA–RELA* in EP1NS (ZFTA–RELA$^+$) cells. The following *ZFTA–RELA* shRNAs were custom-designed and obtained from Gentarget: shZFTA Fus-1, GCTTGCCCGCCCAAGGGCCCA; shZFTA Fus-2, AGGGCCCAGAACTGTTCCCCC; and shZFTA Fus-3, CAGAACTGTTCCCCCTCATCT.

Human *ACOD1* lentiviral cDNA (NM_001258406) and scrambled vector controls were purchased from Origene (SKU RC232825L4).

Snapshot metabolomics

To obtain a comprehensive overview of metabolites, a total of 2 million cells were cultivated in T-75 flasks and incubated for 24 h. Before metabolite collection, a complete change of medium was performed 2 h before the samples were collected. Our metabolomic analysis involved liquid chromatography with tandem mass spectrometry (LC–MS/MS) per a previously described method[64]. We used an Agilent 1290 UHPLC and 6490 Triple Quadrupole (QqQ) mass spectrometer (LC–MS) for label-free targeted metabolomic analysis. Agilent MassHunter Optimizer and Workstation software LC–MS data acquisition for 6400 series QqQ B.08.00 were used for standard optimization and data acquisition.

For each multiple reaction monitoring (MRM) transition, a retention time with a 1-min left delta and right delta was assigned. Additional parameters included a mass extraction window of 0.05 Da on both sides of the extracted *m/z*, Agile2 integrator algorithm, peak filter of 100 counts, noise algorithm RMS, noise SD multiplier of 5 min, S/N of 3, accuracy max of 20% max %Dev and quadratic/cubic Savitzky–Golay smoothing algorithm with a smoothing function width of 14 and a Gaussian width of 5.

In reversed-phase liquid chromatography (RPLC), we used a Waters Acquity UPLC BEH TSS C18 column (2.1 × 100 mm, 1.7 µm) in the positive ionization mode. Mobile phase A consisted of 0.5 mM NH_4F and 0.1% formic acid in water, whereas mobile phase B contained 0.1% formic acid in acetonitrile. The gradient program involved initially holding mobile phase B at 1% for 1.5 min, followed by an increase to 80% over 15 min, further increasing to 99% over 17 min and holding for 2 min before returning to the initial condition and holding for 10 min.

For hydrophilic interaction liquid chromatography (HILIC), we used a Waters Acquity UPLC BEH amide column (2.1 × 100 mm, 1.7 µm) in the negative ionization mode. Mobile phase A consisted of 20 mM ammonium acetate in water at pH 9.6, whereas mobile phase B comprised acetonitrile. The gradient program involved initially holding mobile phase B at 85% for 1 min, followed by a decrease to 65% over 12 min, further decreasing to 40% over 15 min and holding for 5 min before returning to the initial condition and holding for 10 min.

Both columns were maintained at a temperature of 40 °C, and each sample (3 µl) was injected into the LC–MS system with a flow rate of 0.2 ml min^{-1}. Calibration was performed using an Agilent ESI-low concentration tuning mix. Optimization was carried out on a 6490 QqQ in either the RPLC-positive or HILIC-negative mode for each of the 245 standard compounds (215 compounds for RPLC-positive and 217 compounds for HILIC-negative).

Immunoblotting

Cells were lysed in 1× RIPA buffer containing 1× protease (100× stock, Sigma Aldrich, P8340) and 1× phosphatase inhibitors (100× stock, Sigma Aldrich, P5726). Protein concentrations were quantified using colorimetric bicinchoninic acid assay (BCA) (Pierce BCA protein assay, 23227). Equal amounts of total protein from cell lysate or histone extracts were loaded on 4–15% Mini-Protean TGX precast gels

(Bio-Rad, 3450027). Proteins were transferred to PVDF membranes using a Bio-Rad Trans-Blot Turbo transfer system (Bio-Rad, 1704150). Membranes were blocked with 5% bovine serum albumin (BSA) dissolved in TBST (TBS buffer containing 0.1% Tween-20) and incubated in primary antibody diluted in 5% BSA at 4 °C overnight. The following antibodies were used in the immunoblotting experiments: RELA (Cell Signaling Technology, 8242, 1:1,000); GAPDH (Cell Signaling Technology, 2118, 1:10,000); vinculin (Sigma Aldrich, V9264, 1:40,000); ACOD1-human (Abcam, ab222411, 1:1,000 and Novus Biologicals, NBP3-06244, 1:1,000); ACOD1-mouse (Cell Signaling Technology, 17805, 1:1,000); ZFTA (C11orf95) (VWR, 89379-010, AP11349B, 1:1,000); RFP (Abcam, Ab124754, 1:1,000); MAML3 (Invitrogen, PA5-13678, 1:1,000); SLC1A5 (Cell Signaling Technology, 5345, 1:1,000); GLS-human (Cell Signaling Technology, 49363, 1:1,000); GLS-mouse (Invitrogen, PA5-35365, 1:1,000); MYC (Abcam, 32072, 1:1,000); PTEN (Cell Signaling Technology, 9559, 1:1,000); pAKT (S473) (Cell Signaling Technology, 9271, 1:1,000); AKT (Cell Signaling Technology, 4056, 1:1,000); pS6RP (S235/236) (Cell Signaling Technology, 4858, 1:1,000); S6RP (Cell Signaling Technology, 2217, 1:1,000); pGSK3α/β (Cell Signaling Technology, 9331, 1:1,000); GSK3α/β (Cell Signaling Technology, 5676, 1:1,000); H3K4me3 (Cell Signaling Technology, 9751, 1:1,000); H3K9me3 (Cell Signaling Technology, 13969, 1:1,000); H3K27Ac (Cell Signaling Technology, 8173, 1:1,000); H3K27me3 (EMD Millipore, 07-449, 1:1,000); and total H3 (Cell Signaling Technology, 3638, 1:5,000). Next, membranes were washed with TBST three times. Membranes were incubated with species-matched secondary antibodies (1:5,000), goat-anti-mouse (Bio-Rad, 1706516) or goat anti-rabbit (Bio-Rad, 1706515) conjugated to horseradish peroxidase (HRP) for 2 h at room temperature and washed with TBST 3 times (about 5 min each) and TBS one time (around 10 min). Immunoreactivity was detected using Pierce ECL Western blotting substrate (Thermo Fisher Scientific, 32106). Tumour tissues from mice were processed for immunoblotting analysis after lysing red blood cells with RBC lysis buffer (Miltenyi Biotech, 130-094-183). Uncropped and unprocessed scans of all the immunoblots in the study are provided in Supplementary Fig. 1.

IHC analysis

IHC was conducted on ZFTA–RELA$^+$ and control ependymoma patient-derived samples and on mouse tumours using established procedures. The patient tumours were classified by DNA methylation and fusions were determined by RNA-seq. For IHC of metastatic spinal cord, the vertebral column was dissected and decalcified before haematoxylin and eosin staining. Immunohistochemical staining was performed using either a Discovery XT processor from Ventana Medical Systems or a Leica Bond automated staining processor from Leica Biosystems. Each tissue section was blocked with a mixture of 10% normal goat serum and 2% BSA in PBS for 30 min. Subsequently, a rabbit monoclonal anti-ACOD1 antibody (1:200, Abcam, ab238580) or anti-PTEN (1:200, Abcam, ab170941), H3K27me3 (EMD Millipore, 07-449, 1:150), Ki-67 (Invitrogen, MA5-14520, 1:400) and SLC1A5 (Sigma Aldrich, HPA035240, 0.1 μg ml^{-1}) was applied to each section for 5 h. The tissue sections were then treated with biotinylated goat anti-rabbit IgG (PK6101, Vector Labs) at a dilution of 1:200 for 60 min. Chromogens were detected using a DAB detection kit along with streptavidin–HRP and blocker D to minimize background signal (Ventana Medical Systems) following the manufacturer's instructions. Afterwards, each section was mounted, dried and visualized using an Aperio Vista scanning system (AperioScanscope Scanner). The accompanying Aperio ImageScope software program was used to view each slide at ×40 magnification. An experimenter, who was unaware of the study design, captured JPEG images from three randomly selected areas of each control-stained and ZFTA–RELA-stained section. To quantify the images, an automated analysis program previously published by our laboratory[65] was used. This MatLab-based program uses techniques such as *k*-means clustering, colour segmentation based on RGB colour differentiation and Otsu's threshold-based background–foreground separation. It generates a quantitative score by multiplying the extracted pixels with the average intensity for each JPEG image.

Cumate-inducible ZFTA–RELA fusion system

The SPARQ 2 Cumate Switch system (System Biosciences, QM822B-1) was used to design the inducible ZFTA–RELA fusion model. The EV and ZFTA–RELA fusion plasmids were transduced in both mNSCs and in HEK293T cells via lentiviral transfection as described above. Cumate (10,000×) purchased from System Biosciences (PBQM100A-1) was used at 1× concentration for 48 h to induce expression of either EV or the ZFTA–RELA fusion.

KDM5 activity measurement

Assessment of KDM5 enzyme activity was performed using a JARID1A Homogenous Assay kit (BPS Bioscience, 50510-2) following the manufacturer's instructions in three independent experiments. For enzymatic inhibition, KDM5 enzyme (25ng μl^{-1}) was incubated in quadruplicate with different concentrations (100, 250, 500, 1,000, 2,000, 5,000 or 10,000 μM) of itaconic acid (Sigma-Aldrich, I29204), D-2G (Cayman, 16366) or L-2HG (Cayman, 16367). For enzymatic activation, KDM5 enzyme at different concentrations (1.5, 3.0, 6.5, 12.5 or 25.0 ng μl^{-1}) was incubated in quadruplicate with 2,000 μM αKG (Sigma-Aldrich, 349631), 2,000 μM itaconic acid (Sigma-Aldrich, I29204), 2,000 μM D-2HG (Cayman, 16366) or 1,000 μM L-2HG (Cayman, 16367). Compounds were diluted in either PBS or DMSO, which were also used as negative controls. Assays were read in an Envision plate reader (PerkinElmer) using the AlphaLisa 615/Alphascreen 444 method.

ChIP–seq

ZFTA–RELA mNSCs and EPN1425 cells were seeded at a density of 2×10^6 cells in a 100 mm dish and treated with 10 mM dimethyl citraconate (TCI, C0364) or DMSO for 24–48 h. Following this, the cells were detached and dissociated using Accutase (Corning, 25-058-CI). ChIP experiments were performed per the manufacturer's protocol using an Ideal ChIP–seq kit for transcription factors (Diagenode). For histone ChIPs, 1 million cells were used per ChIP reaction with 2 μg antibody. In brief, cells were crosslinked for 10 min in a 1% formaldehyde solution, followed by quenching with 1/10 the volume of 1.25 M glycine for 5 min at room temperature. Following this, the cells were lysed and sonicated (Bioruptor Pico, Diagenode) to a desired chromatin size of about 200 bp using the Easy mode cycle. Sheared chromatin was then incubated with the following antibodies overnight at 4 °C: H3K4me3 (CST, 9751S) and H3K27me3 (Millipore, 07-449). ChIP DNA was de-crosslinked and purified the next day using a Diagenode iPure kit V3 following the manufacturer's protocol. Purified DNA was prepared for sequencing using the manufacturer's instructions (Illumina). About 1–10 ng ChIP DNA was converted to blunt-ended fragments using T4 DNA polymerase, *Escherichia coli* DNA polymerase I large fragment (Klenow polymerase) and T4 polynucleotide kinase (New England Biolabs (NEB)). Klenow fragment (3′ to 5′ exo minus; NEB) was used to add a single adenine base to fragment ends, followed by ligation of Illumina adaptors (Quick ligase, NEB). PCR enriched the adaptor-ligated DNA fragments using Illumina Barcode primers and Phusion DNA polymerase (NEB). PCR products were size-selected using 3% NuSieve agarose gels (Lonza), followed by gel extraction using QIAEX II reagents (Qiagen). Quantified libraries were quality-checked using a Bioanalyzer 2100 (Agilent) and sequenced on an Illumina HiSeq 2500 Sequencer (125-nucleotide read length).

Reads were processed as previously described[66]. To summarize, reads were first processed using Trimmomatic (v.0.39) (settings TruSeq3-PE-2.fa:2:30:10, minlen 50) followed by alignment with bwa (bwa mem, options -5SP -T0, v.0.7.17-r1198-dirty) to the mm10 (GRCm38) genome reference or the hg38 (GRCh38) reference[67,68]. After alignment, the reads were filtered using MarkDuplicates from Picard and then by a quality score of >20 using SAMtools[69]. MACS2 was used to call peaks, filtered using bedtools and converted to bigwigs with UCSC wigtoBigwig[70,71]. Cistrome overlap analysis was performed in R (v.3.6.0) using ChipSeekAnno (v.3.0.0) and ChipSeeker (v.1.29.1)[72,73]. Enrichment heatmaps were generated using DeepTools[74].

ATAC-seq

ATAC-seq was performed as previously described[75]. In brief, 50,000 mNSC and EPN1425 cells were washed in cold PBS and resuspended in lysis buffer (10 mM Tris HCL, pH 7.4, 10 mM NaCl, 3 mM $MgCl_2$, digitonin, NP-40, Tween-20 and protease and phosphatase inhibitor). This single-cell suspension was incubated on ice for 5 min with gentle mixing by pipetting every 2 min, followed by quenching in resuspension buffer. The lysate was centrifuged at 1,300*g* for 5 min at 4 °C. Nuclei were resuspended in a 50 µl reaction containing 25 µl of 2× TD buffer and 1 µl Tn5 enzyme for 30 min at 37 °C using a Nextera DNA Library Preparation kit. Samples were immediately purified using a Qiagen minElute column and PCR-amplified with NEBNext High-Fidelity 2× PCR master mix (NEB, M0541L). Optimal PCR cycles were determined by qPCR, and the amplified libraries were further purified using a Qiagen minElute column and SPRI beads (Beckman Coulter). Libraries were quantified and quality checked using a Bioanalyzer 2100 (Agilent).

The ATAC-seq libraries were sequenced on an Illumina HiSeq 2500 platform, using a 2 × 50-nucleotide paired-end read length with a sequence depth of 40–45 million. Sequencing of ATAC-seq libraries generated fastq files, which were initially processed using Trimmomatic (v.0.39) for trimming[67]. These files were then aligned to the mm10 (GRCm38) mouse genome reference or the hg38 (GRCh38) reference using bwa mem (v.0.7.17-r1198-dirty)[67], and the alignments were converted to binary format with SAMtools (v.1.9)[68]. Next, we eliminated mitochondrial and duplicated reads using SAMtools and Picard MarkDuplicates (v.2.26.0-1-gbaf4d27-SNAPSHOT)[69]. Peaks in the ATAC-seq data were identified using MACS2 (v.2.1.1.20160309)[70]. Finally, the conversion of data to bigwig format was accomplished using the UCSC tool wigtoBigwig[71]. The enrichment heatmaps were generated using DeepTools[74].

RNA-seq

RNA was isolated from 1×10^6 cells seeded in 100 mm dishes using Trizol (Invitrogen 15596-026) and treated with DNase (Sigma, 9003-98-9). RNA-seq libraries were prepared according to the Illumina TruSeq protocol and were sequenced on a HiSeq 2000. RNA-seq data generated were aligned to the mouse reference genome using bowtie and analysed using the RSEM software package with default parameters. DEseq2 was used to identify differentially upregulated and downregulated genes[76]. Differentially enriched pathways were identified using Enrichr (https://maayanlab.cloud/Enrichr/)[77].

Generation of the ZFTA–RELA KDM5δ mutant

The following sequences with RFP tags were transfected into mNSCs to derive ZFTA–RELA and ZFTA–RELA KDM5δ cells (shown in Fig. 3 and Extended Data Fig. 5). Putative KDM5 recognition sites in the ZFTA portion of the fusion were identified based on previous studies[36,37,39] and mutated as indicated below.

The KDM5A site in *ZFTA* exon 1, normally CCGCCC, was changed to CCACCA. The KDM5B site in *ZFTA* exon 2, normally GCACAC, was changed to GCAAAC. In detail, the parts of the sequence involved are highlighted in bold:

ZFTA–RELA unaltered: GATCCC**ATG**GAGCCCGGCGGGGACCACCGTAAGAGCCGGAGCAGCGGCGGCAGGGGCGGCCCCGGGCCAGCAGTGGCCTCGGCACGGGGCCGACGGCTG**CCGCCC**GCCGGATCGAGCGGCAGCGCGGAGCCAGAGGAAGACGAAGGCGGGCAAGATCTTCAGCTGGAAGGGGGTGCCTTGGGGTCCTGGGGGAGTGCCCCCCTGCCCTCCTCCAGGGCCAGGGGACCAGCATCTTCAGGCAGGAAATATTCAGACCACTGTGAGGCCCGGGCCTCGAGGCCTGGAAAGAGCCGCATCCCTGGCCGTGACCACCGGCGCTACTACCACGACCACTGGCGGCTGGAGTACCTGATGGACTTCAACCCTGCCCGGCACGGCATGGTGTGCATGGTGTGCGGCAGCTCCCTGGCCACCCTCAAGCTCAGCACCATCAAGCGCCACATCCGCCAAAAGCACCCCTACTCCTTGCATTGGAGTCCCCGGGAGAAGGAAGTCATCAGCAACAGCTGGGAT**GCACAC**ATGGGGCTGGGGGCCTGCGGAGAGGCCGAGGGCCTGGGGGTCCAGGGGGCTGAGGAGGAGGAGGAGGAGGAAGAAGAGGAGGAGGAGGAGGGGGCCGGTGTCCCAGCTTGCCCGCCCAAGGGCCCAG.

ZFTA–RELA KDM5δ: GATCCC**ATG**GAGCCCGGCGGGGACCACCGTAAGAGCCGGAGCAGCGGCGGCAGGGGCGGCCCCGGGCCAGCAGTGGCCTCGGCACGGGGCCGACGGCTG**CCACCA**GCCGGATCGAGCGGCAGCGCGGAGCCAGAGGAAGACGAAGGCGGGCAAGATCTTCAGCTGGAAGGGGGTGCCTTGGGGTCCTGGGGGAGTGCCCCCCTGCCCTCCTCCAGGGCCAGGGGACCAGCATCTTCAGGCAGGAAATATTCAGACCACTGTGAGGCCCGGGCCTCGAGGCCTGGAAAGAGCCGCATCCCTGGCCGTGACCACCGGCGCTACTACCACGACCACTGGCGGCTGGAGTACCTGATGGACTTCAACCCTGCCCGGCACGGCATGGTGTGCATGGTGTGCGGCAGCTCCCTGGCCACCCTCAAGCTCAGCACCATCAAGCGCCACATCCGCCAAAAGCACCCCTACTCCTTGCATTGGAGTCCCCGGGAGAAGGAAGTCATCAGCAACAGCTGGGAT**GCAAAC**ATGGGGCTGGGGGCCTGCGGAGAGGCCGAGGGCCTGGGGGTCCAGGGGGCTGAGGAGGAGGAGGAGGAGGAAGAAGAGGAGGAGGAGGAGGGGGCCGGTGTCCCAGCTTGCCCGCCCAAGGGCCCAG.

ChIP–PCR

ZFTA–RELA mNSCs and EPN1425 cells were seeded at a density of 5×10^6 cells in a 100 mm dish and treated with 10 mM dimethyl citraconate (TCI, C0364) or DMSO for 48 h. Chromatin fragmentation was achieved by sonication (QSonica, 800R) and by micrococcal nuclease (Cell Signaling Technologies, 10011) digestion to a final size of 150–300 bp. ChIP was performed using a Simple Chip Enzymatic Chromatin IP kit (Cell Signaling Technologies, 9002) and a Simple Chip Plus Sonication Chromatin IP kit (Cell Signaling Technologies, 56383) as per the manufacturer's protocols.

Two independent set of primers were designed and used for the ChIP PCR and RT–qPCR experiments shown in Fig. 3h and Extended Data Fig. 5e,f,j. They were custom designed and obtained from Integrated DNA Technologies (IDT). The following *ZFTA*-based primers were used: *ZFTA* exon 5 set 1 FWD: 5′-AGAGGAGGACGAAGAGGAC-3′; *ZFTA* exon 5 set 1 REV: 5′-CCGTCGTAGTCCATCAGGTA-3′; *ZFTA* exon 5 set 2 FWD: 5′-TGAGGAGCGCCAGACTAT-3′; *ZFTA* exon 5 set 2 REV: 5′-CACACAGCGCCAGACTT-3′; *ZFTA* exons 1–2 set 1 FWD: 5′-GAGCCAGAGGAAGACGAAGG-3′; and *ZFTA* exons 1–2 set 1 REV: 5′-GAAGATGCTGGTCCCCTG-3′. The following *RELA*-based primers were used: *RELA* exon 4 set 1 FWD: 5′-ACAGGACCAGGGACAGT-3′; *RELA* exon 4 set 1 REV: 5′-CTCAGCCTCATAGAAGCCATC-3′; *RELA* exon 4 set 2 FWD: 5′-CGCATCTCCCTGGTCAC-3′; and *RELA* exon 4 set 2 REV: 5′-CAT CCC GGC AGT CCT TT-3′. The following mouse primers were used: *H3f3a* FWD: 5′-ACAAAAGCCGCTCGCAAGAGTG-3′; and *H3f3a* REV: 5′-TTCTCGCACCAGACGCTGAAAG-3′.

RT–qPCR

RNA was isolated from 1×10^6 cells seeded in 100 mm dishes using Trizol (Invitrogen 15596-026) and treated with DNase (Sigma, 9003-98-9) per the manufacturer's instructions. qPCR was performed with $n = 5$ samples of 20 ng mRNA each using a TaqMan RNA-to-C_T kit (Applied Biosystems, 4392938). TaqMan probes (Thermo Fisher) targeting mouse *Pten* (Mm00477208), human *PTEN* (Hs02621230), human *GAPDH* (Hs99999905, Thermo Fisher Scientific, 4326317E) and mouse *Gapdh* (Mm99999915_g1, Thermo Fisher Scientific, 4352339E) were used. The following primers from IDT were used to detect *ZFTA–RELA* mRNA in patient-derived cell lines (shown in Fig. 1m): fusion set 1 FWD: 5′-GAGGAGGAGGAGGAAGAAGAG-3′; fusion set 1 REV: 5′-GCTGCTCAATGATCTCCACATA-3′; fusion set 2 FWD: 5′-GAAGAAGAGGAGGAGGAGGAG-3′; and fusion set 2 REV: 5′-CTTGGGCTGCTCAATGATCT-3′.

RT–qPCR was conducted using an ABI7900HT Sequence Detection system, and relative expression was calculated using the $2^{-\Delta\Delta C_T}$ method, with *Gapdh* (mouse) or *TBP* (human) as a housekeeping control for normalization.

Glutamine uptake and intracellular glutamine and glutamate measurement

Glutamine uptake and intracellular glutamine levels were estimated using a Glutamine/Glutamate-glo assay kit (Promega, J8022). In brief, 25,000 cells per ml medium per well were seeded in triplicate in a 24-well plate for each time point as indicated. Both cell culture media and cells were collected at 0, 12, 24, 36, 48, 60 and 72 h. Following extraction, intracellular and extracellular glutamine and glutamate were measured by bioluminescence detection for all the time points. The concentrations of glutamine and glutamate were calculated using the standards provided by the manufacturer. The values obtained were used to estimate percentage glutamine uptake and intracellular glutamate to glutamine ratios.

Isotope tracing of radiolabelled glucose and glutamine

For ^{13}C tracing, 2 million cells were plated and cultured using medium supplemented with either ^{13}C-U-labelled glucose (25 mM) or glutamine (2 mM, both from Cambridge Isotope Laboratories, CLM-99-1396-1 and CLM-1822-H, respectively) for 16 h. Cells were collected by centrifugation and the medium was aspirated. The cell pellet was resuspended in 300 µl ice-cold methanol followed by thorough pipetting. Next, 300 µl water containing 1 µg norvaline as internal standard and 600 µl chloroform was added to the microfuge tube. The extracts were vortexed thoroughly for 30 min at 4 °C, followed by centrifugation. The polar layer was dried in a SpeedVac for 3–4 h without heat and stored at −80 °C. For derivatization, 30 µl methoxyamine hydrochloride (Fisher Scientific, PI45950) was added to the dried samples and incubated at 45 °C for 30 min with constant mixing. Next 30 µl MBTSTFA and 1% TBDMCS (Sigma Aldrich, M-108-1243 5×1ML) was added, and samples were incubated at 45 °C for 1 h. Derivatized samples were transferred to GC vials with glass inserts. Samples were analysed using an Agilent 7890 GC equipped with a 30-m HP-5MSUI capillary 1246 column connected to an Agilent 5977B MS in scan mode. In total, a 1–2 µl sample was injected at 270 °C with helium as the carrier gas at 1 ml min^{-1} flow. The temperature gradient was maintained at 100 °C for 1 min, increased at 3.5 °C min^{-1} to 255 °C, increased to 320 °C at 15 °C min^{-1} and held for 3 min (method total time of 52.6 min). MS detector was operated in scan mode (70–600 *m/z*). Relative metabolite abundances were calculated by normalizing the integrated peak area of ions to the internal standard signal (norvaline) and protein content. For ^{13}C-labelled samples, isotopic correction of raw GC–MS peaks for all reported metabolites was performed using the IsoCorrectoR package (v.1.5.1) available as part of the Bioconductor library (BioC 3.8) and implemented in R (CRAN 3.6.1).

Cell proliferation and viability assays

Proliferation and viability of cells after drug treatment was assessed by trypan blue exclusion assays. Cells were seeded at a density of 2.5×10^4 cells per well in a 24-well plate and were left overnight. They were then treated with vehicle or drug (JHU-083, V-9302, CB-839 or PI-103) at varying concentrations and time points for the indicated time periods, following which they were counted using a Countess III cell counter (Thermo Fisher Scientific). Cell number (*y* axis) for each cell line was calculated as a percentage of living cells normalized to the untreated or vehicle-treated controls (average number of cells alive in the untreated or vehicle-treated wells).

Chemical compounds

The drugs and chemical compounds used in the study are listed as follows: dimethyl citraconate (Fisher Scientific, C0364-5G), mesaconic acid (Millipore-Sigma, 131040-10G), itaconic acid (Sigma Aldrich, I29204), dimethyl 2-ketoglutarate (Cayman Chemical, 28394), octyl-L-2-hydroxyglutarate (Cayman Chemical, 16367), LPS (Cayman Chemical, 19661), IRG1-IN-1 (MedChem Express, HY-148335), GSK-343 (Cayman Chemical, 14094), CPI-455 (Cayman Chemical, 22127), DON (Cayman Chemical, 17580), JHU-083 (MedChem Express, HY-122218), V-9302 (Selleckchem, S8818), CB-839 (MedChem Express, HY-12248), PI-103 (Selleckchem, S1038), MK-2206 (Cayman Chemical, 11593) and DMSO (Sigma Aldrich, D2650).

Histone extraction

Cells were plated at densities below confluence. Following the specified treatment, cells were rinsed with PBS. The cell pellet resulting from centrifugation was resuspended in 1 ml hypotonic lysis buffer (containing 10 mM Tris HCl pH 8.0, 1 mM KCl, 1.5 mM $MgCl_2$ and protease and phosphatase inhibitors) and incubated for 30 min on a rotator at 4 °C. The pellet was then collected by centrifugation at 10,000*g*, 4 °C for 10 min. It was subsequently resuspended in 400 µl of 0.4 N H_2SO_4 and left to incubate overnight on a rotator at 4 °C. After centrifugation, the resulting supernatant was transferred to a new tube, and 132 µl trichloroacetic acid was gradually added. The mixture was then incubated on ice for 30 min. The histone pellet was obtained by centrifugation at 16,000*g*, 4 °C for 10 min and washed with cold acetone. After another round of centrifugation at 16,000*g*, 4 °C for 5 min, acetone was removed. The histone pellet was further washed with acetone and subsequently allowed to air dry with the caps open at room temperature for 20 min to eliminate any remaining acetone. Finally, the dried histone pellet was resuspended in an appropriate volume of ddH_2O, supplemented with protease inhibitors and kept on ice.

Animal handling and housing conditions

Animal experiments were performed after approval from the University of Michigan Committee on the Use and Care of Animals (PRO00010599) and were conducted as per National Institutes of Health (NIH) guidelines for animal welfare. All animals used in these studies were housed in pathogen-free conditions as per IACUC guidelines with continuous access to both food and water in addition to veterinary care. NOD-SCID-IL2R γ-chain deficient (NSG) mice (NOD.Cg-*Prkdc*scid *Il2rg*tm1Wjl/SzJ, 005557) aged 4–6 weeks old were used for all experiments involving subcutaneous or orthotopic injections of ZFTA–RELA mNSCs and for the subcutaneous MAF-1329 and MAF-811 PDX models. IUE models were CD-1 (Charles River, Crl:CD1(ICR), 022) or C57BL/6 animals (The Jackson Laboratory, 003771). For all drug trials, the animals were randomized and sorted into treatment groups in an unbiased manner, ensuring that all cohorts contained equal proportions of male and female animals.

Nes^{cre}Acod1$^{fl/+}$ models

Acod1$^{fl/fl}$ animals were provided by M. Diamond[25]. B6.Cg.Tg.(Nes Cre)1KlnJ animals were crossed with *Acod1$^{fl/fl}$* animals. The pups were weaned after 21 days and genotyped to establish *Nes^{cre}Acod1$^{fl/+}$* mice.

Subcutaneous ZFTA–RELA xenograft models

In this study, two subcutaneous xenograft models (mouse and human patient-derived) ZFTA–RELA fusion tumours were established in NSG mice. Xenograft models were generated by injecting 1×10^6 ZFTA–RELA mNSCs on either flank of the animal and tumour volumes were measured once palpable tumours (around 200 mm^3) appeared (about 1 week after injection). MAF-1329 (ZFTA–RELA$^+$) and MAF-811 PDXs were provided by A.G. and N.K.F. PDX cells were injected in NSG mice and were allowed to grow. Once the tumours reached the end-point volumes of 1,000–1,500 mm^3, they were excised and homogenized into single-cell suspensions using a gentleMACS Octo dissociator (Miltenyi Biotech, 130-096-427), following which they were counted and serially passaged in NSG animals to generate a suitably sized cohort for the trial. For subcutaneous tumours, growth was measured using Vernier calipers, and tumour volumes were calculated using the formula $L \times W \times W/2$, where L is the longer dimension and W is the shorter dimension of the tumour. At the end point, the animals were humanely euthanized and perfused before collecting the tumour tissues. Tumour volumes were not allowed to exceed these limits (as per IACUC guidelines) in any of the experiments.

Orthotopic ZFTA–RELA tumour models

Orthotopic models of ZFTA–RELA tumours were established in NSG animals by injecting 2×10^5 ZFTA–RELA bioluminescent mNSCs in the cortex, 3 mm posterior and 2 mm lateral right from the bregma using a stereotaxic apparatus. Before implantation, mice were anaesthetized by intraperitoneal injection of ketamine (90 mg kg^{-1}) and dexmedetomidine (0.6 mg kg^{-1}). Carprofen (5.5 mg kg^{-1}) was used as an analgesic to alleviate pain after surgery. A total volume of 4 µl of cells resuspended in sterile PBS was injected using a Hamilton syringe through a burr hole drilled at the location described. The surgery site was treated with iodine and sealed with a wound clip to avoid infection. The animals were then revived using atipamezole (1.25 mg kg^{-1}).

IUE ZFTA–RELA tumour models

IUE ZFTA–RELA immunocompetent ependymoma animal models were established using previous protocols to generate piggy-bac (PB) ZFTA–RELA plasmids containing the luciferase gene along with the plasmid transposase (PBase)[6,10,11]. Pregnant CD1 or B6 mice (Charles River) mice at embryonic day 15 were used. IUE was performed by injecting a concentrated mixture of DNA (1 µg μl^{-1} ZFTA–RELA plasmid) along with 0.05% Fast Green (Sigma) into the lateral ventricle of the embryos using a pulled glass capillary pipette. Electroporation was performed using 5 square pulses (45 V, 50 ms pulses with 950 ms intervals) and applied using a 3 mm tweezer electrode, with the positive electrode directed towards the cortex (BTX/Harvard Bioscience). After the procedure, the embryos were carefully placed back into the abdominal cavity, the incision was sutured, and the female mouse was monitored until she fully recovered.

Pharmacological and radiation treatment

In both the implantation and IUE models, tumour engraftment and establishment was verified by bioluminescence measurements. The flux density was calculated, and treatment regimens were initiated only after tumours were established (predefined as $>10^5$ photons s^{-1}). Two independent baseline measurements were recorded for every animal in the trial to ensure tumour growth and to avoid possible technical artefacts. Subsequent bioluminescent readings were normalized to the baseline measurements to calculate the fold change in the signal to assess tumour progression. The glutamine antagonist JHU-083 was dissolved in 10% DMSO and 90% corn oil to be dosed orally at 20 mg kg^{-1} twice a week. The dual PI3K–mTOR inhibitor was dissolved in DMSO and was i.p. injected every other day during weekdays with scheduled breaks in treatment on the weekend. Dimethyl citraconate was prepared in sterile saline solution was i.v. injected on alternate days for the entire duration of the treatment paradigm. For experiments involving radiotherapy, whole-brain irradiation was performed on mice twice per week (single fraction of 2 Gy per day) for two consecutive weeks.

Bioluminescence measurement and analysis

Successful tumour formation was verified by checking for bioluminescence after injecting the pups with luciferin (15 mg ml^{-1}, GoldBio, LUCK 115144-35-9) using an IVIS spectrum (Perkin Elmer) instrument. Once anaesthetized, a sequence of bioluminescence images was recorded to capture the peak flux intensity value for each animal. This value was then used to normalize to baseline for fold change calculation. In the implantation model in which ZFTA–RELA tumours metastasized to the spinal cord, the fold change in tumour bioluminescence signal was calculated by defining a region of interest around the spinal cord distal and distinct to the head. The end points of the animal trial were defined based on IACUC guidelines and animal welfare was prioritized. Swelling of the head, lack of mobility, loss of weight or appetite, among other parameters, were all considered as key criteria for euthanasia of tumour-bearing animals. Tumour volumes were not allowed to exceed these limits (as per IACUC guidelines) in any of the experiments.

Statistics and reproducibility

The Department of Bioinformatics provided consultation for the statistical analyses conducted. Each figure and its corresponding legend indicate the sample size (n), the specific statistical test performed and the corresponding P values. No data were excluded in analyses of samples or animals. Owing to the rarity of ZFTA–RELA ependymomas, the sample sizes were determined based on the available tumour samples. The figure legends provide the exact n value for each experiment. The data are presented as the mean ± s.d., and the box and whisker plots show the maximum, mean and minimum values. Graphs were generated and statistical analyses were performed using Prism software (v.9.5.1, GraphPad). The data analysis methods included unpaired, two-sided, two-tailed Student's t-test, one-way or two-way ANOVA followed by post hoc Bonferroni multiple comparison analysis along with Dunnett's correction, as indicated in each figure. Data in Fig. 1h was analysed using nonparametric Spearman's correlation with 95% confidence intervals and correlation coefficient (R^2) and P values are indicated.

Overall survival data, including data from animal models, were visualized using Kaplan–Meier curves and the association of various factors with overall survival was assessed using the log-rank test. Data were considered significant if P values were below 0.05 (95% CI).

Data shown in the following figures are representative images of independent experiments or samples as indicated. Fig. 1e ($n = 3$ independent experiments), Fig. 2a ($n = 5$ independent experiments), Fig. 2g ($n = 2$ independent experiments), Fig. 2h ($n = 2$ independent experiments), Fig. 2j ($n = 2$ independent experiments), Fig. 3b ($n = 2$ independent experiments), Fig. 3c ($n = 2$ independent experiments), Fig. 3h ($n = 5$ independent experiments), Fig. 3l ($n = 2$ independent experiments), Fig. 5c ($n = 2$ independent experiments), Fig. 5j ($n = 3$ independent samples were used for immunohistochemical staining), Extended Data Fig. 1e ($n = 2$ independent experiments), Extended Data Fig. 1f (ZFTA–RELA ($n = 18$ independent samples), non-ZFTA fusion ($n = 5$ independent samples), posterior fossa type A ($n = 7$ independent samples), posterior fossa type B ($n = 2$ independent samples), spinal ($n = 3$ independent samples) and myxopapillary ($n = 4$ independent samples) of ependymoma tumours from patients). Extended Data Fig. 1h ($n = 3$ independent experiments), Extended Data Fig. 1i ($n = 3$ independent experiments), Extended Data Fig. 1l ($n = 2$ independent experiments), Extended Data Fig. 3a ($n = 5$ independent experiments), Extended Data Fig. 3b ($n = 2$ independent experiments), Extended Data Fig. 3c ($n = 2$ independent experiments), Extended Data Fig. 3d ($n = 2$ independent experiments), Extended Data Fig. 3e ($n = 2$ independent experiments), Extended Data Fig. 3f ($n = 2$ independent experiments), Extended Data Fig. 3h ($n = 3$ independent experiments), Extended Data Fig. 3i ($n = 2$ independent experiments), Extended Data Fig. 3j ($n = 2$ independent experiments), Extended Data Fig. 3k ($n = 2$ independent experiments), Extended Data Fig. 3l ($n = 2$ independent experiments), Extended Data Fig. 3m ($n = 2$ independent experiments), Extended Data Fig. 3n ($n = 3$ independent experiments), Extended Data Fig. 3o ($n = 2$ independent experiments), Extended Data Fig. 5c ($n = 3$ independent experiments), Extended Data Fig. 5d ($n = 3$ independent experiments), Extended Data Fig. 5e ($n = 2$ independent experiments), Extended Data Fig. 5f ($n = 2$ independent experiments), Extended Data Fig. 5n ($n = 2$ independent experiments), Extended Data Fig. 7b ($n = 2$ independent experiments), Extended Data Fig. 7c ($n = 2$ independent experiments), Extended Data Fig. 7d ($n = 2$ independent experiments), Extended Data Fig. 8c ($n = 2$ independent experiments), Extended Data Fig. 8d ($n = 2$ independent experiments), Extended Data Fig. 8h ($n = 2$ independent experiments), Extended Data Fig. 8i ($n = 3$ independent samples each for mouse ZFTA–RELA fusion tumours and cortex tissues, $n = 18$ independent samples for ZFTA–RELA$^+$ tumours from patients and $n = 5$ independent samples for non-ZFTA (YAP1) fusion tumours from patients), Extended Data Fig. 8m ($n = 2$ independent experiments), Extended Data Fig. 9c ($n = 17$ independent samples for ZFTA–RELA$^+$ tumours from patients and $n = 5$ independent samples for non-ZFTA (YAP1) fusion tumours from patients), Extended Data Fig. 9i ($n = 2$ independent experiments), Extended Data Fig. 9j ($n = 2$ independent experiments), Extended Data Fig. 9k ($n = 2$ independent experiments), Extended Data Fig. 10b ($n = 2$ independent experiments), Extended Data Fig. 11d ($n = 3$ independent experiments), Extended Data Fig. 12m ($n = 3$ independent samples).

Reporting summary

Further information on research design is available in the Nature Portfolio Reporting Summary linked to this article.

Data availability

The ChIP–seq and ATAC-seq data generated in this study are accessible through the NCBI Gene Expression Omnibus (GEO) database with the series accession numbers GSE294954 and GSE294955. Gene expression data shown in Extended Data Figs. 7f and 8j were derived from a previous study[3] and were downloaded from the NCBI GEO database with the accession number GSE64415. Single-cell RNA-seq data shown in Extended Data Figs. 7g and 8k are from a previous study[43] and were downloaded using the accession number GSE141460. Data in Fig. 4g and Extended Data Fig. 8g,l were derived from a paediatric ependymoma dataset from cBioPortal (https://pedcbioportal.kidsfirstdrc.org/; GEO accession GSE50385). Source data are provided with this paper.

62. Johnson, R. A. et al. Cross-species genomics matches driver mutations and cell compartments to model ependymoma. *Nature* **466**, 632–636 (2010).
63. Milde, T. et al. A novel human high-risk ependymoma stem cell model reveals the differentiation-inducing potential of the histone deacetylase inhibitor Vorinostat. *Acta Neuropathol.* **122**, 637–650 (2011).
64. Lee, H. J., Kremer, D. M., Sajjakulnukit, P., Zhang, L. & Lyssiotis, C. A. A large-scale analysis of targeted metabolomics data from heterogeneous biological samples provides insights into metabolite dynamics. *Metabolomics* **15**, 103 (2019).
65. Panwalkar, P. et al. Immunohistochemical analysis of H3K27me3 demonstrates global reduction in group-A childhood posterior fossa ependymoma and is a powerful predictor of outcome. *Acta Neuropathol.* **134**, 705–714 (2017).
66. Parolia, A. et al. NSD2 is a requisite subunit of the AR/FOXA1 neo-enhanceosome in promoting prostate tumorigenesis. *Nat. Genet.* **56**, 2132–2143 (2024).
67. Bolger, A. M., Lohse, M. & Usadel, B. Trimmomatic: a flexible trimmer for Illumina sequence data. *Bioinformatics* **30**, 2114–2120 (2014).
68. Li, H. & Durbin, R. Fast and accurate short read alignment with Burrows–Wheeler transform. *Bioinformatics* **25**, 1754–1760 (2009).
69. Danecek, P. et al. Twelve years of SAMtools and BCFtools. *Gigascience* **10**, giab008 (2021).
70. Zhang, Y. et al. Model-based analysis of ChIP–Seq (MACS). *Genome Biol.* **9**, R137 (2008).
71. Raney, B. J. et al. The UCSC Genome Browser database: 2024 update. *Nucleic Acids Res.* **52**, D1082–D1088 (2024).
72. Zhu, L. J. et al. ChIPpeakAnno: a Bioconductor package to annotate ChIP–seq and ChIP–chip data. *BMC Bioinformatics* **11**, 237 (2010).
73. Yu, G., Wang, L. G. & He, Q. Y. ChIP seeker: an R/Bioconductor package for ChIP peak annotation, comparison and visualization. *Bioinformatics* **31**, 2382–2383 (2015).
74. Ramírez, F., Dündar, F., Diehl, S., Grüning, B. A. & Manke, T. DeepTools: a flexible platform for exploring deep-sequencing data. *Nucleic Acids Res.* **42**, W187–W191 (2014).
75. Buenrostro, J. D., Giresi, P. G., Zaba, L. C., Chang, H. Y. & Greenleaf, W. J. Transposition of native chromatin for fast and sensitive epigenomic profiling of open chromatin, DNA-binding proteins and nucleosome position. *Nat. Methods* **10**, 1213–1218 (2013).
76. Love, M. I., Huber, W. & Anders, S. Moderated estimation of fold change and dispersion for RNA-seq data with DESeq2. *Genome Biol.* **15**, 550 (2014).
77. Kuleshov, M. V. et al. Enrichr: a comprehensive gene set enrichment analysis web server 2016 update. *Nucleic Acids Res.* **44**, W90–W97 (2016).

Acknowledgements We thank M. Diamond for providing the *Acod1*$^{-/-}$ and *Acod1*$^{fl/fl}$ animals; A. Jassim for providing the ZFTA–RELA plasmids and access to data; J. Presner, L. A. O'Neill, M. Artyomov and M. Diamond for their feedback on the manuscript; C. Sivakumar and G. McIntyre for their help in the study; staff at the Morgan Adams Foundation for supporting the development of the MAF-1329 and MAF-811 cell lines used in the study; and staff at the Chad Carr Pediatric Brain Tumor Center at the University of Michigan for their support. This work was funded by the Sontag Foundation (S.V.), Clinical Scientist Development Award–Doris Duke Charitable Foundation (S.V.), the Hyundai Hope On Wheels Foundation (S.V.), NINDS R01NS110572 (S.V.), NCI R01CA261926 and the Julie Taubman Reys emerging scholar award from the University of Michigan Taubman Institute (S.V.). The Venneti Laboratory is/was supported by grants from Mathew Larson (S.V.), Sidney Kimmel (S.V.), St Baldrick's (S.V.), Claire McKenna (S.V.), Chad Tough (S.V.), Alex's Lemonade Stand (S.V.), Storm The Heavens (S.V.) and the University of Michigan Chad Carr Pediatric Brain Tumor Initiative (S.V.). S.K.N. was supported by the Momental Foundation and is currently funded by the Michigan Pioneer Fellows Program, the ChadTough Defeat DIPG, the Alvin L. Glick Foundation, an Alex's Lemonade Stand Foundation Young Investigator Award (grant 1454502) and an AACR-SONTAG Foundation Brain Cancer Research Fellowship (25-40-78-NATA). C.K. acknowledges the following funding sources: NIH grants R01-NS119231 and R01-NS124607, and DOD grant CA201129P1. A.M.C. acknowledges funding from NIH grant R35CA231996. A.M.C. is a Howard Hughes Medical Institute Investigator, an A. Alfred Taubman Scholar and an American Cancer Society Professor.

Author contributions S.K.N. and S.V. designed and conceptualized the study. S.K.N. and S.V. analysed the data and wrote the manuscript. J.L., J.H.S., M.N., S.E., M.M., J.M.B., A.D., M.P., S.R.S., S.H., Q.Z., R.M., O.A., P.N., S.S., A.P., P.S., P.P. and R.D carried out experiments. S.E., E.T.H., M.P., E.Y. and A.P. helped perform ChIP, ATAC and RNA-seq and data analyses. M.C. performed the perfusion on animals. D.H. and F.Y. performed IHC experiments. D.D. performed blinded quantification of generation of IHC images and helped edit the final version of the manuscript. T.V. and R.M.M. generated *Acod1*$^{-/-}$ and *Acod1*$^{fl/fl}$ mice. J.H.S., J.L., M.N., M.P., S.R.S. and A.P. contributed to data analyses. M.S., A.R.J. and Y.W. provided human tumour tissues. T.O., E.C.H., A.G., N.K.F., K.A.M., M.T., S.A. and R.J.G. provided primary patient cell lines. A.F., M.T., R.J.G., C.K., A.M.C., C.A.L. and D.N. helped interpret data and provided feedback on the manuscript. S.V. provided funding, resources, conceptual input and supervised the research. All authors reviewed and approved the final version of the manuscript.

Competing interests S.K.N., J.L. and S.V. are listed as inventors on US provisional patent 63/919,979. A.M.C. is a co-founder and serves on the Scientific Advisory Board of Lynx Dx, Esanik Therapeutics, Medsyn and Flamingo Therapeutics. A.M.C. is a scientific consultant for EdenRoc, Proteovant, Aurigene Oncology, RAPPTA, Belharra and Tempus. C.A.L. has received consulting fees from Astellas Pharmaceuticals, Odyssey Therapeutics and T-Knife Therapeutics, and is an inventor on patents pertaining to KRAS-regulated metabolic pathways, redox control pathways in pancreatic cancer, and targeting the GOT1 pathway as a therapeutic approach (US patent 2015126580-A1, 05/07/2015; US patent 20190136238, 05/09/2019; international patent WO2013177426-A2, 04/23/2015).

Additional information
Supplementary information The online version contains supplementary material available at https://doi.org/10.1038/s41586-025-10005-1.
Correspondence and requests for materials should be addressed to Sriram Venneti.
Peer review information *Nature* thanks the anonymous reviewers for their contribution to the peer review of this work.
Reprints and permissions information is available at http://www.nature.com/reprints.

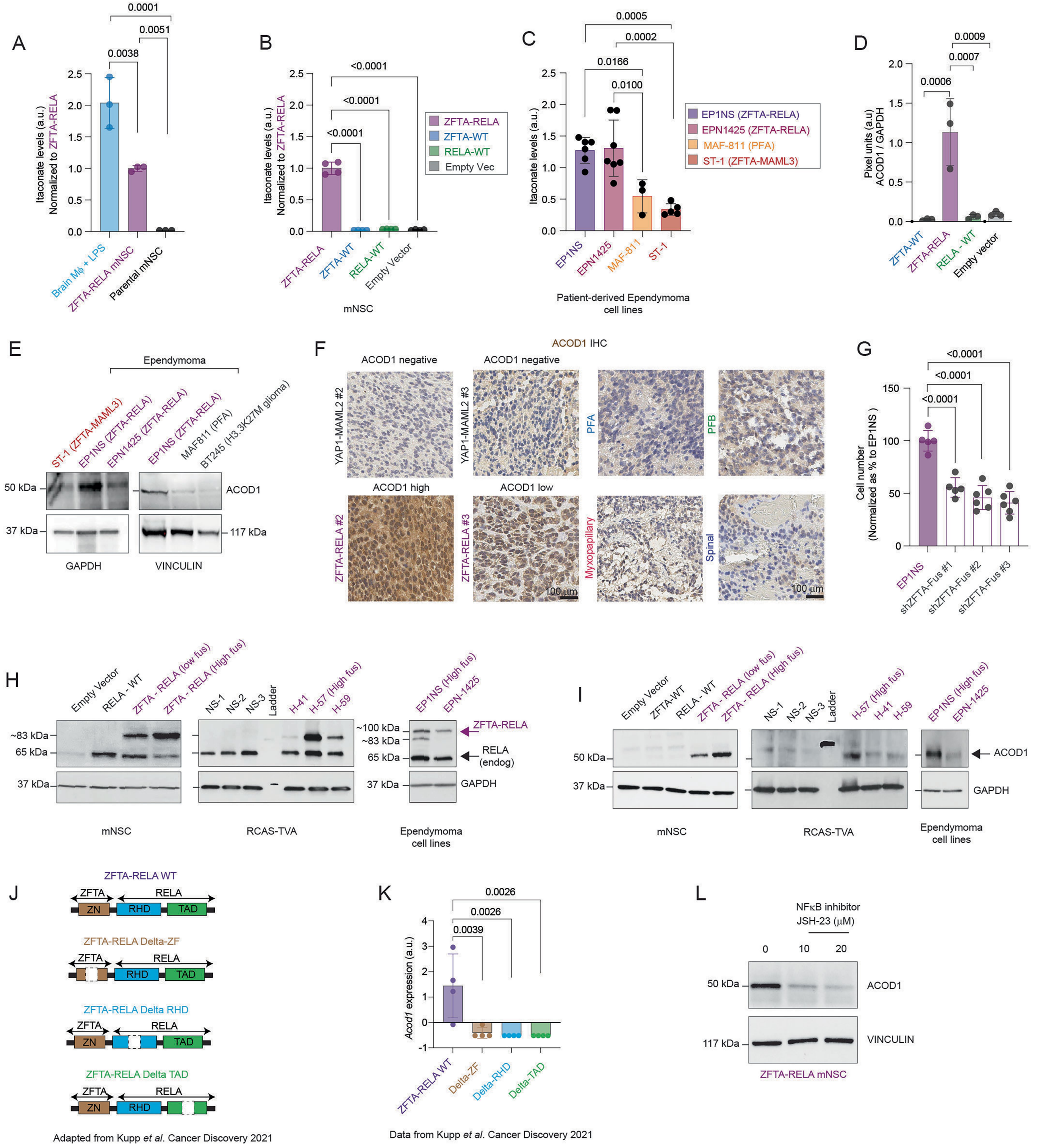

Extended Data Fig. 1 | See next page for caption.

Extended Data Fig. 1 | ZFTA-RELA induces ACOD1 expression and itaconate production. A) Itaconate levels (y-axis, per 10^6 cells mean normalized to internal standard) in BV2 brain macrophages (Mϕ) treated with 1ng/mL Lipopolysaccharide (LPS) for 6 h (light blue, n=3 independent samples), ZFTA-RELA (purple, n=3 independent samples), and parental (gray, n=3 independent samples) mNSCs. Data shown as mean ± SD and analyzed using one-way ANOVA with Tukey's multiple comparisons test using 95% C.I. **B-C**) Bar plot showing itaconate levels (y-axis, per 10^6 cells mean normalized to internal standard, a.u.) in (**B**) ZFTA-RELA (purple), ZFTA-WT (blue), RELA-WT (green), and ev (gray) mNSCs. (**C**) Itaconate levels (y-axis, per 10^7 cells mean normalized to internal standard) in EP1NS (violet, ZFTA-RELA fusion, n=6 independent samples), EPN1425 (purple, ZFTA-RELA fusion, n=7 independent samples), MAF-811 (orange, Posterior Fossa Type A, n=3 independent samples), and ST-1 (red, ZFTA-MAML3, n=5 independent samples) mNSCs. Data shown as mean ± SD and analyzed by using one-way ANOVA with Tukey's multiple comparisons test with 95% C.I. Z-scores calculated from this data are shown in Fig. 1c. **D**) Bar plot showing densitometric quantification of ACOD1 protein level (y-axis: pixel units a.u normalized to GAPDH) in ZFTA-WT, ZFTA-RELA, RELA-WT and ev-mNSCs. Quantification was performed using Image J software from n=3 independent experiments. Data shown as mean ± SD and analyzed using one-way ANOVA with Dunnett's multiple comparisons using 95% C.I. **E**) Immunoblot for ACOD1 protein levels relative to GAPDH and VINCULIN shown in ST-1 (red, ZFTA-MAML3), EP1NS (purple, ZFTA-RELA fusion), EPN1425 (purple, ZFTA-RELA fusion), MAF-811 (gray, PFA ependymoma) and BT-245 (gray, H3.3K27M) patient-derived cell lines. **F**) Representative IHC images from ACOD1 negative YAP1-MAML2 (gray text) and high ACOD1 (bottom left), and low ACOD1 ZFTA-RELA (purple text), Posterior Fossa type A (PFA, light blue text), Posterior Fossa type B (green text), Myxopapillary (pink text), and Spinal (dark blue text) patient ependymomas. Quantification of images shown in Fig. 1f. **G**) Cell number (y-axis, normalized as percentage to total live EP1NS cells without ZFTA-fusion knockdown) in parental EP1NS cells (purple bar) or EP1NS cells with ZFTA-RELA fusion knockdown (clear bars, 3 independent shRNAs). Data from n=5 (EP1NS, shZFTA-Fus #1) and n=6 (shZFTA-Fus #2, shZFTA-Fus #3) independent samples shown as mean ± SD and analyzed using one-way ANOVA with Dunnett's multiple comparisons using 95% C.I. **H-I**) Western blots for RELA (**H**) and ACOD1 (**I**, black arrow, -50 kDa) in relation to GAPDH in a panel of ZFTA-RELA fusion (purple text) and non-fusion (black text) cell lines. RELA blots demonstrate expression of ZFTA-RELA fusion (purple arrow, ~83 kDa) and endogenous RELA (black arrow, 65 kDa). Cell lines used: - mNSC non-fusion ev, and RELA-WT, ZFTA-WT - mNSC ZFTA-RELA. Lentiviral induction of ZFTA-RELA fusion was titrated to achieve low and high levels of fusion expression). - NS-1, NS-2, and NS-3 RCAS-TVA murine isogenic non-fusion ependymoma tumor cell lines from Ozawa T, et al., Cell Reports, 2018[12]. - H-57 (high fusion), H-41, and H-59 RCAS-TVA murine ZFTA-RELA ependymoma tumor cell lines from Ozawa T, et al., Cell Reports, 2018[12]. - EP1NS (high fusion), and EPN1425 patient-derived ependymoma cell lines. **J**) Schematic illustrating ZFTA-RELA fusion constructs with deletions in zinc (ZN) finger (Delta-ZF), Rel homology domain (Delta-RHD) or Transactivating domain (Delta-TAD) adapted from Kupp et al.[10] **K**) *Acod1* mRNA levels (n=4 independent samples, z-scores, y-axis) in cells expressing the indicated ZFTA-RELA fusion deletion constructs from Fig. S1k. Data are derived from Kupp et al.[10], and shown as mean ± SD. Data were analyzed by one-way ANOVA with Dunnett's multiple comparisons using 95% C.I. **L**) Immunoblot for ACOD1 protein levels in relation to VINCULIN shown in ZFTA-RELA mNSCs after treatment with the NF-kB inhibitor, JSH-23 at the indicated concentrations for 48h.

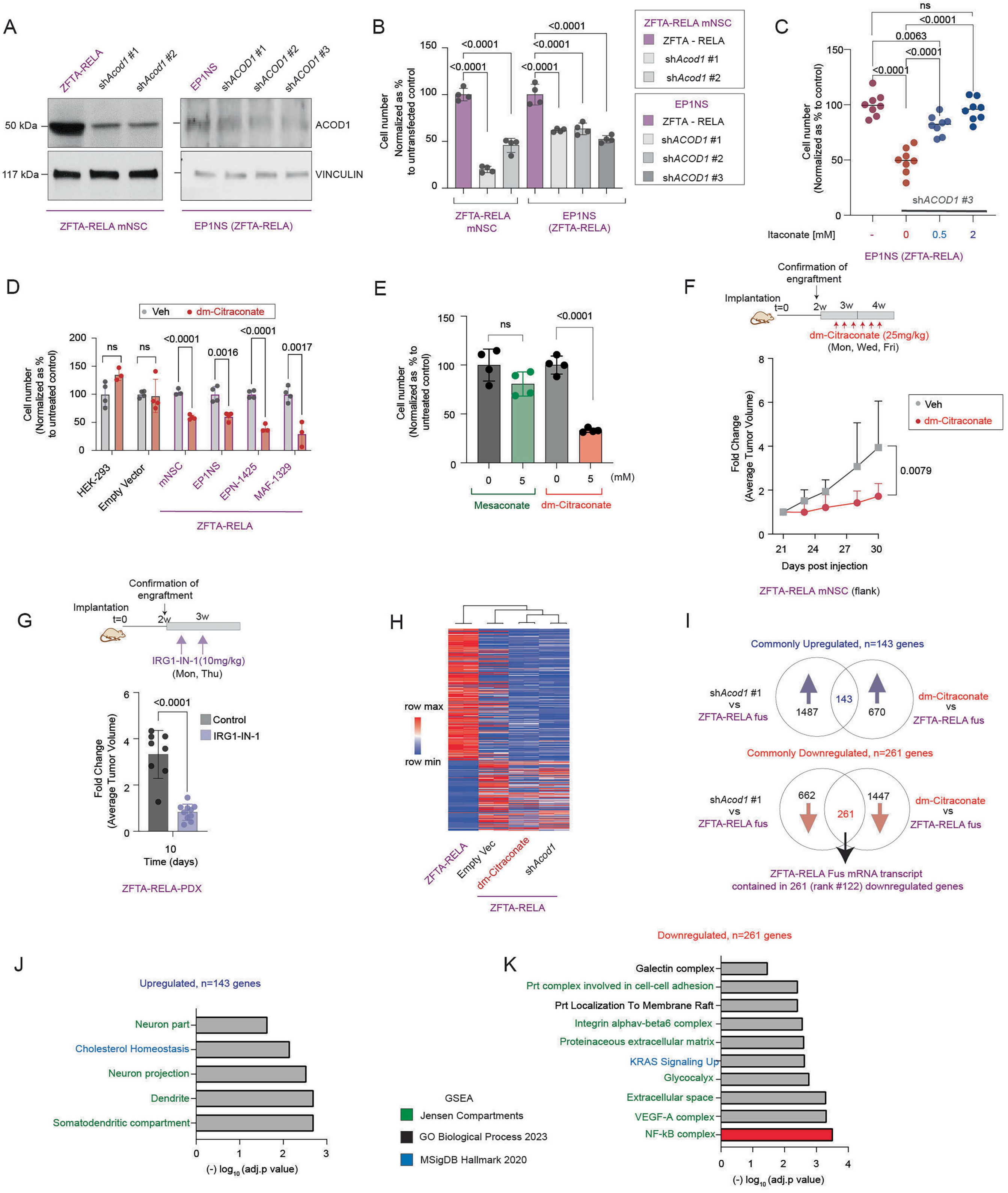

Extended Data Fig. 2 | See next page for caption.

Extended Data Fig. 2 | Suppressing ACOD1 or antagonizing itaconate metabolism with dm-citraconate reduces ZFTA-RELA mRNA levels and is toxic to ZFTA-RELA tumor cells. A) Western blots showing ACOD1 levels to in ZFTA-RELA mNSCs (left, relative to GAPDH, n=2 independent shRNAs) and EP1NS (right, relative to VINCULIN, n=3 independent shRNAs) with/without *ACOD1* knockdown. **B**) Bar graph showing cell number (y-axis, normalized as percentage to ZFTA-RELA fusion cells without *ACOD1* knockdown) in ZFTA-RELA mNSCs (n=2 independent shRNAs) and EP1NS cells (n=3 independent shRNAs) with or without ACOD1 knockdown (n=4 independent samples, each). Cells were counted 48h after plating. Data shown as mean ± SD and analyzed by two-way ANOVA with Tukey's multiple comparisons using 95% confidence intervals (C.I). **C**) Cell number (y-axis, normalized as percentage to EP1NS cells without *ACOD1* knockdown) in EP1NS cells without *ACOD1* knockdown (purple); or with *ACOD1* knockdown (red); or with *ACOD1* knockdown supplemented with itaconate - 0.5mM (light blue), or 2mM (dark blue) for 48h (n=8 independent samples, each). EP1NS cells with the best *ACOD1* knockdown (sh*ACOD1* #3 as per Extended Data Fig. 2a) was used for this experiment. Data shown as mean ± SD and analyzed by one-way ANOVA with Tukey's multiple comparisons using 95% C.I. **D**) Cell number (y-axis, normalized as percentage to corresponding vehicle treated controls) in ZFTA-RELA fusion (purple bars) and control non-fusion (gray bars) cell lines treated with vehicle (gray) or dm-citraconate (red, 10mM) for 24h (n=3-4 independent samples each). Data shown as mean ± SD and analyzed by unpaired, two-tailed, two-sided t-test with 95% C.I. **E**) Cell number (y-axis, normalized as percentage to corresponding vehicle treated controls) in ZFTA-RELA mNSCs treated with vehicle (gray), or mesaconate (itaconate analogue that does not inhibit ACOD1[61], green, 5mM), or dm-citraconate (red, 5mM) for 24h (n=4 independent samples, each). Data shown as mean ± SD and analyzed by unpaired, two-tailed, two-sided t-test with 95% C.I. **F**) Fold change in the average tumor volume (y-axis) plotted against time (days post injection, x-axis) of ZFTA-RELA mNSCs xenografted in the flanks of mice and treated with vehicle (gray, n=9), or dm-citraconate (red, n=10, 25mg/kg, i.v.). Data shown as mean ± SD and analyzed by unpaired, two-tailed, two-sided t-test with 95% C.I. using 95% C.I. Schematic illustration of the dm-citraconate (25mg/kg, i.v.) treatment regimen shown above the graph **G**) Bar plot showing the fold change in the average tumor volume (y-axis) at day 10 (days post tumor engraftment, x-axis) of MAF-1329 (ZFTA-RELA) PDX xenografted in the flanks of mice and treated with vehicle (gray, n=8), or IRG1-IN-1 (ACOD1-specific inhibitor, 10 mg/kg, i.p.) (violet, n=9). Data shown as mean ± SD and analyzed by unpaired, two-tailed, two-sided t-test with 95% C.I. Schematic illustration of the IRG1-IN-1 (10mg/kg, i.v.) treatment regimen shown above the graph **H**) Heatmap representing the top differentially upregulated and downregulated genes in ZFTA-RELA mNSCs (purple text) compared to ev-mNSCs (gray text), or ZFTA-RELA mNSCs treated with dm-citraconate (10mM for 24h, red text), or ZFTA-RELA mNSCs with *Acod1* knockdown (sh*Acod1* #1) (2 independent samples R1, R2, each). **I**) Venn diagrams illustrating commonly upregulated (143) and downregulated (261) genes in ZFTA-RELA mNSCs after treatment with dm-citraconate or after *Acod1* knockdown from Extended Data Fig. 2h. Significantly different genes (adjusted p value of <0.05) were identified by DEseq2 analysis. The position of ZFTA-RELA mRNA (#122) among the 261 commonly downregulated genes is indicated with the black arrow. **J-K**) The top 10 differentially **J**) upregulated pathways (from143 commonly upregulated genes from Extended Data Fig. 2i) and (**K**) top 15 differentially downregulated pathways (from 261 commonly downregulated genes from Extended Data Fig. 2i). Red indicates NF-kB complex as the top downregulated pathway in ZFTA-RELA mNSCs treated with dm-citraconate and *Acod1* knockdown. Differentially enriched pathways were identified using EnrichR (https://maayanlab.cloud/Enrichr/). Text: black=GO Biological Process 2023, green=Jensen Compartments, and blue=MSigDB Hallmark 2020.

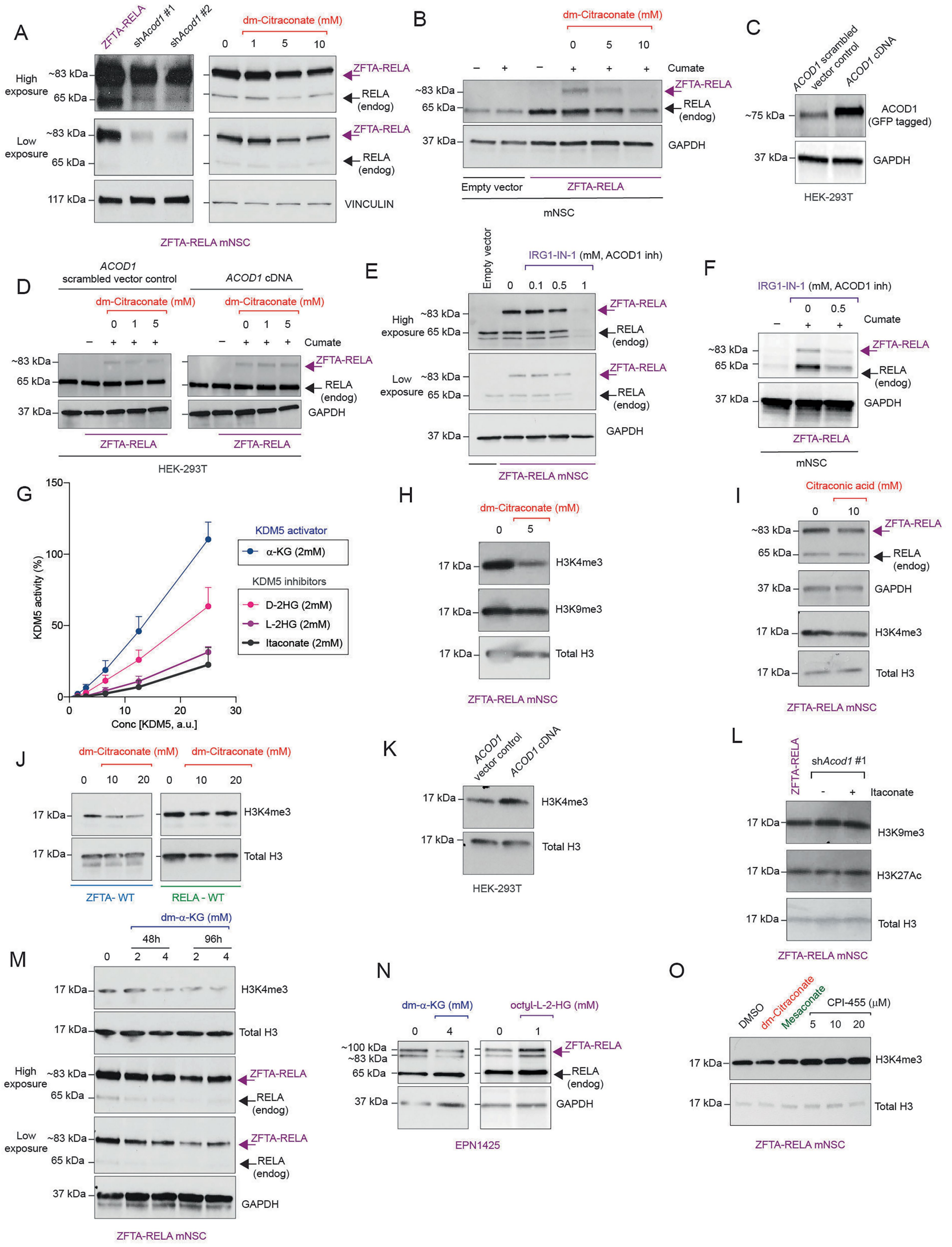

Extended Data Fig. 3 | See next page for caption.

Extended Data Fig. 3 | Inhibiting ACOD1 lowers global H3K4me3 and decreases pathogenic ZFTA-RELA fusion levels. A) Western blots probed for RELA (relative to VINCULIN) depicting changes in protein levels of ZFTA-RELA fusion (purple arrow, ~83 kDa) and endogenous RELA (black arrow, 65 kDa) in ZFTA-RELA mNSCs with/without *Acod1* knockdown; or vehicle versus dm-citraconate treatment (red) at the indicated concentrations for 24h (right). (High exposure: top, low exposure: bottom). **B**) Western blots for RELA (relative to GAPDH) in mNSCs with cumate-inducible expression of ev (lanes 1-2) or ZFTA-RELA fusion (lanes 3-6). Arrows point to changes in ZFTA-RELA fusion levels (purple arrow, ~83 kDa) and endogenous RELA (black arrow, 65 kDa). No cumate (lanes 1 and 3); cumate-induction (48h) with vehicle treatment (lanes 2 and 4), and cumate-induction with dm-citraconate treatment (red, lanes 5 and 6) at the indicated concentrations for 48h. **C**) Immunoblot for ACOD1(relative to GAPDH) in HEK293 cells expressing either a non-targeted, vector control for *ACOD1* (left) or with an *ACOD1* overexpression (right) cDNA (GFP tagged, ~75 kDa). **D**) HEK293 cells expressing a non-targeted, vector control for *ACOD1* (left) or an *ACOD1* overexpression (right) cDNA were transfected with cumate-inducible ZFTA-RELA fusion constructs. Western blots for RELA (left and right panels, relative to GAPDH) depict changes in ZFTA-RELA fusion levels (purple arrow, ~83 kDa) and endogenous RELA (black arrow, 65 kDa). No cumate (lanes 1 and 2); or cumate-induction (48h) with vehicle treatment (lane 3), or cumate-induction with dm-citraconate treatment (red) at the indicated concentrations (lanes 4 and 5) for 48h. **E**) Western blots for RELA (relative to GAPDH) depicting changes in protein levels of ZFTA-RELA fusion (purple arrow, ~83 kDa) and endogenous RELA (black arrow, 65 kDa) in ZFTA-RELA mNSCs after treatment with the ACOD1 inhibitor, IRG1-IN-1 at the indicated concentrations for 48h (high exposure: top, low exposure: bottom). **F**) Western blots for RELA (relative to GAPDH) in ZFTA-RELA mNSCs with cumate-inducible ZFTA-RELA depicting changes in ZFTA-RELA fusion levels (purple arrow, ~83 kDa) and endogenous RELA (black arrow, 65 kDa). No cumate (lane 1); or cumate-induction with vehicle treatment (lane 2); or cumate-induction with IRG1-IN-1 treatment (lane 3) at the indicated concentration for 48h. **G**) KDM5 activation dose response curves (y-axis, mean ± SD shown as a percentage of KDM5 activity; x-axis, increasing concentrations of the KDM5 [enzyme units] as indicated) upon incubation with Itaconate (2mM, black), or D-2-hydroxyglutarate (D-2HG, 2mM, pink), or L-2-hydroxyglutarate (L-2HG, 2mM, violet), or α-ketoglutarate (α-KG, 2mM, blue). (n=6-9 samples, each) **H**) Western blots for H3K4me3 and H3K9me3 relative to total H3 in ZFTA-RELA mNSCs after treatment with dm-citraconate (5mM) for 48h. **I**) Western blots probed for RELA (relative to VINCULIN) depicting changes in protein levels of ZFTA-RELA fusion (purple arrow, ~83 kDa) and endogenous RELA (black arrow, 65 kDa) and H3K4me3 (relative to total H3) in ZFTA-RELA mNSCs treated with vehicle or Citraconic acid (red) at the indicated concentrations for 48h. **J**) Western blots for H3K4me3 and total H3 in ZFTA-WT (left) and RELA-WT mNSCs (right) after treatment with dm-citraconate at the indicated concentrations for 48h. **K**) Western blots in HEK293 cells with either a non-targeted, vector control for *ACOD1* (left) or with an *ACOD1* overexpression (right) cDNA (GFP tagged, ~75 kDa) from Extended Data Fig. 3c showing levels of H3K4me3 (relative to total H3). **L**) ZFTA-RELA mNSCs (lane 1); or ZFTA-RELA mNSCs with *Acod1* knockdown (lane 2); or ZFTA-RELA mNSCs with *Acod1* knockdown supplemented with 1mM itaconate for 48h (lane 3) were probed for H3K9me3 and H3K27Ac relative to total H3. **M**) ZFTA-RELA mNSCs were treated with cell permeable, dimethyl α-KG (dm-α-KG) at the indicated concentrations for 48 and 96 h. Western blots show changes in H3K4me3 levels (relative to total H3). Western blots for RELA (in relation to GAPDH) show ZFTA-RELA fusion (purple arrow, ~83 kDa), and endogenous RELA (black arrow, 65 kDa) (high exposure: top, low exposure: bottom). **N**) Western blots for RELA (in relation to GAPDH) in patient-derived ZFTA-RELA EPN1425 cells showing changes in protein levels of ZFTA-RELA fusion (purple arrow, higher molecular weights), and endogenous RELA (black arrow, 65 kDa) upon treatment with cell permeable α-KG (dm-α-KG, left) or L-2HG (octyl-L-2HG, right) at the indicated concentrations for 96 h. **O**) Western blots for H3K4me3 (in relation to total H3) in ZFTA-RELA mNSCs treated with DMSO (lane 1), dm-citraconate (10mM, red, lane 2), mesaconate (10mM, green, does not inhibit ACOD1 and used as control, lane 3) for 48h; and the H3K4me3 demethylase KDM5 inhibitor CPI-455 (lanes 4,5 and 6) at indicated concentrations for 48h.

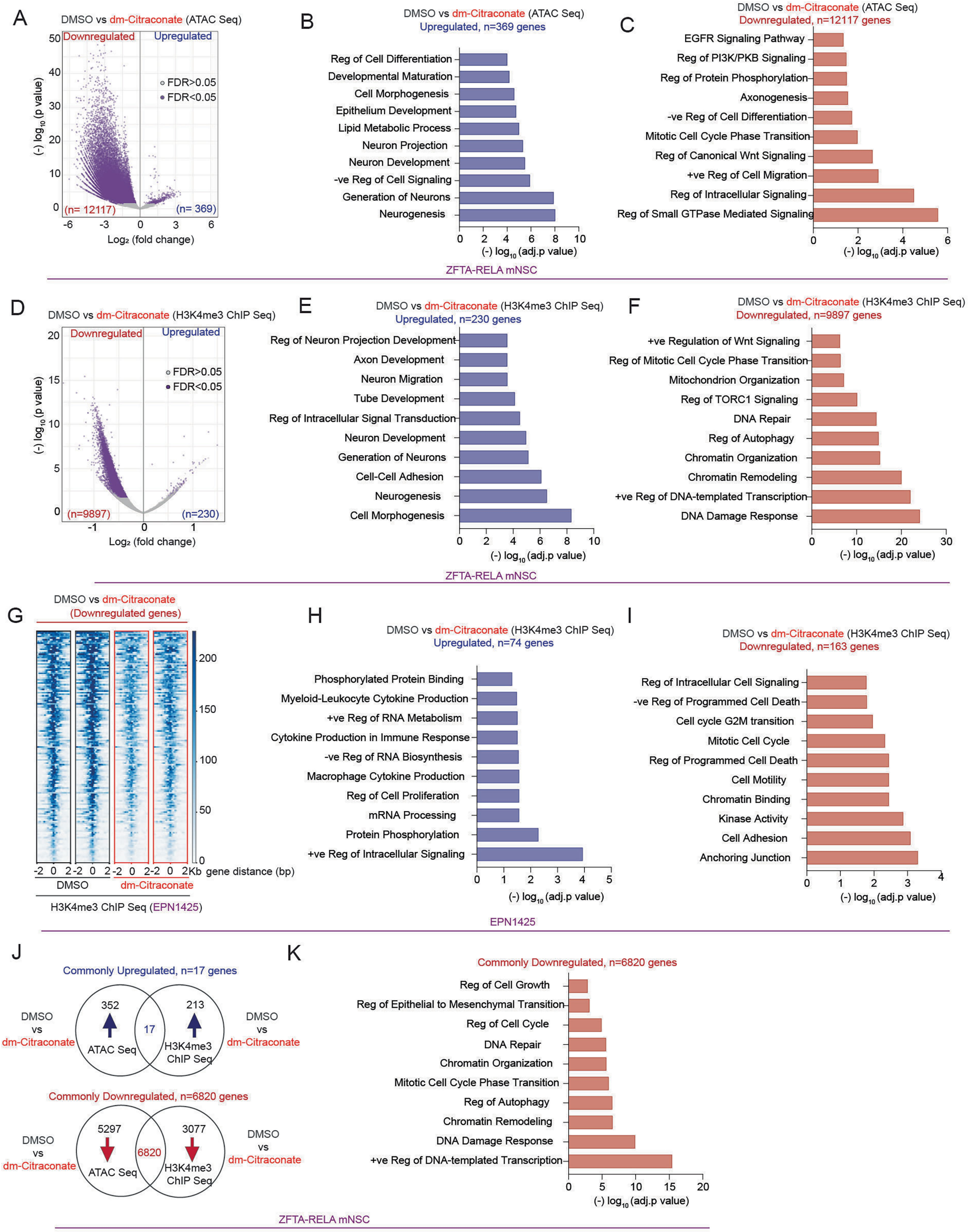

Extended Data Fig. 4 | See next page for caption.

Extended Data Fig. 4 | DM-citraconate treatment represses chromatin accessibility and decreases H3K4me3 enrichment in ZFTA-RELA cells. **A**) Volcano plot from ATAC seq (x-axis, $\log_2$-fold change) depicting genes (Table S8) that significantly (y-axis, $\log_{10}$ p value, $p<0.05$) gained (upregulated) or lost (downregulated) chromatin accessibility in ZFTA-RELA mNSCs upon dm-citraconate treatment (10mM) versus DMSO for 48h. **B-C**) The differentially **B**) upregulated pathways from (n=369) genes that showed a gain in chromatin accessibility from Extended Data Fig. 4a, Table S9) and (**C**) downregulated pathways from (n=12117) genes that showed a loss in chromatin accessibility from Extended Data Fig. 4a, Table S10) in ZFTA-RELA cells treated with dm-citraconate vs DMSO. Differentially enriched Gene Ontology (GO) biological pathways were identified using EnrichR (https://maayanlab.cloud/Enrichr/) and Gene Set Enrichment Analysis (GSEA). **D**) Volcano plot from H3K4me3 ChIP seq (x-axis, $\log_2$-fold change) depicting genes (Table S11) that significantly (y-axis, $\log_{10}$ p value, $p<0.05$) gained (upregulated) or lost (downregulated) H3K4me3 enrichment in ZFTA-RELA mNSCs upon dm-citraconate treatment (10mM) versus DMSO for 48h. **E-F**) The differentially (**E**) upregulated pathways from (n=230) genes that showed a gain in H3K4me3 enrichment from Extended Data Fig. 4d, Table S12) and (**F**) downregulated pathways from (n=9897) genes that showed a loss in H3K4me3 enrichment from Extended Data Fig. 4d, Table S13) in ZFTA-RELA cells treated with dm-citraconate vs DMSO. Differentially enriched Gene Ontology (GO) biological pathways were identified using EnrichR (https://maayanlab.cloud/Enrichr/) and Gene Set Enrichment Analysis (GSEA). **G**) Heatmaps for H3K4me3 ChIP seq in EPN1425 cells treated with DMSO (gray) or dm-citraconate (10mM, red) for 48h showing decreased H3K4me3 enrichment. **H-I**) The differentially (**H**) upregulated pathways from (n=74) genes that showed a gain in H3K4me3 enrichment from Extended Data Fig. 4g, Table S12) and (**I**) downregulated pathways from (n=163) genes that showed a loss in H3K4me3 enrichment from Extended Data Fig. 4g, Table S13) in EPN1425 cells treated with dm-citraconate vs DMSO. Differentially enriched Gene Ontology (GO) biological pathways were identified using EnrichR (https://maayanlab.cloud/Enrichr/) and Gene Set Enrichment Analysis (GSEA). **J**) Venn diagrams depicting the overlapping genes from H3K4me3 (from ChIP-seq) and chromatin accessibility (from ATAC-seq) in ZFTA-RELA mNSCs treated with dm-citraconate (10mM) for 48 h. Top panel shows genes (n=17, blue) with overlapping increase in H3K4me3 enrichment and chromatin accessibility. Bottom panel shows genes (n=6820, red) with overlapping decrease in H3K4me3 enrichment and chromatin accessibility. **K**) The differentially downregulated pathways from (n=6820) genes that showed an overlapping decrease in H3K4me3 enrichment and chromatin accessibility in ZFTA-RELA mNSCs upon dm-citraconate treatment (from Extended Data Fig. 4j). Differentially enriched Gene Ontology (GO) biological pathways were identified using EnrichR (https://maayanlab.cloud/Enrichr/).

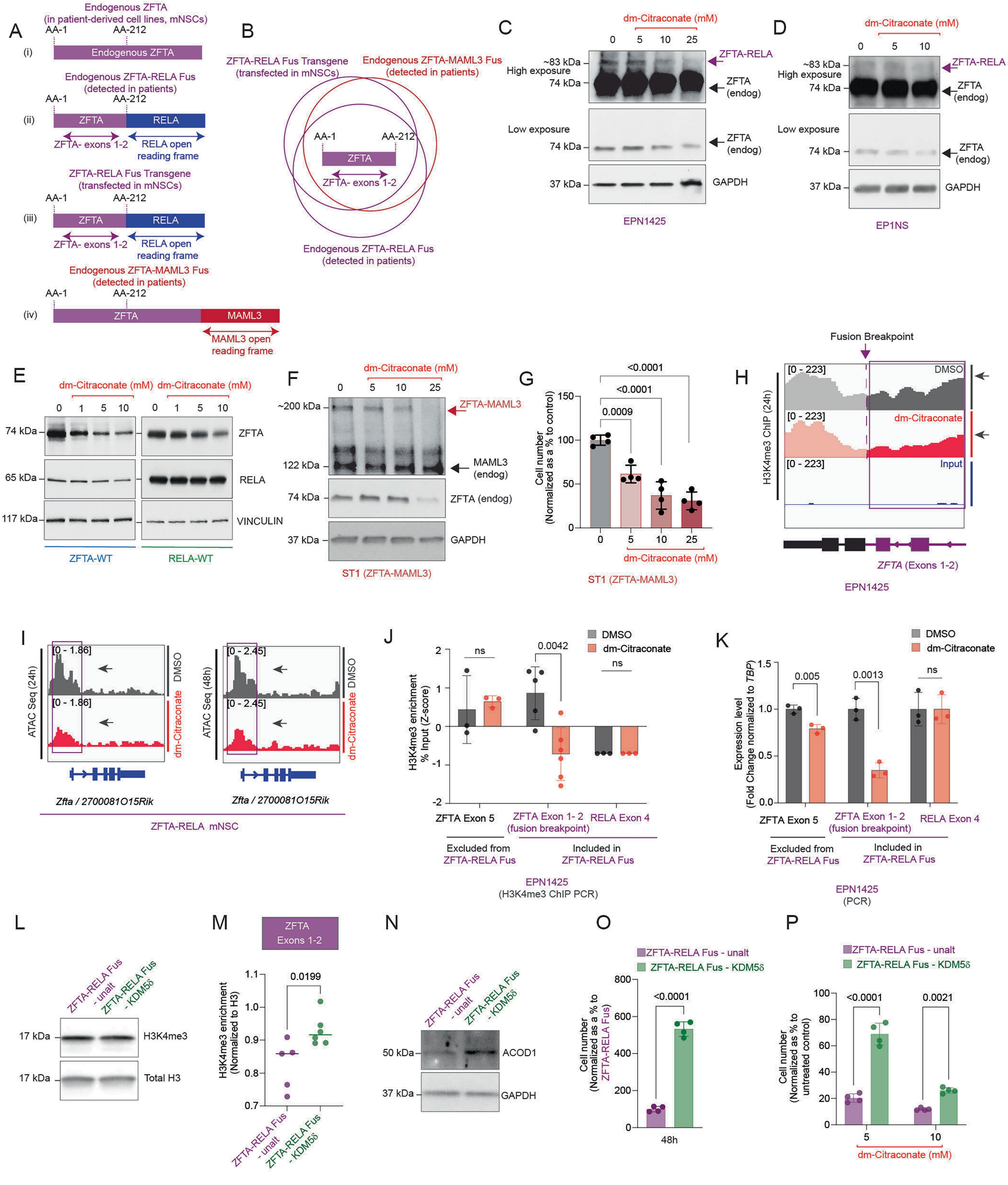

Extended Data Fig. 5 | See next page for caption.

Extended Data Fig. 5 | dm-citraconate lowers genomic H3K4me3 at the ZFTA regulatory region of ZFTA-RELA. A-B) Schematic illustrating the (**A**) similarities between endogenous ZFTA, endogenous ZFTA-RELA fusion (as detected in patients and patient-derived cell lines), ZFTA-RELA transgene (expressed in mNSCs), and endogenous ZFTA-MAML3 fusion (detected in patients and in ST-1 cells). (**B**) Venn Diagram showing the common ZFTA-regulatory regions (Exons 1 and 2 of ZFTA) contained within the ZFTA-RELA transgene and endogenous ZFTA-RELA and ZFTA-MAML3 fusion genes. **C-D**) Western blots for ZFTA (relative to GAPDH) depicting changes in protein levels of ZFTA-RELA fusion (purple arrow, higher molecular weight) and endogenous ZFTA (black arrow, lower molecular weight) in (**C**) EPN1425 and (**D**) EP1NS patient-derived cell lines after treatment with dm-citraconate at the indicated concentrations for 24h (high exposure: top, low exposure: middle). **E**) Western blots for endogenous ZFTA and RELA (relative to VINCULIN) in ZFTA-WT mNSC (left), RELA-WT (middle) expressing mNSCs after treatment with dm-citraconate at indicated concentrations for 24h. **F**) Western blots for MAML3 depicting changes in protein levels of ZFTA-MAML3 fusion (red arrow, higher molecular weight), endogenous MAML3 (black arrow, lower molecular weight, top panel) in relation to GAPDH (bottom panel) in the patient-derived ST-1 (ZFTA-MAML3 fusion) cell line after treatment with dm-citraconate at indicated concentrations for 24h. The same lysates were probed for endogenous ZFTA (middle panel). **G**) Cell number (y-axis) of ST-1 ZFTA-MAML3 fusion patient-derived ependymoma cells after treatment with dm-citraconate at the indicated concentrations for 24h (mean ± SD, n=4 independent samples, each). Statistical analysis was performed by one-way ANOVA with Dunnett's multiple comparisons using 95% C.I. **H**) Representative ChIP tracks for H3K4me3 at *ZFTA* locus in EPN1425 (patient-derived ZFTA-RELA ependymoma) cells treated with DMSO (gray) or 10mM dm-citraconate (red) for 24h. Dotted purple line indicates the fusion breakpoint region in ependymoma patients (between exons 1 and 2 of *ZFTA* containing amino acids 1-212). Arrows indicate H3K4me3 peaks at *ZFTA* (Exons1-2) loci. **I**) Representative ATAC seq tracks depicting chromatin accessibility changes at the *Zfta* (*2700081O15Rik*) locus (indicated by purple box) in ZFTA-RELA mNSCs treated with DMSO (gray) or 10mM dm-citraconate (red) for 24h (n=2 independent samples, left panel) and 48h (n=2 independent samples, right panel). Arrows indicate ATAC seq peaks at *Zfta* locus. **J**) H3K4me3-ChIP qPCR was performed in patient-derived ZFTA-RELA fusion EPN1425 cells treated with DMSO (gray) or dm-citraconate (10mM, red) for 48h. Bar graphs show H3K4me3 enrichment (y-axis, data normalized to IgG controls and shown as z-scores of % input values) at *ZFTA* Exons 1-2 fusion breakpoint regulatory region in ependymoma patients that is part of the ZFTA-RELA fusion. As controls, *ZFTA* exon 5 (not included in ZFTA-RELA fusions), and *RELA* Exon 4 (promoters not part of ZFTA-RELA fusions) were used. Data shown as mean ± SD from 3-5 independent samples analyzed using two-way ANOVA with adjusted p values shown after multiple comparisons using 95% C.I. Fold Change calculated from this data is shown in Fig. 3f. **K**) Patient-derived ZFTA-RELA fusion EPN1425 cells were treated with DMSO (gray) or dm-citraconate (10mM, red) for 48h, following which qPCR was performed. Bar graph showing changes in mRNA expression levels (y-axis, data normalized to expression levels of housekeeping gene TATA binding protein, *TBP*) of *ZFTA* Exons 1-2 fusion breakpoint regulatory region (primers were designed to these specific regions as in Fig. 3f). As controls, qPCR for *ZFTA* exon 5 (not included in ZFTA-RELA fusions), and *RELA* Exon 4 (promoters not part of ZFTA-RELA fusions) were used. Data shown as mean ± SD from n=3 independent samples and analyzed by using two-way ANOVA with adjusted p values shown after multiple comparisons using 95% C.I. Fold Change calculated from this data is shown in depicted in Fig. 3f. **L**) Western blots for global H3K4me3 (relative to total H3) in ZFTA-RELA Fus - unaltered (purple) and ZFTA-RELA – KDM5δ (green) mNSCs. **M**) Scatter plot showing H3K4me3 enrichment (y-axis, data is normalized to % input values of Histone H3 for each cell line) at *ZFTA* Exons 1-2 (fusion breakpoint region in ependymoma patients and is part of the ZFTA-RELA fusion) in ZFTA-RELA Fus - unaltered (purple) and ZFTA-RELA – KDM5δ (green) mNSC. Data are shown as mean ± SD from n=5-6 independent samples, and were analyzed by unpaired, two-tailed, two-sided t-test with 95% C.I. **N**) Western blots for ACOD1 (relative to GAPDH) in ZFTA-RELA Fus - unaltered (purple) and ZFTA-RELA – KDM5δ (green) mNSC. **O**) Bar plots depicting cell numbers (y-axis, normalized as percentage of total live ZFTA-RELA Fus cells) of ZFTA-RELA Fus - unaltered (purple) and ZFTA-RELA – KDM5δ (green) cells at 48 h after seeding. Data shown as mean ± SD of n=4 independent samples and analyzed by unpaired, two-tailed, two-sided t-test with 95% C.I. **P**) Bar plots depicting cell number (y-axis, normalized as percentage to DMSO-treated control cells) of ZFTA-RELA Fus - unaltered (purple) and ZFTA-RELA – KDM5δ (green) cells treated with dm-citraconate at the indicated concentrations for 48h. Data shown as mean ± SD from n=4 independent samples and analyzed by using two-way ANOVA with Šídák's multiple comparisons using 95% C.I.

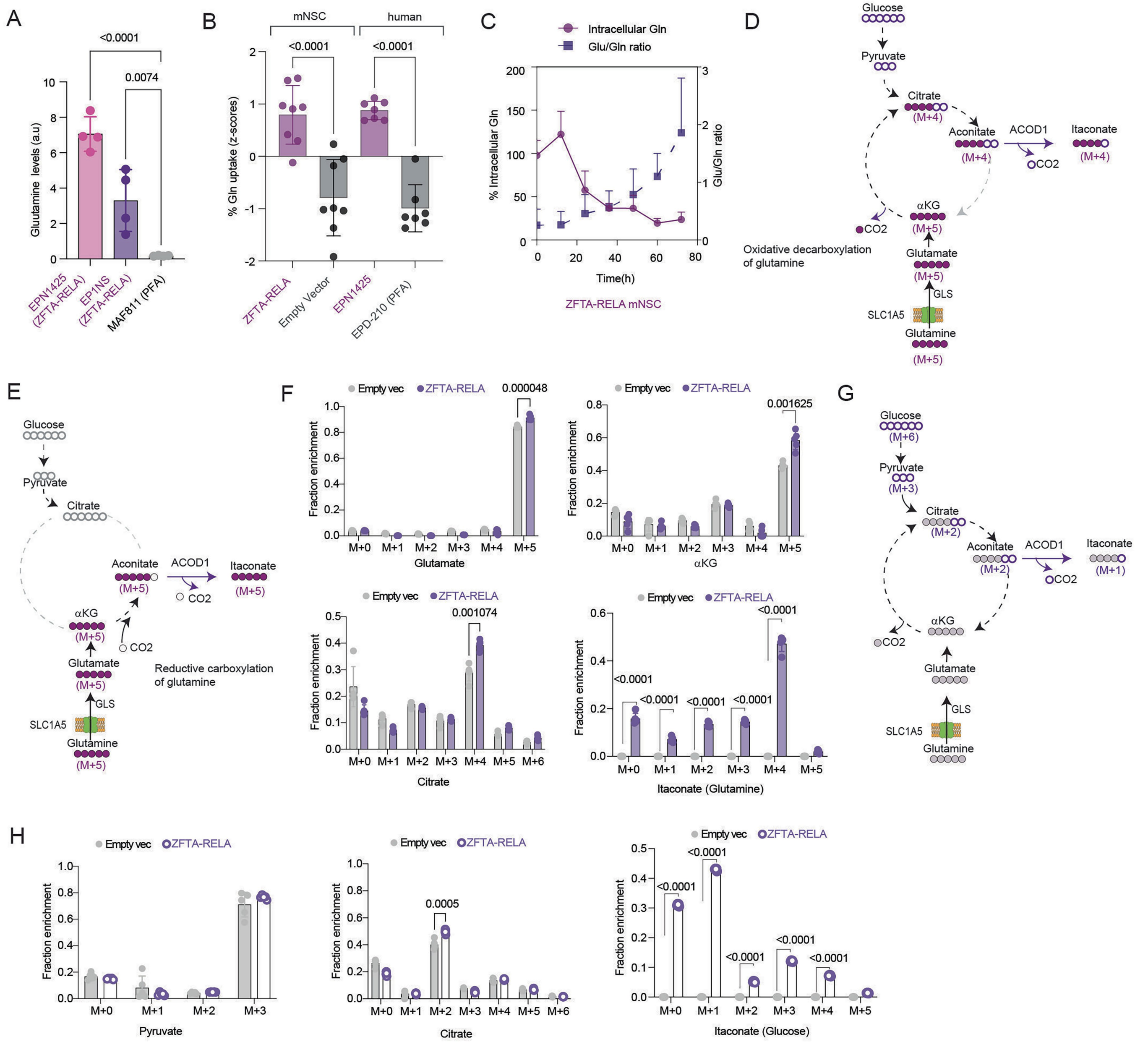

Extended Data Fig. 6 | ZFTA-RELA upregulates glutamine metabolism to generate itaconate. A) Bar plot showing glutamine levels (y-axis, per 10^6 cells mean normalized to internal standard, a.u.) in ZFTA-RELA fusion EP1NS and EPN1425 and control MAF811 (non-fusion PFA) ependymoma patient-derived cell lines. Data shown as mean ± SD of n=4 independent samples and analyzed using one-way ANOVA with Šídák's multiple comparisons using 95% C.I. **B**) Bar graph showing glutamine uptake (y-axis, z-scores of % glutamine consumed per 10^6 cells from culture media after 72 h) in mouse ZFTA-RELA mNSC (purple) and human ZFTA-RELA fusion EPN1425 cells (purple) cells vs control cells (ev-mNSC, and EPD-210 patient-derived, non-fusion PFA ependymomas, gray). Data shown as mean ± SD of n=7-8 samples each from 2 independent experiments and analyzed using one-way ANOVA with multiple comparisons test using 95% C.I. **C**) X-Y graph showing glutamine consumption (left y-axis, % intracellular glutamine per 10^6 cells consumed from culture media at each time point) in ZFTA-RELA mNSCs as a function of time (x-axis, 0–72 h). Glutamine utilization to produce glutamate is also indicated (right y-axis, intracellular Glutamate (Glu) / intracellular Glutamine (Gln) ratios measured per 10^6 cells. Data shown as mean ± SD of n=8 samples each from 2 independent experiments. **D-E**) Schematic illustrating the possible pathways of itaconate biosynthesis from glutamine. Radiolabeled glutamine (M+5) is imported into cells by the transporter SLC1A5 and converted to glutamate (M+5) by the enzyme, glutaminase (GLS). Glutamate is converted into alpha-ketoglutarate (M+5 α-KG) which is then incorporated into the citric acid cycle to: **D**) synthesize citrate (M+4) and aconitate (M+4) that can subsequently give rise to itaconate (M+4) through oxidative decarboxylation (forward direction). **E**) Alternately, alpha-ketoglutarate (M+5 α-KG) can be converted to aconitate (M+5) by reductive carboxylation to give rise to itaconate (M+5). **F**) Bar plots showing the percent labeled fractions (y-axis, n=5 independent samples each) of glutamate, αKG, citrate and itaconate in ZFTA-RELA and ev-mNSCs incubated with 2mM U-^{13}C-glutamine for 24 h. Note that other labelled fractions can be derived from U-^{13}C-glutamine via multiple passages through the TCA cycle. Data are shown as mean ± SD and were analyzed by unpaired, two-tailed, two-sided t-test with 95% C.I. **G**) Schematic illustrating incorporation of glucose into the 5th itaconate carbon using U-^{13}C-glucose. Glucose (M+6) gives rise to pyruvate (M+3), which enters the citric acid cycle as citrate (M+2). Citrate (M+2) is then converted to aconitate (M+2) to be incorporated as itaconate (M+1). Note that the other 4 carbons of itaconate are derived from glutamine as depicted in Extended Data Fig. 6d. **H**) Bar plots showing the % labeled fractions (y-axis, n=5 independent samples each) of pyruvate, citrate, and itaconate in ZFTA-RELA and ev-mNSCs incubated with U-^{13}C-glucose (25 mM) for 24h. Note that other labelled itaconate fractions can be derived from U-^{13}C-glucose via multiple passages through the TCA cycle. Data are shown as mean ± SD and were analyzed by unpaired, two-tailed, two-sided t-test with 95% C.I.

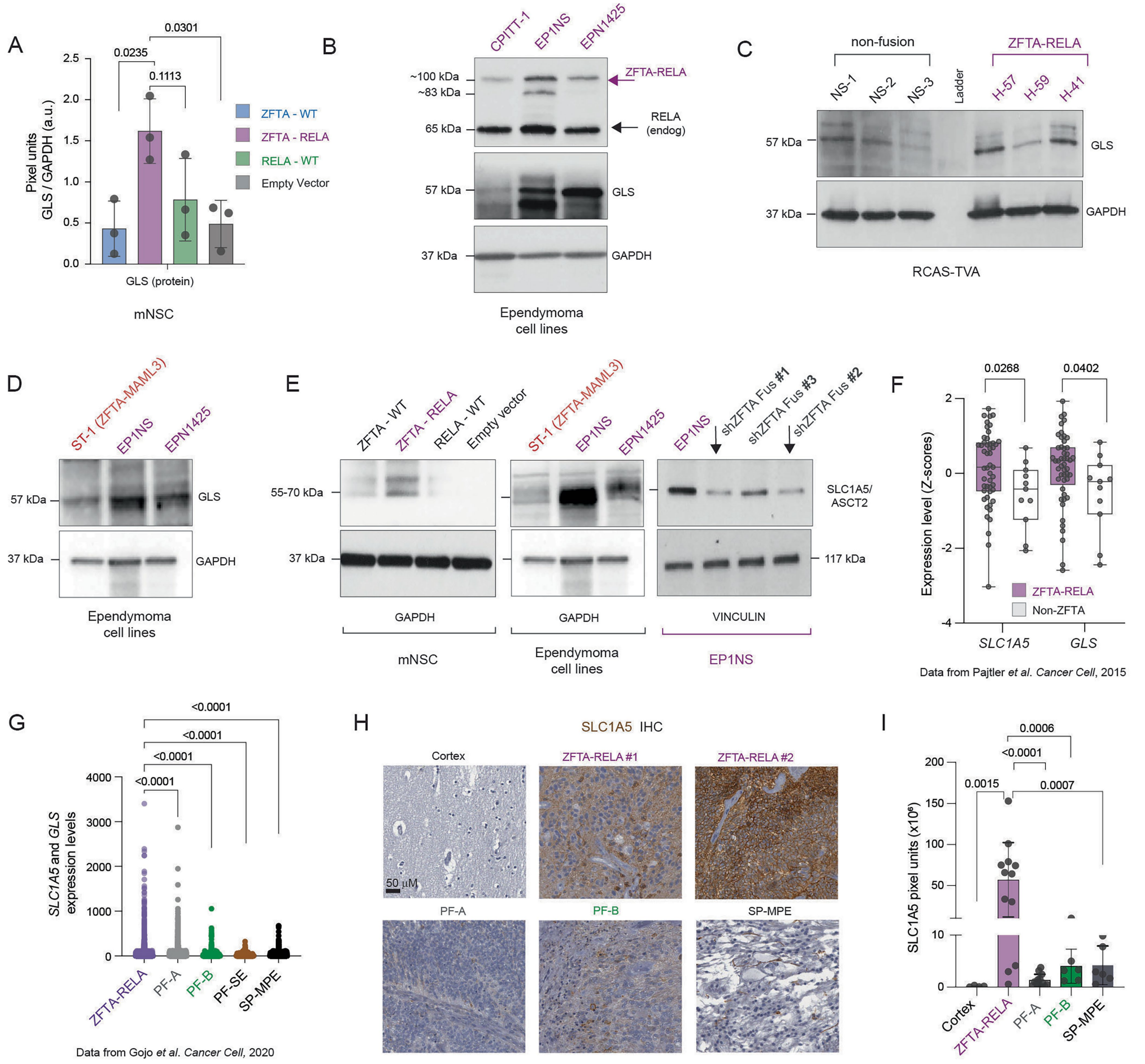

Extended Data Fig. 7 | ZFTA-RELA ependymomas show high GLS and SLC1A5 expression. A) Densitometric quantification (y-axis: pixel units) of GLS protein levels (normalized to GAPDH as control) shown as bar plots in ZFTA-RELA (purple), ZFTA-WT (blue), RELA-WT (green), and ev (gray) expressing mNSCs. Quantification was performed using Image J software from n=3 independent experiments. Data shown as mean ± SD and analyzed by one-way ANOVA with Tukey's multiple comparisons using 95% C.I. **B**) Representative Western blots showing GLS and ZFTA-RELA fusion protein levels (relative to GAPDH) in three patient-derived, ZFTA- RELA (CPITT-1, EP1NS, EPN1425, purple text) cell lines. Purple arrow indicates ZFTA-RELA fusion (higher molecular weights), and black arrow indicates endogenous RELA (lower molecular weight). **C-D**) Western blots depicting GLS levels in (**C**) three ZFTA-RELA (purple) and control non-fusion ependymoma cell lines (black) RCAS/TVA mouse models Ozawa T, et al., *Cell Reports*, 2018[12] and (**D**) in ZFTA-MAML3 (ST-1, red) vs ZFTA-RELA (EP1NS and EPN1425, purple) fusion cell lines relative to GAPDH. **E**) Western blots showing protein levels of the glutamine importer (SLC1A5/ ASCT2) in: - (left panel): ZFTA-RELA versus ev, ZFTA-WT, RELA-WT, and ev-mNSCs (relative to GAPDH). - (middle panel): Patient-derived ZFTA-MAML3 (ST-1, red) vs ZFTA-RELA (EP1NS and EPN1425, purple) fusion cell lines (relative to GAPDH). - (right panel): Patient-derived EP1NS cells with/without ZFTA-RELA fusion knockdown (n=3 independent shRNAs, relative to VINCULIN). shRNAs with best knockdown of ZFTA-RELA fusion indicated with black arrows. **F**) Box plot depicting the expression of *SLC1A5* and *GLS* mRNA levels in ZFTA-RELA fusion (n=49, purple) compared to YAP-1 fusion (n=11, white) ependymomas. Data were derived from Pajtler et al. *Cancer Cell* 2015[3] and plotted as z-scores (y-axis). Data shown as medians and interquartile ranges with ends of box plots representing highest and lowest observations. Data analyzed using Mann-Whitney test with 95% C.I. **G**) Expression levels of *SLC1A5* and *GLS* derived from single cell RNA sequencing of ZFTA-RELA fusion (purple), posterior fossa-group A (PF-A, gray), posterior fossa-group B (PF-B, green), posterior fossa-sub ependymoma (PF- SE, brown), and spinal myxopapillary (SP-MPE, black) ependymomas. Single-cell RNA sequencing data were derived from Gojo J et al. *Cancer Cell* 2020[43]. Data are depicted as scatter plots and analyzed using one-way ANOVA with Dunnett's multiple comparisons using 95% C.I. **H-I**) Representative SLC1A5 IHC images from ZFTA-RELA fusion, PF-A, PF-B, SP-MPE ependymomas and normal cerebral cortical tissue. (**I**) Bar plot (pixel units: y-axis) showing blinded quantification of SLC1A5 staining from ZFTA-RELA fusion (n=6), PF-A (n=7), PF-B (n=3), SP-MPE (n=3) ependymomas and normal cerebral cortical (n=3) tissue. Data were quantified using MATLAB from two independent regions from samples in Panwalkar et al. *Acta Neuropathologica*, 2017[65] Data are shown as mean ± SD and were analyzed using one-way ANOVA with Dunnett's multiple comparisons using 95% C.I.

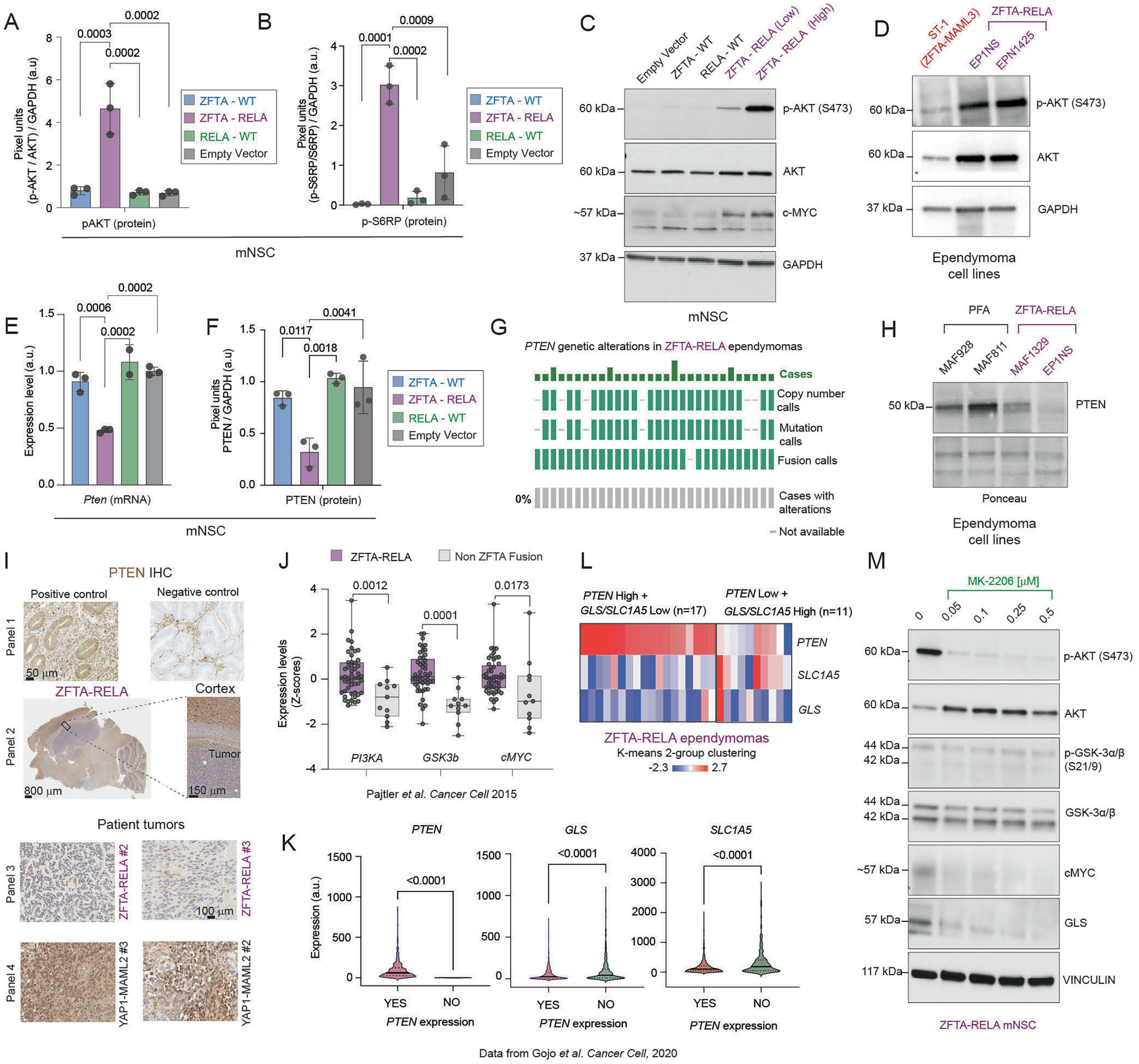

Extended Data Fig. 8 | See next page for caption.

Extended Data Fig. 8 | ZFTA-RELA lowers PTEN to drive glutamine metabolism. A-B) Bar plots showing densitometric quantification (y-axis: pixel units) for **A**) p-AKT (p-S473, normalized to total AKT and GAPDH) and **B**) p-S6RP levels (p-S235/S236, normalized to total S6RP and GAPDH) from Western blots in ZFTA-RELA fusion (purple), ZFTA-WT (blue), RELA-WT (green), and ev-mNSCs (gray). Quantification was performed using Image J software from n=3 independent experiments. Data are shown as mean ± SD and analyzed with one-way ANOVA with Tukey's multiple comparisons using 95% C.I. **C**) ZFTA-RELA mNSCs with titrated levels of high and low levels of ZFTA-RELA fusion expression (From Extended Data Fig. 1h); and, as controls, ev, RELA-WT, and ZFTA-WT mNSCs were used. Western blots show protein levels of p-AKT (p-S473), total AKT and c-MYC relative to GAPDH. **D**) Western blots showing protein levels of p-AKT (S473) and total AKT (relative to GAPDH) in EP1NS and EPN1425 ZFTA-RELA fusion vs ST-1 ZFTA-MAML3 patient-derived tumor cell lines. **E**) Bar plot showing *Pten* mRNA expression (y-axis, normalized to *Gapdh* mRNA levels, n=4 independent samples) in ZFTA-RELA (purple) compared to control ev (gray), RELA-WT (green), and ZFTA-WT (blue) mNSCs. Data are shown as mean ± SD and analyzed with one-way ANOVA with Dunnett's multiple comparisons using 95% C.I. **F**) Bar plots showing the densitometric quantification (y-axis: pixel units) of PTEN protein levels (normalized to GAPDH) from Western blots in ZFTA-RELA (purple), ZFTA-WT (blue), RELA-WT (green), and ev (gray) mNSCs. Quantification was performed using Image J software from n=3 independent experiments. Data are shown as mean ± SD and analyzed with one-way ANOVA with Tukey's multiple comparisons using 95% C.I. **G**) *PTEN* Oncoplot of ZFTA-RELA ependymoma patient sample (n=30, dark green) derived from Pediatric cBioPortal ependymoma GSE50385 dataset (https://pedcbioportal.kidsfirstdrc.org/). Oncoplot shows proportion of ZFTA-RELA fusion ependymomas (gray, 0%) harboring PTEN mutations, or fusions, or copy number alterations (light green). Each box represents an individual tumor. Hyphens (-) indicates cases where data was not available. **H**) Western blot of PTEN protein relative to (GAPDH or ponceau staining of total proteins as loading controls) in patient-derived ZFTA-RELA fusion (MAF-1329, EP1NS, EPN1425) vs PFA (MAF-811, MAF-928) cell lines. **I**) (Panel 1) Representative PTEN IHC images from positive control (left, *PTEN* intact patient derived uterine adenocarcinoma carcinoma) and negative controls (right, *PTEN* homozygous deleted uterine adenocarcinoma, note retained PTEN staining in non-tumor stromal cells as internal control). (Panel 2) Representative PTEN IHC images from ZFTA-RELA mouse model. Inset (indicated by a box) delineates PTEN staining within surrounding non-neoplastic mouse cortex as compared to low PTEN staining in the tumor. (Panel 3) Representative PTEN IHC images from two independent ZFTA-RELA fusion RELA ependymomas. (Panel 4) Representative PTEN IHC images from two independent YAP1-MAML2 fusion ependymomas. **J**) Box plot depicting the expression of *PI3K-α*, *GSK3α/β*, and *c-MYC* mRNA levels in ZFTA-RELA fusion (n=49, purple) compared to non ZFTA-fusion (n=11, white) ependymomas. Data were derived from Pajtler et al. *Cancer Cell* 2015[3] and plotted as z-scores (y-axis). Data shown as medians and interquartile ranges with ends of box plots representing the highest and lowest observations. Data analyzed using Mann-Whitney test with 95% C.I. **K**) Violin plots demonstrating expression of *PTEN*, *GLS*, and *SLC1A5* in ZFTA-RELA fusion tumor cells with/without *PTEN* expression. Expression data derived from single-cell RNA sequencing of patient ZFTA-RELA fusion tumors from Gojo J et al. *Cancer Cell* 2020[43]. Plots show medians with ends of the violin representing highest and lowest observations. Data analyzed using Mann-Whitney test with 95% C.I. **L**) Gene expression values of *PTEN*, *SLC1A5*, and *GLS* from ZFTA-RELA ependymomas (n=28) obtained from the Pediatric cBioPortal ependymoma GSE50385 dataset (https://pedcbioportal.kidsfirstdrc.org/). K-means clustering of gene expression was used to segregate patients into two groups: *PTEN* high + *GLS/SLC1A5* low (n=17) and *PTEN* low + *GLS/SLC1A5* high (n=11). **M**) Representative Western blots showing p-AKT (p-S473), total AKT, p-GSK3α/β (S21/9), total GSK3α/β, c-MYC, and GLS relative to VINCULIN protein levels in ZFTA-RELA fusion mNSCs after treatment with an AKT inhibitor, MK-2206 at the indicated concentrations for 24 h.

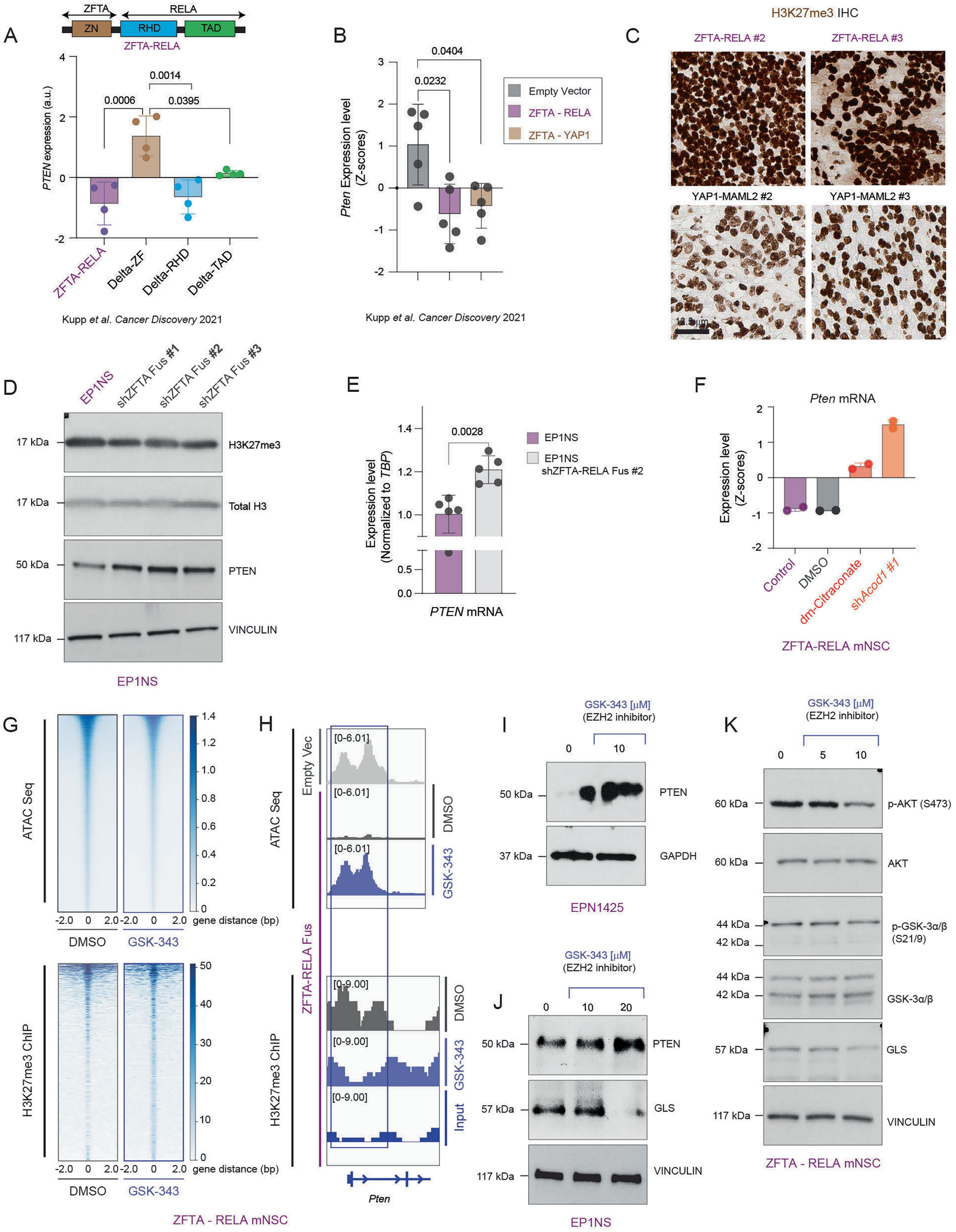

Extended Data Fig. 9 | See next page for caption.

Extended Data Fig. 9 | ZFTA-RELA epigenetically lowers PTEN. A) *PTEN* expression in 293T cells (Z-scores, y-axis) expressing full length ZFTA-RELA fusion protein (purple), or deletion mutants: Delta-ZF (brown, ZF: Zinc Finger), Delta-RHD (blue, RHD: REL Homology Domain) and Delta-TAD (green, TAD: Transactivating domain) depicted as bar graphs (n=4 independent samples). Data are derived from Kupp et al. *Cancer Discovery* 2021[10]. Data are shown as mean ± SD and analyzed by one-way ANOVA with Tukey's multiple comparisons using 95% C.I. **B**) *Pten* expression levels (z-score, y-axis) in mNSCs expressing ev (gray), ZFTA-RELA fusion (purple), or ZFTA-YAP1 fusion (brown) (n=5 independent samples). Data are derived from Kupp et al.[10], shown as mean ± SD and analyzed by one-way ANOVA with Dunnett's multiple comparisons using 95% C.I. **C**) Representative H3K27me3 IHC images from ZFTA-RELA (purple text) and YAP1-MAML2 fusion (black text) patient ependymomas. **D**) Western blots for H3K27me3 in relation to total H3; and PTEN protein levels in relation to VINCULIN in EP1NS patient-derived cells with/without shZFTA-RELA fusion knockdown (n=3 independent shRNAs). **E**) Bar graph showing *PTEN* mRNA expression (y-axis, normalized to that of the housekeeping gene TATA binding protein, *TBP*) in EP1NS cells with/without shZFTA-RELA fusion knockdown #2. Data shown as mean ± SD of n=5 independent samples each and analyzed by unpaired, two-tailed, two-sided t-test with 95% C.I. **F**) Bar graph showing *Pten* mRNA levels (z-scores, y-axis) in ZFTA-RELA mNSCs untreated (purple), or treated with vehicle (gray), or dm-citraconate (10mM for 24h, red); and ZFTA-RELA mNSCs with *Acod1* knockdown (shRNA #1, orange). Data shown as mean ± SD of n=2 independent samples. **G**) Heatmaps of ATAC-seq (top panel) and H3K27me3 ChIP-seq (bottom panel) depicting the significantly altered consensus regions in ZFTA-RELA mNSCs treated with DMSO (gray) or 10μM GSK-343 (violet) for 96h. **H**) Representative ATAC sequencing tracks (top panel) at the *Pten* gene locus in ev (top, light gray) and ZFTA-RELA mNSCs treated with DMSO (middle, dark gray) or 10μM GSK-343 (EZH2 inhibitor, bottom, violet) for 96h. Representative H3K27me3-ChIP tracks (bottom panel) at the *Pten* locus in ZFTA-RELA mNSCs treated with DMSO (gray) or 10μM GSK-343 (EZH2 inhibitor, violet) for 96h. Input track is shown in blue. **I**) Western blots showing protein levels of PTEN (relative to GAPDH) in EPN1425 patient-derived cells treated with the EZH2 inhibitor, GSK-343 at the indicated concentrations for 96h. **J**) Western blots showing protein levels of PTEN and GLS (relative to VINCULIN) in EP1NS patient-derived cells treated with the EZH2 inhibitor, GSK-343 at the indicated concentrations for 96h. **K**) Western blots showing protein levels of p-AKT (S473), total AKT, p-GSK3α/β (S21/9), total GSK3α/β, and GLS in relation to vinculin in ZFTA-RELA fusion mNSCs after treatment with the EZH2 inhibitor, GSK-343 at the indicated concentrations for 96h.

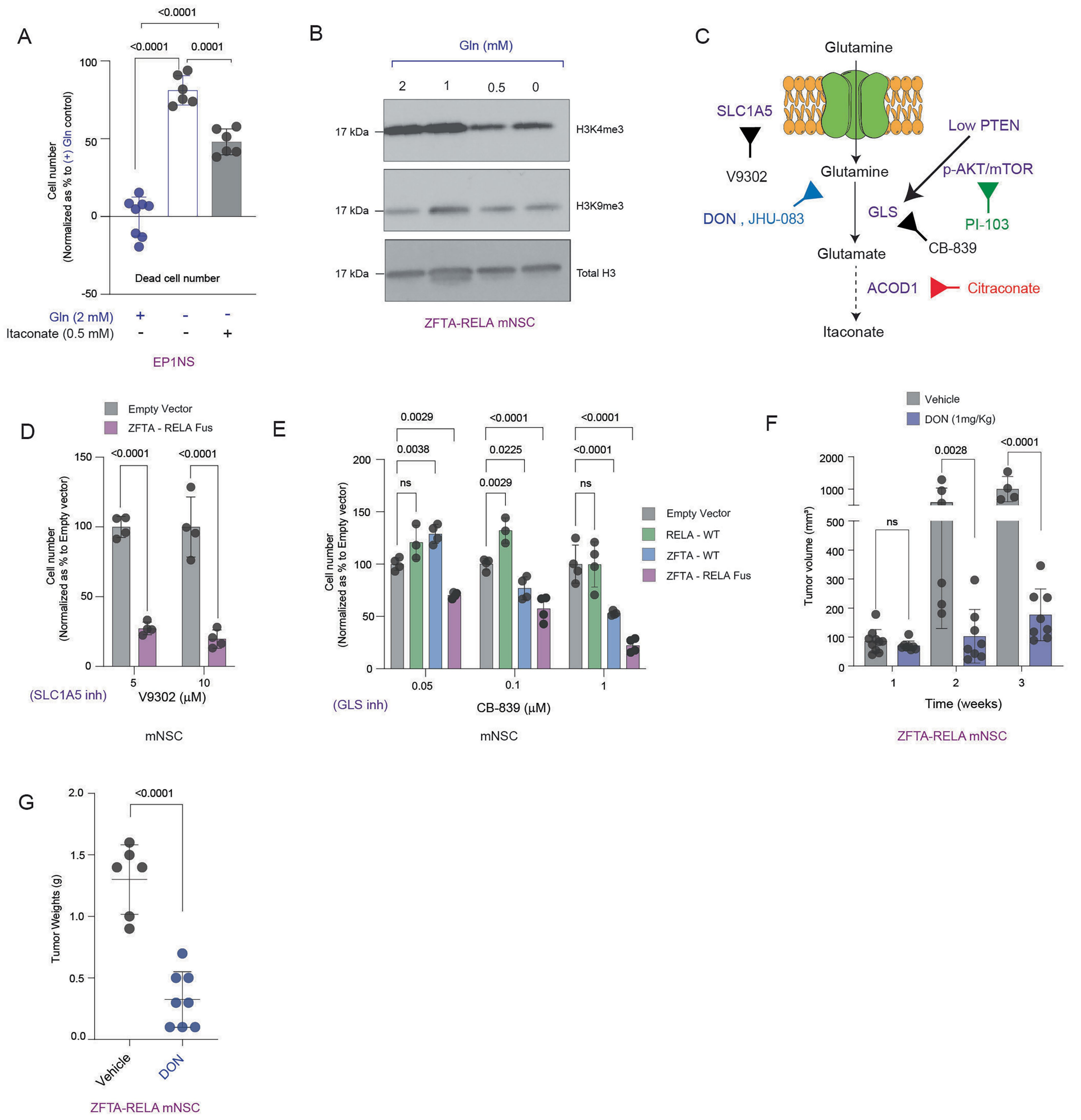

Extended Data Fig. 10 | Inhibiting glutamine metabolism is therapeutic in ZFTA-RELA ependymomas. A) Dead cell number (y-axis, normalized as percentage to that in control cells in glutamine replete condition) in patient-derived EP1NS cells grown in complete media with 2mM glutamine (blue circles); or upon glutamine deprivation (clear bars); or upon glutamine deprivation supplemented with 0.5mM itaconate (gray bars). Data shown as mean ± SD from n=6 independent samples, each, and analyzed using one-way ANOVA with Tukey's multiple comparisons using 95% C.I. **B**) Western blots for H3K4me3 and H3K9me3 relative to total H3 in ZFTA-RELA mNSCs cultured in complete media (2mM glutamine) or decreasing concentrations of glutamine (1, 0.5, or 0mM) for 96h. **C**) Schematic depicting the key nodes of glutamine metabolic pathway leading to itaconate biosynthesis along with the drugs/compounds used to inhibit them. V9302 is a pharmacological inhibitor of the glutamine transporter SLC1A5[47]; 6-diazo-5-oxo-norleucine (DON) and JHU-083 are glutamine antagonists[49]; CB-839 is an inhibitor of glutaminase[48]; PI-103 is a dual inhibitor of PI3K/mTOR pathway inhibitor; and citraconate is a competitive inhibitor of ACOD1[26] that opposes itaconate metabolism. **D**) Cell numbers (y-axis, normalized as percentage to total live cells in control ev cells) in ZFTA-RELA (purple) or control ev (gray) expressing mNSCs after treatment with indicated concentrations of V-9302 for 72h. Data shown as mean ± SD of n=4 independent samples each, and analyzed by Šídák's test with 95% C.I. **E**) Cell numbers (y-axis, normalized as percentage to total live cells in control ev cells) in ZFTA-RELA (purple) versus control ev (gray), or ZFTA-WT (blue), or RELA-WT (green) expressing mNSC after treatment with indicated concentrations of CB-839 for 96h. Data shown as mean ± SD of n=4 independent samples each. Statistical analysis was performed using two-way ANOVA with adjusted p values shown with Dunnett's multiple comparisons using 95% C.I. **F-G**) Tumor volume (y-axis, mm^3, **F**) and tumor weights (y-axis, grams, **G**) of ZFTA-RELA mNSCs xenografted into flanks of mice and treated with DON (twice a week at 1mg/kg, i.p. for 3 weeks, n=8, blue) or vehicle (n=6, gray). Data shown as mean ± SD. Statistical analysis was performed in (**F**) using two-way ANOVA with Tukey's multiple comparisons using 95% C.I. Data in (**G**) was analyzed by unpaired, two-tailed, two-sided t-test with 95% C.I.

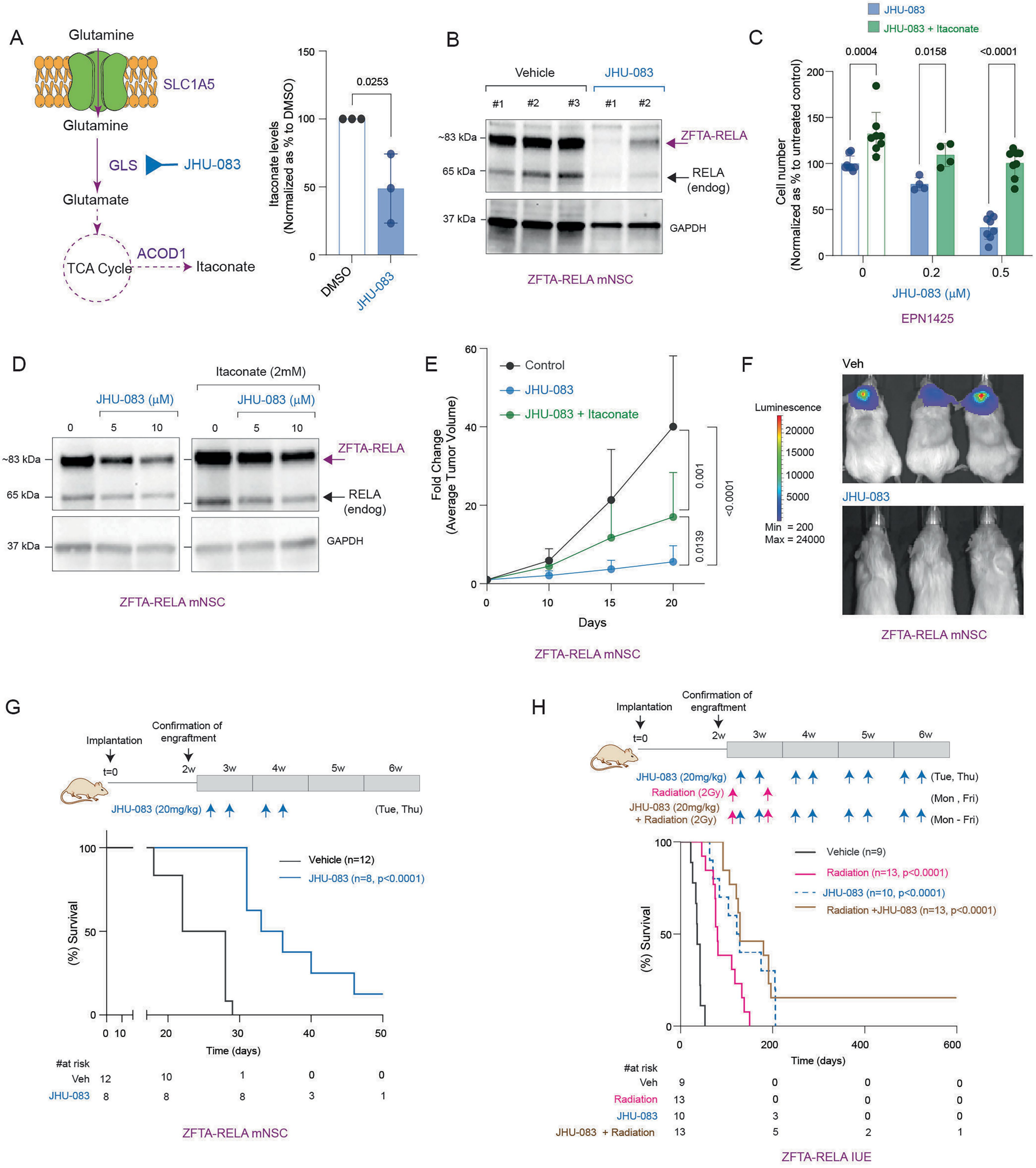

Extended Data Fig. 11 | See next page for caption.

Extended Data Fig. 11 | JHU-083 treatment reduces itaconate production and kills ZFTA-RELA tumor cells. A) Schematic (left) illustrates itaconate synthesis from glutamine. Bar plot (right) showing itaconate levels (y-axis, normalized to total number of live cells and shown as % of itaconate in vehicle treated cells) in ZFTA-RELA mNSCs treated with DMSO (gray) or 10µM of JHU-083 (light blue) for 48 h. Data shown as mean ± SD of n=3 independent samples each, and analyzed by unpaired, two-tailed, two-sided t-test with 95% C.I. **B**) Western blots for RELA (relative to GAPDH) from ZFTA-RELA fusion tumor samples derived from subcutaneous implantation of ZFTA-RELA mNSCs (shown in Extended Data Fig. 11e) in the flanks of mice. Western blots depict changes in in vivo protein levels of ZFTA-RELA fusion (purple arrow, ~83 kDa) and endogenous RELA (black arrow, 65 kDa) in vehicle (gray text, n=3 independent tumors) or JHU-083 (light blue text, n=2 independent tumors) treated tumor tissues. **C**) Cell number (y-axis, normalized as percentage to total number of live cells in vehicle-treated control cells) in patient derived EPN1425 ZFTA-RELA fusion cells treated with JHU-083 alone (light blue) or a combination of JHU-083 and 1mM Itaconate (green) at the indicated concentrations for 96h. Data shown as mean ± SD of n=4 independent samples each, and analyzed by two-way ANOVA with adjusted p values shown after multiple comparisons using 95% C.I. **D**) Western blots for RELA (relative to GAPDH) depicting changes in ZFTA-RELA fusion protein levels (purple arrow, ~83 kDa) and endogenous RELA (black arrow, 65 kDa) in ZFTA-RELA mNSCs treated with vehicle or JHU-083 alone (left), or in combination with 2mM Itaconate (right) at the indicated concentrations for 96h. **E**) Fold change in the average tumor volume (y-axis) plotted against time (days post injection, x-axis) of ZFTA-RELA mNSCs xenografted in the flanks of mice and treated with vehicle (black, n=4), or JHU-083 alone (20mg/kg, p.o., 2 doses a week for two weeks, light blue, n=6), or a combination of JHU-083 (20mg/kg, p.o.) and itaconate (25mg/kg, i.v., 3 doses a week for two weeks, green, n=8). Data shown as mean ± SD and analyzed by two-way ANOVA with Tukey's multiple comparisons using 95% C.I. **F-G**) Representative bioluminescence images (**F**) and Kaplan-Meier analysis (**G**) of mice with ZFTA-RELA fusion mNSC orthotopic (cortical) xenografts treated with vehicle (n=17, black) or JHU-083 (blue, n=8, 20mg/kg, p.o.). Median survival was 25 days for vehicle treated mice and 34.5 days for JHU-083 treatment. Statistical analysis was performed using Log-rank test with 95% C.I. Number of animals at risk is indicated below the graph for each time point shown. Schematic illustration of the JHU-083 (20mg/kg, p.o.) treatment regimen is shown above the graph **H**) Kaplan-Meier analysis from ZFTA-RELA IUE mice treated with vehicle (black, n=9 animals), radiation (pink, 2 doses of 2Gy, n=13) or a combination of radiation (2 doses of 2Gy) and JHU-083 (brown, 20mg/kg, p.o. 5 weeks, n=13 animals). Median survival for animals treated with Vehicle (36 days), radiation alone (80 days), JHU-083 alone (125 days), and a combination of JHU-083 + radiation (129 days) was noted. Statistical analysis was performed using Log-rank test with 95% C.I. Dotted line (light blue) shows the Kaplan-Meier curve from Fig. 5e for JHU-083 alone. Number of animals at risk is indicated below the graph for each time point shown in the survival analysis. Schematic illustration of dosing regimens for JHU-083 (20mg/kg, p.o.), radiation (2 doses of 2Gy) and their combination treatment is shown above the graph.

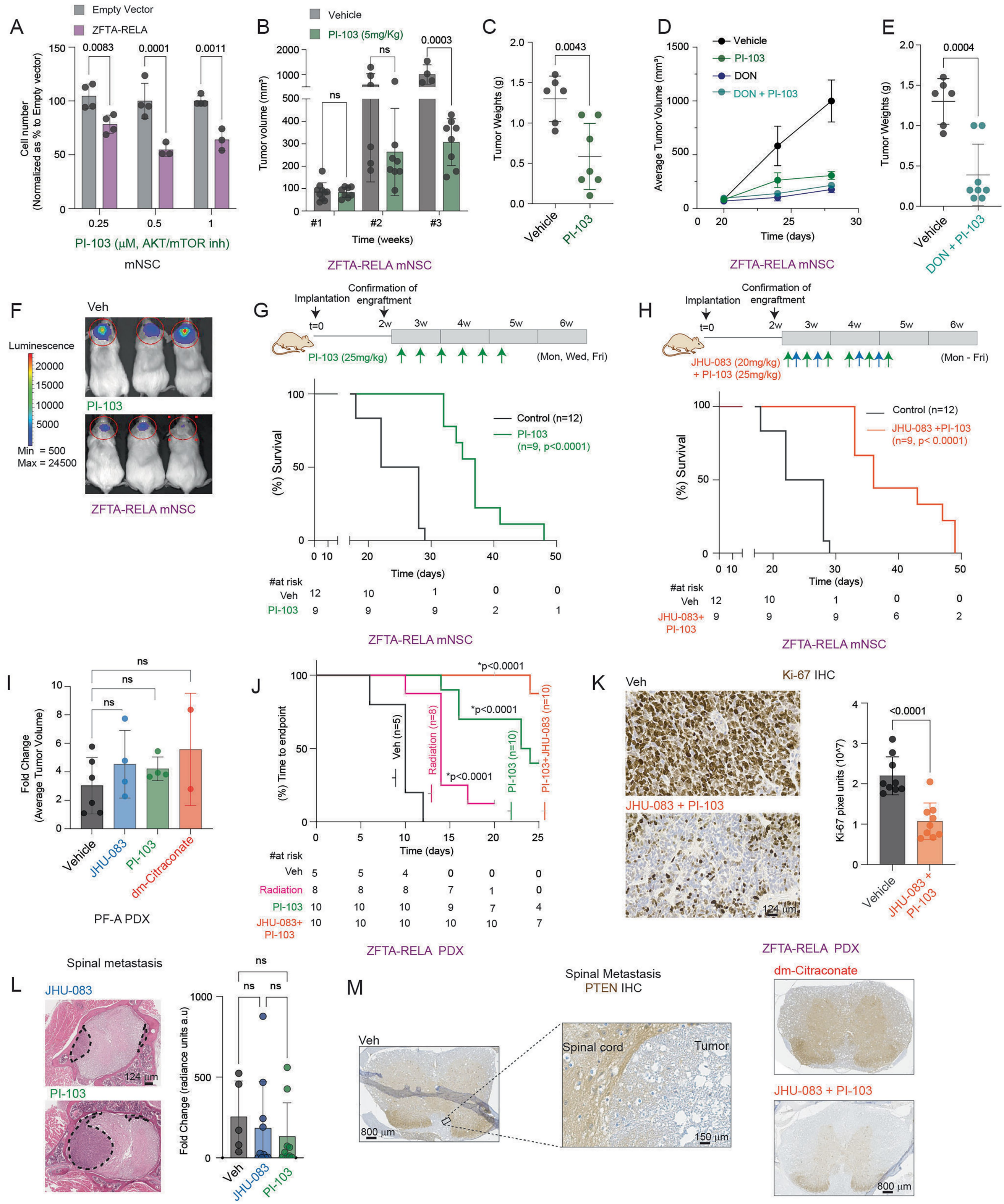

Extended Data Fig. 12 | See next page for caption.

Extended Data Fig. 12 | Combined glutamine antagonism and PI3K/AKT inhibition is therapeutic in ZFTA-RELA ependymomas. A) Cell number (y-axis, normalized as percentage to total number of live cells in vehicle-treated control ev cells) in ZFTA-RELA (purple) or ev expressing mNSCs (gray) after treatment with PI3K/mTOR inhibitor, PI-103 at indicated concentrations for 72h. Data shown as mean ± SD of n=4 independent samples each, and analyzed by two-way ANOVA with adjusted p values shown after Šídák's multiple comparisons using 95% C.I. **B-C**) ZFTA-RELA mNSCs xenografted into flanks of mice were treated with PI-103 (thrice a week at 5mg/kg, i.p., green, n=5) or vehicle (gray, n=4) for 3 weeks. Graphs indicate tumor volume (y-axis, mm^3, **B**) and tumor weights (y-axis, grams, **C**). Data are shown as mean ± SD. Statistical analysis was performed in (**B**) using two-way ANOVA with Tukey's multiple comparisons using 95% C.I. Data in (**C**) was analyzed by unpaired, two-tailed, two-sided t-test with 95% C.I. **D-E**) Fold Change (mean ± SEM) in average tumor volume (**D**, y-axis) and tumor weights (**E**, y-axis, grams) of ZFTA-RELA mNSCs xenografted into flanks of mice and treated with vehicle (gray, n=6, each, animals), or DON (n=8, blue, animals), or PI-103 (n=5, animals, green), or a combination of DON and PI-103 for 3 weeks (n=8, animals, teal). Data in shown as mean ± SD (**E**) and was analyzed by unpaired, two-tailed, two-sided t-test with 95% C.I. **F-G**) Representative bioluminescence images (**F**) and Kaplan-Meier analysis (**G**) of mice with ZFTA-RELA fusion mNSC orthotopic (cortical) xenografts treated with vehicle (n=17, animals, black) or PI-103 (green, n=9, animals, 25mg/kg). Median survival was 25 days for vehicle treated and 37 days for PI-103 treated mice. Statistical analysis was performed using Log-rank test with 95% C.I. Number of animals at risk is indicated below the graph for each time point shown in the survival analysis. Schematic illustration of dosing regimens is shown above the graph. **H**) Kaplan-Meier analysis of survival in mice with ZFTA-RELA fusion mNSC orthotopic (cortical) xenografts and treated with vehicle (n=17, red animals); or a combination of JHU-083 (20mg/kg) and PI-103 (25mg/kg) (orange, n=9 animals). Median survival was 25 days for vehicle treated mice and 36 days for animals receiving combined JHU-083 and PI-103 treatment. Statistical analysis was performed using Log-rank test with 95% c.i. Number of animals at risk is indicated below the graph for each time point shown in the survival analysis. Schematic illustration of dosing regimens is shown above the graph. **I**) Bar graph showing the fold change in the average tumor volume (y-axis, at day 21) of non-fusion MAF-811(Posterior Fossa Type A) ependymoma PDX xenografted subcutaneously in the flanks of NSG mice and treated with vehicle (gray, n=6 independent samples), or JHU-083 (20mg/kg, p.o., 2 doses/week, light blue, n=4 independent samples), or PI-103 (25mg/kg, i.p., 3 doses/week, green, n=4 independent samples), or dm-citraconate (25mg/kg, i.v., 3 doses/week, red, n=2 independent samples). Data shown as mean ± SD and analyzed by one-way ANOVA with a Tukey's multiple comparisons using 95% C.I. **J**) Kaplan-Meier analysis of time to reach endpoint (tripling of tumor volume) in MAF-1329 (ZFTA-RELA fusion) PDXs xenografted subcutaneously into the flanks of NSG mice and treated with vehicle (black, n=5 independent samples), or radiation (2 doses of 2Gy each, pink, n=8 independent samples), or PI-103 (25mg/kg, i.p., 3 doses/week, green, n=10 independent samples), or a combination (orange, n=10 independent samples) of JHU-083 and PI-103. Median number of days to reach endpoint for tumors treated with Vehicle (10 days), Radiation (14 days), PI-103 (23.5 days) is noted. Tumors of mice treated with combined JHU-083, and PI-103 did not reach endpoint when experiment was stopped. Statistical analysis was performed using Log-rank test with 95% C.I. Number of animals at risk is indicated below the graph for each time point shown in the survival analysis. Schematic illustration of dosing regimens is shown above the graph. **K**) Representative Ki-67 IHC images (left panel) from ZFTA-RELA PDX tumors treated with vehicle (gray) or a combination of JHU-083 and PI-103 (orange). Bar graphs (right panel) show blinded quantification for Ki-67 IHC (pixel units, y-axis) in vehicle treated (gray, n=3 independent tumors); or JHU-083+PI103 treated (orange, n=3 independent tumors) ZFTA-RELA PDX tumors. Data were quantified using MATLAB from three independent and randomly selected regions for each sample. Data are shown as mean ± SD and were analyzed by unpaired, two-tailed, two-sided t-test with 95% C.I. **L**) Representative cross-sectional H&E images (left) of spinal cords from single agent JHU-083 (top), or PI-103 (bottom) treated ZFTA-RELA mice. Dotted region encapsulates regions of metastases. Bar graph shows quantification (right) of fold change in the radiance units from spinal bioluminescent signal in mice treated with vehicle (n=5, black), or JHU-083 (20mg/kg, p.o., n=10), or PI-103 (20mg/kg, i.p., n=10) treatment. Data shown as mean ± SD and analyzed by one-way ANOVA with Dunn's multiple comparisons using 95% C.I. **M**) Representative PTEN IHC images of spinal cord cross sections from ZFTA-RELA tumor bearing mice treated with vehicle (gray, left panel); dm-citraconate alone (red, right top); or JHU-083+PI-103 (right bottom). Inset (indicated by a box) delineates PTEN staining within surrounding non-neoplastic mouse spinal cord as compared to low PTEN staining in the metastatic spinal tumor.

nature portfolio

Corresponding author(s): Sriram Venneti

Last updated by author(s): Dec 2, 2025

Reporting Summary

Nature Portfolio wishes to improve the reproducibility of the work that we publish. This form provides structure for consistency and transparency in reporting. For further information on Nature Portfolio policies, see our Editorial Policies and the Editorial Policy Checklist.

Statistics

For all statistical analyses, confirm that the following items are present in the figure legend, table legend, main text, or Methods section.

n/a	Confirmed	
☐	☒	The exact sample size (*n*) for each experimental group/condition, given as a discrete number and unit of measurement
☐	☒	A statement on whether measurements were taken from distinct samples or whether the same sample was measured repeatedly
☐	☒	The statistical test(s) used AND whether they are one- or two-sided *Only common tests should be described solely by name; describe more complex techniques in the Methods section.*
☒	☐	A description of all covariates tested
☐	☒	A description of any assumptions or corrections, such as tests of normality and adjustment for multiple comparisons
☐	☒	A full description of the statistical parameters including central tendency (e.g. means) or other basic estimates (e.g. regression coefficient) AND variation (e.g. standard deviation) or associated estimates of uncertainty (e.g. confidence intervals)
☐	☒	For null hypothesis testing, the test statistic (e.g. *F*, *t*, *r*) with confidence intervals, effect sizes, degrees of freedom and *P* value noted *Give P values as exact values whenever suitable.*
☒	☐	For Bayesian analysis, information on the choice of priors and Markov chain Monte Carlo settings
☒	☐	For hierarchical and complex designs, identification of the appropriate level for tests and full reporting of outcomes
☐	☒	Estimates of effect sizes (e.g. Cohen's *d*, Pearson's *r*), indicating how they were calculated

Our web collection on statistics for biologists contains articles on many of the points above.

Software and code

Policy information about availability of computer code

Data collection	All metabolomics data was collected and analyzed using Agilent MassHunter software. qRT-PCR data was gathered using 7500 Software v2.3. Cell number for cell viability experiments were collected using the Countess III cell counter (Thermo Fisher Scientific). All in vivo bioluminescence data was acquired by IVIS Spectrum (Perkin Elmer) instrument. Immunohistochemistry images were visualized using the Aperio Vista scanning system (AperioScanscope Scanner) and Aperio ImageScope software program was used to view each slide at 40x magnification.
Data analysis	All immunoblot images were quantified using Image J 1.53k. Graphs were generated and statistical analyses were performed using Prism software (version 9.5.1, Graph Pad, La Jolla, CA). Quantification of Immunohistochemistry images was performed using on MATLAB using an automated analysis program previously published by our lab (Panwalkar et al, Acta Neuropathologica, 2017 PMID:28733933). For 13C labelled samples, isotopic correction of raw GC-MS peaks for all reported metabolites was performed using the IsoCorrectoR package (v 1.5.1) available as part of the Bioconductor library (BioC 3.8) and implemented in R (CRAN 3.6.1). DEseq2 was used to identify differentially upregulated and downregulated genes from the RNA seq experiments and the differentially enriched pathways were identified using Enrichr (https://maayanlab.cloud/Enrichr/).

For manuscripts utilizing custom algorithms or software that are central to the research but not yet described in published literature, software must be made available to editors and reviewers. We strongly encourage code deposition in a community repository (e.g. GitHub). See the Nature Portfolio guidelines for submitting code & software for further information.

Data

Policy information about availability of data

All manuscripts must include a data availability statement. This statement should provide the following information, where applicable:

- Accession codes, unique identifiers, or web links for publicly available datasets
- A description of any restrictions on data availability
- For clinical datasets or third party data, please ensure that the statement adheres to our policy

The ChIP seq and ATAC seq data generated in this study are accessible through the GEO series accession numbers GSE294954 and GSE294955. Gene expression data shown in (Extended Data Fig 7F, 8J) were derived from Pajtler et al, Cancer Cell, 2015 and were downloaded from the NCBI GEO database with the accession number GSE64415. Single cell RNA sequencing data shown in (Extended Data Fig 7G, 8K) are from Gojo et al, Cancer Cell, 2020 and were downloaded using the accession number GSE141460. Data in (Fig 4G, Extended Data Fig 8G, 8L) derived from Pediatric cbioportal ependymoma GSE50385 dataset (https://pedcbioportal.kidsfirstdrc.org/).

Research involving human participants, their data, or biological material

Policy information about studies with human participants or human data. See also policy information about sex, gender (identity/presentation), and sexual orientation and race, ethnicity and racism.

Reporting on sex and gender	*Use the terms sex (biological attribute) and gender (shaped by social and cultural circumstances) carefully in order to avoid confusing both terms. Indicate if findings apply to only one sex or gender; describe whether sex and gender were considered in study design; whether sex and/or gender was determined based on self-reporting or assigned and methods used.* *Provide in the source data disaggregated sex and gender data, where this information has been collected, and if consent has been obtained for sharing of individual-level data; provide overall numbers in this Reporting Summary. Please state if this information has not been collected.* *Report sex- and gender-based analyses where performed, justify reasons for lack of sex- and gender-based analysis.*
Reporting on race, ethnicity, or other socially relevant groupings	*Please specify the socially constructed or socially relevant categorization variable(s) used in your manuscript and explain why they were used. Please note that such variables should not be used as proxies for other socially constructed/relevant variables (for example, race or ethnicity should not be used as a proxy for socioeconomic status).* *Provide clear definitions of the relevant terms used, how they were provided (by the participants/respondents, the researchers, or third parties), and the method(s) used to classify people into the different categories (e.g. self-report, census or administrative data, social media data, etc.)* *Please provide details about how you controlled for confounding variables in your analyses.*
Population characteristics	*Describe the covariate-relevant population characteristics of the human research participants (e.g. age, genotypic information, past and current diagnosis and treatment categories). If you filled out the behavioural & social sciences study design questions and have nothing to add here, write "See above."*
Recruitment	*Describe how participants were recruited. Outline any potential self-selection bias or other biases that may be present and how these are likely to impact results.*
Ethics oversight	*Identify the organization(s) that approved the study protocol.*

Note that full information on the approval of the study protocol must also be provided in the manuscript.

Field-specific reporting

Please select the one below that is the best fit for your research. If you are not sure, read the appropriate sections before making your selection.

☒ Life sciences ☐ Behavioural & social sciences ☐ Ecological, evolutionary & environmental sciences

For a reference copy of the document with all sections, see nature.com/documents/nr-reporting-summary-flat.pdf

Life sciences study design

All studies must disclose on these points even when the disclosure is negative.

Sample size	For in vivo animal experiments sample size was calculated based on tumor variance to use at least n= 5 -20 mice to detect differences in overall survival with 80% power (0.05 significance). All metabolomics, isotope tracing, and qPCR experiments, utilized sample sizes of 4-5 biological replicates and the number of replicates were chosen based on the variability observed in pilot studies. For RNA sequencing, ChIP sequencing, and ATAC sequencing, n=2 replicates were utilized for each sample shown. For cell viability and cell count experiments a minimum of n=3 replicates were used per experiment and each experiment was repeated at least twice with the exact number indicated in the Figure legends and in the Statistics and Reproducibility section of the methods.
Data exclusions	No data was excluded from the analyses.
Replication	All experiments were reproduced atleast twice with n=3 independent experimental replicates unless noted. The exact number of independent

Replication	replicates or samples is indicated in the Figure legends and in the Statistics and Reproducibility section of the methods.
Randomization	All in vivo experiments were performed after randomizing the mice to avoid any bias. The cells used in the in vitro experiments were not randomized as they were collected from a homogeneous, clonally identical population.
Blinding	Quantification of immunohistochemical staining was performed in a blinded manner where an experimenter unaware of the study design captured JPEG images from three randomly selected areas of stained sections for every sample. For in vivo experiments blinding was not possible since Vehicle/drug treatments needed to be conducted in all tumor bearing mice.

Reporting for specific materials, systems and methods

We require information from authors about some types of materials, experimental systems and methods used in many studies. Here, indicate whether each material, system or method listed is relevant to your study. If you are not sure if a list item applies to your research, read the appropriate section before selecting a response.

Materials & experimental systems

n/a	Involved in the study
☐	☒ Antibodies
☐	☒ Eukaryotic cell lines
☒	☐ Palaeontology and archaeology
☐	☒ Animals and other organisms
☒	☐ Clinical data
☒	☐ Dual use research of concern
☒	☐ Plants

Methods

n/a	Involved in the study
☐	☒ ChIP-seq
☒	☐ Flow cytometry
☒	☐ MRI-based neuroimaging

Antibodies

Antibodies used	The following antibodies were used in the immunoblotting experiments, RELA (Cell Signaling Technology #8242, 1:1000), GAPDH (Cell Signaling Technology, #2118, 1:10,000), Vinculin (Sigma Aldrich, #V9264, 1:40,000), ACOD1-human (Abcam #ab222411, 1:1000 and Novus Biologicals #NBP3-06244, 1:1000), ACOD1-mouse (Cell Signaling Technology #17805, 1:1000), ZFTA (C11orf95) (VWR #89379-010, Supplier number #AP11349B, 1:1000), RFP (Abcam #Ab124754, 1:1000), MAML3 (Invitrogen #PA5-13678, 1:1000), SLC1A5 (Cell Signaling Technology #5345, 1:1000), Glutaminase-human (Cell Signaling Technology #49363, 1:1000), Glutaminase-mouse (Invitrogen #PA5-35365, 1:1000), c-MYC (Abcam #32072, 1:1000), PTEN (Cell Signaling Technology #9559, 1:1000), p-AKT (S473) (Cell Signaling Technology #9271, 1:1000), AKT (Cell Signaling Technology #4056, 1:1000), p-S6RP (S235/236) (Cell Signaling Technology #4858, 1:1000), S6RP (Cell Signaling Technology #2217, 1:1000), p-GSK3α/β (Cell Signaling Technology #9331, 1:1000), GSK3α/β (Cell Signaling Technology #5676, 1:1000), H3K4me3 (Cell Signaling Technology #9751, 1:1000), H3K9me3 (Cell Signaling Technology #13969, 1:1000), H3K27Ac (Cell Signaling Technology #8173, 1:1000), H3K27me3 (EMD Millipore #07-449, 1:1000), and Total H3 (Cell Signaling Technology #3638, 1:5000). The following secondary antibodies were used Goat-anti-mouse (BIORAD, #1706516), Goat-anti-rabbit (BIORAD, #1706515). For immunohistochemistry, a rabbit monoclonal anti-ACOD1 antibody (1:200, Abcam, #ab238580) or anti-PTEN (1:200, Abcam, #ab170941), H3K27me3 (EMD Millipore #07-449, 1:150), Ki-67 (Invitrogen #MA5-14520, 1:400), and SLC1A5 (Sigma Aldrich #HPA035240, 0.1ug/mL) were used.
Validation	RELA (Cell Signaling Technology #8242): Figs.1E, 1G, Figs. 2A, 2C, 2H, 2J Figs. 3B, 3H, 3L, Figs. 5C, 5G Extended Data Figs. 1H, 3A, 3B, 3D, 3E, 3F, 3I, 3M, 3N, 7B, 11B, 11D. ACOD1-mouse (Cell Signaling Technology #17805): Figs. 1E, Extended Data Figs. 1I, 1L, 2A, 5N ACOD1-human (Abcam #ab222411): Fig 1H, Extended Data Figs. 1E, 2A, 3C, ACOD1-human (Novus Biologicals #NBP3-06244): Extended Data Fig. 1E ZFTA (C11orf95) (VWR #89379-010, Supplier number #AP11349B): Figs. 3B, 3C, Extended Data Figs. 5C, 5D, 5E, 5F RFP (Abcam #Ab124754):Fig. 3H MAML3 (Invitrogen #PA5-13678): Fig 5F SLC1A5 (Cell Signaling Technology #5345): Extended Data Fig 7E Glutaminase-human (Cell Signaling Technology #49363): Fig 4C, Extended Data Figs. 7B, 7D, 9J Glutaminase-mouse (Invitrogen #PA5-35365): Figs. 4C, 4H, Extended Data Figs. 7C, 8M, 9K c-MYC (Abcam #32072): Fig 4H, Extended Data Figs. 8C, 8M PTEN (Cell Signaling Technology #9559): Figs. 4E, 4K, Extended Data Figs. 8H, 9D, 9I, 9J p-AKT (S473) (Cell Signaling Technology #9271): Fig 4E, 4H, Extended Data Figs. 8C, 8D, 8M, 9K AKT (Cell Signaling Technology #4056): Fig 4E, 4H, Extended Data Figs. 8C, 8D, 8M, 9K p-S6RP (S235/236) (Cell Signaling Technology #4858): Fig 4E S6RP (Cell Signaling Technology #2217): Fig 4E p-GSK3α/β (Cell Signaling Technology #9331): Fig 4E, 4H, Extended Data Figs. 8M, 9K GSK3α/β (Cell Signaling Technology #5676): Fig 4E, 4H, Extended Data Figs. 8M, 9K H3K4me3 (Cell Signaling Technology #9751): Figs. 2F, 2G, 2H, Extended Data Figs. 3H, 3I, 3J, 3K, 3M, 3O, 5L, 10B H3K9me3 (Cell Signaling Technology #13969): Fig 4I, Extended Data Figs. 3H, 3L, 10B H3K27Ac (Cell Signaling Technology #8173): Fig 4I, Extended Fig 3L H3K27me3 (EMD Millipore #07-449): Fig 4I, 4K, Extended Data Fig. 9D Total H3 (Cell Signaling Technology #3638): Figs. 2F, 2G, 2H, 4I, 4K, Extended Data Figs. 3H, 3I, 3J, 3K, 3M, 3O, 5L, 9D, 10B GAPDH (Cell Signaling Technology, #2118): Figs. 1E, 2A, 2C, 3E, 3J, 3N, 4C, 4E, 5C, 5G, Extended Data Figs. 1E, 1H, 1I, 3B, 3C, 3D, 3E, 3F, 3K, 3J, 5C, 5D, 5F, 5N, 7B, 7C, 7D, 7E, 8C, 8D, 9I, 11B, 11D Vinculin (Sigma Aldrich, #V9264): Figs. 1G, 1H, 2A, 2H, 2J, 3B, 3C, 4C, 4H, 4K Extended Data Figs. 1E, 1L, 2A, 3A, 5E, 7E, 8M, 9D, 9J, 9K

Immunohistochemistry:
anti-ACOD1 antibody (Abcam, #ab238580): Fig. 1F, Extended Data Fig. 1F
anti-PTEN (Abcam, #ab170941): Fig 4F, Extended Data Fig 8I, 12M
H3K27me3 (EMD Millipore #07-449): Fig. 4J, Extended Data Fig 9C
Ki-67 (Invitrogen #MA5-14520, 1:400): Extended Data Fig 12K
SLC1A5 (Sigma Aldrich #HPA035240): Extended Data Fig 7H

All antibodies utilized in the study were validated by the manufacturer.

Eukaryotic cell lines

Policy information about cell lines and Sex and Gender in Research

Cell line source(s)	Cell lines from collaborators were obtained under MTA. Mouse neural stem cells (mNSCs) with p16 Ink4a-/p14Arf background and EP1NS (human ZFTA-RELA) cell line were provided by Dr. Richard Gilbertson (University of Cambridge, UK). RCAS-TV control (NS-1, NS-2, and NS-3) and RCAS-TV ZFTA-RELA (H-57, H-41, and H-59) cell lines were provided by Dr. Eric Holland (Fred Hutchinson Cancer Research Center). ST-1 (ZFTA-NEAT1, ZFTA-MAML3) , ST-2 (ZFTA-RELA) , ST-4 (ZFTA-RELA) were provided by Dr. Kulandaimanuvel Antony Michaelraj (University of Pittsburgh School of Medicine). CPITT-1 (ZFTA-RELA) cell line was provided by Dr. Sameer Agnihotri (University of Pittsburgh School of Medicine). MAF-1329 (ZFTA-RELA) and MAF-811 (PF-A) cell lines were provided by Dr. Andrea Griesinger and Dr. Nicholas Foreman (University of Colorado Anschutz Medical Campus). CPITT-1 (ZFTA-RELA) cell line was provided by Dr. Sameer Agnihotri (University of Pittsburgh School of Medicine). MAF-1329 (ZFTA-RELA) and MAF-811 (PF-A) cell lines were provided by Dr. Andrea Griesinger and Dr. Nicholas Foreman (University of Colorado Anschutz Medical Campus). HEK293 cells were procured from ATCC (Cat #CRL-1573)
Authentication	All cell lines were authenticated by STR testing.
Mycoplasma contamination	Cell lines were routinely screened for Mycoplasma using the MycoAlert kit (Lonza) and tested negative.
Commonly misidentified lines (See ICLAC register)	None used.

Animals and other research organisms

Policy information about studies involving animals; ARRIVE guidelines recommended for reporting animal research, and Sex and Gender in Research

Laboratory animals	4- 6 weeks old, NOD-SCID-IL2R gamma chain deficient (NSG) mice (NOD.Cg-Prkdcscidll2rgtml Wjl/SzJ, #005557) were used for all experiments involving subcutaneous and orthotopic injections of the ZFTA-RELA fusion mNSCs as well as for the subcutaneous MAF-1329 patient-derived xenograft (PDX) model. For the in-utero electroporation (IUE) model we utilized pregnant 6 week old CD-1 (Charles River, Crl:CDl(ICR), #022), Acod1 WT C57BL6 animals (Jax laboratories, #003771). Similarly 6-8 week old Acod1 -/- or Nestin Cre, and Acod1 floxed mice were used for breeding before in-utero electroporation of the ZFTA-RELA plasmid into the embryos. Electroporation was performed on E15 for the embryos.
Wild animals	No wild animals were used in the study.
Reporting on sex	All in vivo experiments were performed on an equal proportion of male and female animals and all findings were reported in both sexes.
Field-collected samples	Field-collected samples were not used in this study.
Ethics oversight	All animal procedures were approved by the University of Michigan Committee on the Use and Care of Animals (PRO00010599 and PRO00011114).

Note that full information on the approval of the study protocol must also be provided in the manuscript.

Plants

Seed stocks	*Report on the source of all seed stocks or other plant material used. If applicable, state the seed stock centre and catalogue number. If plant specimens were collected from the field, describe the collection location, date and sampling procedures.*
Novel plant genotypes	*Describe the methods by which all novel plant genotypes were produced. This includes those generated by transgenic approaches, gene editing, chemical/radiation-based mutagenesis and hybridization. For transgenic lines, describe the transformation method, the number of independent lines analyzed and the generation upon which experiments were performed. For gene-edited lines, describe the editor used, the endogenous sequence targeted for editing, the targeting guide RNA sequence (if applicable) and how the editor was applied.*
Authentication	*Describe any authentication procedures for each seed stock used or novel genotype generated. Describe any experiments used to assess the effect of a mutation and, where applicable, how potential secondary effects (e.g. second site T-DNA insertions, mosiacism, off-target gene editing) were examined.*

ChIP-seq

Data deposition

☒ Confirm that both raw and final processed data have been deposited in a public database such as GEO.

☒ Confirm that you have deposited or provided access to graph files (e.g. BED files) for the called peaks.

Data access links *May remain private before publication.*	All files are deposited in GEO under the following accession numbers, GSE294954 and GSE294955

Files in database submission

SI_39603_MNSC_DMSO_50K_Repl_R2.fq.gz
SI_39604_MNSC_DMSO_50K_Rep2_R2.fq.gz
SI_39606_MNSC_Citraconate_50K_Repl_R2.fq.gz
SI_39607 _MNSC_Citraconate_50K_Rep2_R2.fq.gz
SI_33920_mNSC_EmptyVector_Repl_R2.fq.gz
SI_33921_mNSC_EmptyVector_Rep2_R2.fq.gz
SI_33922_mNSC_ZFTA_RELA_Repl_R2.fq.gz
SI_33923_mNSC_ZFTA_RELA_Rep2_R2.fq.gz
SI_33924_mNSC_ZFTA_RELA_DMSO_Repl_R2.fq.gz
SI_33925_mNSC_ZFTA_RELA_DMSO_Rep2_R2.fq.gz
SI_33926_mNSC_ZFTA_RELA_GSK_Repl_R2.fq.gz
SI_33927 _mNSC_ZFTA_RELA_GSK_Rep2_R2.fq.gz
SI_33928_mNSC_ZFTA_RELA_dmCitra_Repl_R2.fq.gz
SI_33929_mNSC_ZFTA_RELA_dmCitra_Rep2_R2.fq.gz
SI_39405_EPN1425_DMSO_H3K4me3_R2.fq.gz
SI_39406_EPN1425_DMSO_H3K4me3_R2.fq.gz
SI_39407 _EPN 1425 _lOm M_ Citraconate_H3K4me3_R2. fq.gz
SI_39408_EPN1425_10mM_Citraconate_H3K4me3_R2.fq.gz
SI_39409_EPN1425_DMSO_H3K27me3_Rl_R2.fq.gz
SI_39410_EPN1425_DMSO_H3K27me3_R2.fq.gz
SI_39411_EPN1425_10mM_Citraconate_H3K27me3_R2.fq.gz
SI_39412_EPN1425_10mM_Citraconate_H3K27me3_R2.fq.gz
SI_39263_MNSC_DMSO_Rl_H3K4me3_R2.fq.gz
SI_39264_MNSC_DMSO_R2_H3K4me3_R2.fq.gz
SI_39265_MNSC_10mM_Citraconate_Rl_H3K4me3_R2.fq.gz
SI_39266_MNSC_10mM_Citraconate_R2_H3K4me3_R2.fq.gz
SI_39267 _M NSC_DMSO _Rl_H3K27me3 _R2.fq.gz
SI_39268_MNSC_DMSO_R2_H3K27me3_R2.fq.gz
SI_39269_MNSC_10mM_Citraconate_Rl_H3K27me3_R2.fq.gz
SI_39270_MNSC_10mM_Citraconate_R2_H3K27me3_R2.fq.gz
SI_34243_EPN1425_DMSO_H3K4me3_R2.fq.gz
SI_ 34245 _EPN 1425 _ Citraconate _24h _H 3 K4me3 _R2. fq.gz

Genome browser session (e.g. UCSC)	No longer applicable

Methodology

Replicates	n=2 independent replicates were used for all ChIP-seq and ATAC-seq experiments [except Extended Data Fig. 5H (n=l each)]
Sequencing depth	Sequence depth of 40-45M
Antibodies	H3K4me3 (CST, Cat# 97515), H3K27me3 (Millipore,Cat# 07-449)
Peak calling parameters	MACS2 was used to call peaks, filtered using bedtools, and converted to bigwigs with UCSC wigtoBigwigl. Cistrome overlap analysiswas performed in R (v3.6.0) using ChipSeekAnno (v3.0.0) and ChipSeeker (vl.29.1). Enrichment heatmaps were generated using Deeptools. ATAC-seq libraries were sequenced on the Illumina HiSeq 2500 platform, utilizing a 2x50-nucleotide paired-end read length with a sequence depth of 40-45M. Sequencing of ATAC-seq libraries generated fastq files, which were initially processed using Trimmomatic (version 0.39) for trimming. These files were then aligned to the mmlO (GRCm38) mouse genome reference or hg38 (GRCh38) reference using bwa mem (version 0.7.17-r1198-dirty), and the alignments were converted to binary format with SAMtools (version 1.9). Next, we eliminated mitochondrial and duplicated reads using SAMtools and PICARD MarkDuplicates (version 2.26.0-1-gbaf4d27-SNAPSHOT). Peaks in the ATAC-seq data were identified using MACS2 (version 2.1.1.20160309). Finally, the conversion of data to bigwig format was accomplished using the UCSC tool wigtoBigwig.
Data quality	*Describe the methods used to ensure data quality in full detail, including how many peaks are at FDR 5% and above 5-fold enrichment.*
Software	MACS2 was used to call peaks, filtered using bedtools, and converted to bigwigs with UCSC wigtoBigwigl. Cistrome overlap analysiswas performed in R (v3.6.0) using ChipSeekAnno (v3.0.0) and ChipSeeker (vl.29.1). Enrichment heatmaps were generated using Deeptools. ATAC-seq libraries were sequenced on the Illumina HiSeq 2500 platform, utilizing a 2x50-nucleotide paired-end read length with a sequence depth of 40-45M. Sequencing of ATAC-seq libraries generated fastq files, which were initially processed using Trimmomatic (version 0.39) for trimming. These files were then aligned to the mmlO (GRCm38) mouse genome reference or hg38

(GRCh38) reference using bwa mem (version 0.7.17-r1198-dirty), and the alignments were converted to binary format with SAMtools (version 1.9). Next, we eliminated mitochondrial and duplicated reads using SAMtools and PICARD MarkDuplicates (version 2.26.0-1-gbaf4d27-SNAPSHOT). Peaks in the ATAC-seq data were identified using MACS2 (version 2.1.1.20160309). Finally, the conversion of data to bigwig format was accomplished using the UCSC tool wigtoBigwig.